

UC Santa Barbara

UC Santa Barbara Electronic Theses and Dissertations

Title

Role of Electrostatic Forces on Non-Equilibrium Processes at Confined Inorganic Solid-Liquid-Solid Interfaces

Permalink

<https://escholarship.org/uc/item/362840c1>

Author

Dobbs, Howard Andrew

Publication Date

2018

Peer reviewed|Thesis/dissertation

UNIVERSITY OF CALIFORNIA

Santa Barbara

**Role of Electrostatic Forces on Non-Equilibrium Processes at
Confined Inorganic Solid-Liquid-Solid Interfaces**

A dissertation submitted in partial satisfaction of the
requirements for the degree Doctor of Philosophy
in Chemical Engineering

by

Howard Andrew Dobbs

Committee in charge:

Professor Jacob N. Israelachvili, Co-Chair, in memoriam

Professor Bradley F. Chmelka, Co-Chair

Professor James Boles

Professor Mike Doherty

December 2018

The dissertation of Howard Andrew Dobbs is approved.

Professor James Boles

Professor Mike Doherty

Professor Bradley F. Chmelka, Committee Co-Chair

Professor Jacob N. Israelachvili, Committee Co-Chair

September 2018

Role of Electrostatic Forces on Non-Equilibrium Processes at

Confined Inorganic Solid-Liquid-Solid Interfaces

Copyright © 2018

by

Howard Andrew Dobbs

ACKNOWLEDGEMENTS

The success of my research and personal growth during my time in graduate school has been strongly influenced by the continued support and guidance of many unforgettable people. First and foremost, I would like to thank my PhD advisors Profs. Jacob Israelachvili and Brad Chmelka, whose guidance and mentorship have taught me how to stand on my own as a scientist while simultaneously enlightening me with a random worldly fact or story in every conversation.

Jacob, I am endlessly grateful for your support, mentorship, and constant sense of humor over the years. It has been an honor to work with and learn from such a model scientist who has maintained his passion for exploring and understanding the unknown. The motto of our lab will always stick with me as I move forward in my own career: “If it can work, it will.”

Brad, your encouragement, support, and enthusiasm over the years have been invaluable in my growth as a scientist. I greatly appreciate your constant guidance on how to effectively communicate at a scientific level, whether it is writing or presenting, which I will never forget. I also have an inexhaustible list of places to visit from all your travel stories and recommendations.

I would also like to express my gratitude to the other members of my PhD committee, Profs. James Boles and Mike Doherty, for their valuable time, unique perspectives, and guidance during my time at UCSB. Jim, thank you for always expanding my horizons, whether it is with building rally cars or firing cannons.

One of the biggest benefits of being co-advised was the understanding and collaborative environments of the Israelachvili and Chmelka groups who were always willing to be mentors and sounding boards. The guidance of past lab members and friends including Dr. Nick

Cadirov, Dr. Alex Schrader, Dr. Steve Donaldson, Dr. Dongwoog Lee, Dr. Mike Rapp, Dr. Saurabh Das, Prof. Yair Kaufman, Dr. Matt Idso, Dr. Rahul Sangodkar, and Dr. Niels Zussblatt will always be remembered and appreciated. I am especially grateful to Dr. Matt Gebbie for being an incredible friend and mentor when I first started as young graduate student. I also need to thank my current lab mates for making every day at graduate school more fun than the last including Zach Berkson, Dr. Kai Kristiansen, Sandy Chen, Tom Cristiani, Dr. Thomas Farmer, George Degen, and Nathan Prisco.

I would like to thank my parents and family for their continuous love and support over the years, making it possible for me to continue striving forward. Without them, I would not have had the opportunities to pursue a PhD and you have been an incredible inspiration for me to continue working hard. Lastly, I would like to thank my beautiful and amazing wife Katherine who has stuck by my side and supported my every step these last 9 years. Without your continued love and unwavering support, I would not have been able to accomplish all that I have.

VITA OF HOWARD ANDREW DOBBS

December 2018

EDUCATION

University of California Santa Barbara (UCSB), Santa Barbara, CA

Ph.D. in Chemical Engineering, 2013-December 2018

Advisors: Profs. Jacob N. Israelachvili & Bradley F. Chmelka

Hope College, Holland, MI

Bachelors of Science in Chemical Engineering and Chemistry, 2009-2013

Summa Cum Laude, minor in Mathematics

RESEARCH EXPERIENCE

Doctoral Research: Chemical Engineering, UCSB, 2013-2018

Advisors: Professors Jacob Israelachvili and Brad Chmelka

- Electrochemically enhanced dissolution: Characterized the influence of electrostatic forces on dissolution at confined solid-liquid-solid interfaces to develop a model for controlling dissolution rates relevant to CMP, corrosion, and development of structural materials.
- Network formation of aluminosilica materials: Investigated the development of aluminosilica networks important in structural materials and catalysis using a combination of the SFA, solution-, and solid-state NMR to relate molecular and macroscopic changes.
- Developed composite silica SFA surfaces with tunable surface roughness and composition/chemistry to improve the variety of systems studied using optical and interferometric techniques. Also developed other inorganic surface fabrication procedures, such as CaCO₃, for studying interfacial forces at different aqueous inorganic interfaces within the SFA.
- Characterized the influence on low-salinity waterflooding at carbonate/brine/oil interfaces (Collaboration with Saudi Aramco): Characterization of restructuring and physicochemical changes to improve understanding of low-salinity waterflooding processes

Undergraduate Research: Chemistry, Hope College, 2010-2013

Advisor: Professor Mary Anderson

- Synthesized and characterized PbTe nanoparticles to analyze the impact of reaction temperature on structure and crystal formation

Advisor: Professor William Polik

- Adapted dispersed fluorescence and fluorescence excitation laser spectroscopy experiments for analysis of small, unstable species such as dichlorocarbene

- Updated and modified experimental setup by developing a low delay logic converter for high-sensitivity equipment and improving laser communication programs from Python to LabView

Research Internships: Chemical Engineering, Argonne National Lab, 2012

Supervisor: Dr. Di-Jia Liu

- Utilized in-situ micro-focused XRD at the Advanced Photon Source to study the durability of lithium-oxygen batteries during sequential charging and discharging with spatial and temporal resolution
- Discovered degradation of the anodic lithium and formation of a lithium hydroxide layer on the anode that inhibits ion-transport and battery functionality

FELLOWSHIPS, HONORS, & AWARDS

ACS Colloid and Surface Chemistry Division Outstanding Student Poster Award, 2018

Amgen-Clorox Annual Graduate Student Symposium Poster Prize (UCSB), 2015

CAI-STEM Langmuir Poster Prize, 2014

Blok-Klophenstein Award for Graduate Study (Hope College), 2013

Goldwater Scholarship Honorable Mention (Hope College), 2012

National AIChE Undergraduate Poster Competition, 2nd place, 2010-2012

Jaeger Scholarship (Hope College), 2011-2013

Freshmen Engineering Prize (Hope College), 2009

Dean's Award (Hope College), 2009-2013

Trustee Scholarship (Hope College), 2009-2013

PUBLICATIONS

1. Role of electrochemical surface potential and irradiation on garnet-type almandine's dissolution kinetics. Hsiao, Y.-H.; Plante, E.; Krishnan, N.; **Dobbs, H.**; Pape, Y.; Neithalath, N.; Bauchy, M.; Israelachvili, J.; Sant, G. (2018) *Journal of Physical Chemistry Part C*, doi: 10.1021/acs.jpcc.8b04459
2. Surface chemical heterogeneity modulates silica surface hydration. Schrader, A.; Monroe, J.; Sheil, R.; **Dobbs, H.**; Keller, T.; Li, Y.; Jain, S.; Shell, M.; Israelachvili, J.; Han, S. (2018) *Proc. Natl. Acad. Sci.*, 115 (12): 2890-2895. doi: 10.1073/pnas.1722263115
3. New Atomic to Molecular Scale Insights into SmartWater Flooding Mechanisms in Carbonates. Chen, S.-Y.; Kaufman, Y.; Kristiansen, K.; **Dobbs, H.**; Cadirov, N.; Seo, D.; Schrader, A.; Andresen, R.; Mohammed, B.; Subhash, C.; Boles, J.; Ali, A.; Jacob, N. I. (2018) *Society of Petroleum Engineers*. doi:10.2118/190281-MS
4. Ultra-smooth, chemically functional silica surfaces for surface interaction measurements and optical/interferometry-based techniques. **Dobbs, H.**; Kaufman, Y.; Scott, J.; Kristiansen, K.; Schrader, A.; Chen, S.-Y.; Duda, P.; Israelachvili, J. (2017) *Advanced Engineering Materials*, 1700630. doi: 10.1002/adem.20170063
5. In situ nano- to microscopic imaging and growth mechanism of electrochemical dissolution (e.g., corrosion) of a confined metal surface. Merola, C.; Cheng, H.-W.; Schwenzfeier, K.; Kristiansen,

- K.; Chen, Y.-J.; **Dobbs, H.**; Israelachvili, J.; Valtiner, M. (2017) *Proc. Natl. Acad. Sci.*, 114 (36): 9541-9546. doi: 10.1073/pnas.1708205114
6. Effects of salinity on oil recovery (the “dilution effect”): experimental and theoretical studies of crude oil/brine/carbonate surface restructuring and associated physicochemical interactions. Chen, S.-Y.; Kaufman, Y.; Kristiansen, K.; Seo, D.; Schrader, A.; Alotaibi, M.; **Dobbs, H.**; Cadirov, N.; Boles, J.; Ayirala, S.; Israelachvili, J.; Yousef, A. (2017) *Energy Fuels*. doi: 10.1021/acs.energyfuels.7b00869
 7. Long range electrostatic forces in ionic liquids. Gebbie, M.; Smith, A.; **Dobbs, H.**; Lee, A.; Warr, G.; Banquy, X.; Valtiner, M.; Rutland, M.; Israelachvili, J.; Perkin, S.; Atkin, R. (2017) *Chem. Commun.*, 53: 1214-1224. doi: 10.1039/C6CC08820A
 8. Tuning underwater adhesion with cation- π interactions. Gebbie, M.; Wei, W.; Schrader, A.; Cristiani, T.; **Dobbs, H.**; Idso, M.; Chmelka, B.; Waite, J.; Israelachvili, J. (2017) *Nature Chemistry*, 9: 473-479. doi: 10.1038/nchem.2720
 9. Defining the catechol-cation synergy for enhanced wet adhesion to mineral surfaces. Rapp, M.; Maier, G.; **Dobbs, H.**; Higdon, N.; Waite, H.; Butler, A.; Israelachvili, J. (2016) *J. Am. Chem. Soc.*, 138 (29): 9013-9016. doi: 10.1021/jacs.6b03453
 10. Long-range electrostatic screening in ionic liquids. Gebbie, M.; **Dobbs, H.**; Valtiner, M.; Israelachvili, J. (2015) *Proc. Natl. Acad. Sci.*, 112 (24): 7432-7437. doi: 10.1073/pnas.1508366112
 11. Reversibility of anodic lithium in rechargeable lithium-oxygen batteries. Shui, J.; Okasinski, J.; Kenesei, P.; **Dobbs, H.**; Zhao, D.; Almer, J.; Liu, D. (2013) *Nature Communications*, 4:2255. doi:10.1038/ncomms3255

MANUSCRIPTS IN PREPARATION

1. “Electrochemically enhanced dissolution of alumina and silica in weakly alkaline environments.” **Dobbs, H.A.**; Kristiansen, K.; Schrader, A.; Berkson, Z.; Degen, G.; Oey, T.; Sant, G.; Chmelka, B.; Israelachvili, J. (2018) to be submitted to *Proc. Natl. Acad. Sci.*
2. “Relationship Between Aqueous Chemistry and Composition, Structure, and Solubility of N-A-S-H.” Williamson, T.; Han, J.; Katz, L.; **Dobbs, H.**; Chmelka, B.; Sant, G.; Juneger, M.C.G. (2018) to be submitted to *Journal of the American Ceramic Society*
3. “Network formation and strength development in alkali-activated aluminosilica cements.” **Dobbs, H.A.* (co-1st author)**; Berkson, Z.J.*; Kristiansen, K.; Schrader, A.; Degen, G.; Israelachvili, J.N.; Chmelka, B.F. (2018)
4. “Time-dependent physicochemical changes of carbonate surfaces from SmartWater-flooding processes for improved oil recovery.” Chen, S.Y.; Kristiansen, K.; Seo, D.; Cadirov, N.; **Dobbs, H.**; Kaufman, Y.; Schrader, A.; Andresen-Equiluz, R.; Alotaibi, M.; Ayirala, S.; Boles, J.; Yousef, A.; Israelachvili, J. (2018) under review for *Langmuir*

PRESENTATIONS

1. Oral Presentation at 2018 ACS Spring National Meeting, New Orleans, LA
“Long-range electrostatic forces in ionic liquids.”
2. Poster Presentation at 2018 ACS Spring National Meeting, New Orleans, LA
“Electrochemically enhanced dissolution of silica and alumina in alkaline environments.”
3. Oral Presentation at 2017 Amgen-Clorox Graduate Student Symposium, Santa Barbara, CA
“Characterizing the electrochemically enhanced dissolution of silica and alumina in alkaline environments.”
4. Poster Presentation at 2016 Amgen-Clorox Graduate Student Symposium, Santa Barbara, CA
“Characterizing the electrochemically enhanced dissolution of inorganic materials in electrolyte environments.”
5. Oral Presentation at 2016 AIChE National Meeting, San Francisco, CA
“Characterizing the electrochemically enhanced dissolution of silica and alumina in alkaline environments.”
6. Poster Presentation at 2016 Materials Research Outreach program, Santa Barbara, CA
“Characterizing the electrochemically enhanced dissolution and condensation of aluminosilicates in alkaline environments.”
7. Oral Presentation at 2015 International Conference on Grand Challenges in Construction Materials, Los Angeles, CA
“Characterizing the enhanced dissolution and condensation of aluminosilicates in alkaline environments.”
8. Poster Presentation at 2015 Amgen-Clorox Graduate Student Symposium, Santa Barbara, CA
“Characterizing the enhanced dissolution and condensation of aluminosilicates in alkaline environments.”
9. Poster Presentation at 2014 International Workshop in Colloidal and Interfacial Science, Technology, Engineering and Mathematics, Cancun, Mexico
“‘Differential double-layer dissolution’ of aluminosilicate materials.”
10. Poster Presentation at 2014 International Workshop in Colloidal and Interfacial Science, Technology, Engineering and Mathematics, Cancun, Mexico
“Creation of reusable, synthetic surfaces with tunable roughness for the SFA.”

ABSTRACT

Role of Electrostatic Forces on Non-Equilibrium Processes at
Confined Inorganic Solid-Liquid-Solid Interfaces

by

Howard Andrew Dobbs

Non-equilibrium processes at confined solid-liquid-solid interfaces are prevalent in a wide range of naturally occurring and technologically relevant phenomena such as corrosion, molecular network formation, dissolution and restructuring. Nevertheless, the complex intermolecular interactions involved in the development of macroscopic properties inhibits a fundamental understanding of the evolution of the interface. This is largely due to the difficulties associated with characterizing the role of surface and intermolecular interactions on macroscopic changes within the solid-liquid-solid interface as it evolves over time. In this dissertation, a combination of the surface forces apparatus (SFA), nuclear magnetic resonance (NMR) spectroscopy, and standard materials characterization techniques are used to characterize the intermolecular forces present in confined solid-liquid-solid interfaces and the resultant molecular and macroscopic changes. A new method for producing ultra-smooth (< 3 nm) composite surfaces for the SFA and other optical/interferometric techniques is presented which overcomes the limitations of traditional mica interferometry surfaces while broadening the functionality to achieve characterization of surface and interfacial phenomena in previously

unattainable systems. Using this unique combination of characterization methods and tools, the molecular-level measurements establish the influence of electrostatic forces on dissolution-based processes at confined, asymmetric solid-liquid solid interfaces. The results demonstrate that dissolution at confined solid-liquid-solid interfaces can be dramatically enhanced through the manipulation of local electrostatic forces (i.e., electrochemically enhanced dissolution) which offers a new avenue for manipulating dissolution processes in many technological applications such as chemical mechanical polishing and electrochemical corrosion. Additionally, molecular network formation processes initialize through the dissolution and subsequent reaction of surface species which are heavily influenced by surface interactions which direct local ion behavior. Measurement of the molecular structure and surface interactions indicate that only a small portion (<5%) of the material is involved in the network formation process. These results demonstrate the significant impact that initial dissolution processes have on the macroscopic properties of the network, highlighting the importance of the role of molecular-level interactions in the development of macroscopic properties. The methods, analyses, and resulting insights in characterizing the influence of molecular interactions on macroscopic changes are expected to be broadly relevant for non-equilibrium processes at confined solid-liquid-solid interfaces and help establish critical parameters to directly influence the evolution of macroscopic properties at the interface.

TABLE OF CONTENTS

ACKNOWLEDGEMENTS	iv
VITA OF HOWARD ANDREW DOBBS	vi
ABSTRACT	x
Chapter 1: Introduction and Background	1
1.1 Motivation and Objectives	1
1.2 Electrostatic forces between surfaces in aqueous environments	4
1.3 Experimental approaches	8
1.3.1 The Surface Forces Apparatus	8
References	10
Chapter 2: Ultra-smooth, chemically functional silica surfaces for surface interaction measurements and optical/interferometry-based techniques	13
2.1 Abstract	13
2.2 Introduction	14
2.3 Experimental Methods	19
2.3.1 Fabrication of silica surfaces	19
2.3.2 Octadecyltrichlorosilane (OTS) silica surface modification	21
2.3.3 Characterization of thin film physical properties	21
2.3.4 Surface force measurements using the SFA	22
2.4 Results and Discussion	22
2.4.1 Characterization of the fabricated ultra-smooth SiO ₂ disks	22
2.4.2 Double layer interactions using the fabricated disks	28

2.4.3 Surface chemistry modification through silane chemistry.....	29
2.5 Conclusions.....	34
References.....	36
Chapter 3: Electrochemically enhanced dissolution at confined, asymmetric interfaces	40
3.1 Electrochemically enhanced dissolution of silica and alumina in alkaline environments.....	40
3.1.1 Abstract.....	40
3.1.2 Introduction.....	41
3.1.3 Experimental methods.....	45
3.1.4 Results and Discussion.....	48
3.1.5 Discussion and Conclusions.....	62
3.2 Electrochemically controlled dissolution of inorganic materials.....	64
3.2.1 Electrochemically enhanced dissolution of diamond.....	64
References.....	66
Chapter 4: In Situ nano-to-microscopic imaging and growth mechanism of electrochemical dissolution (eg, corrosion) of a confined metal surface.....	74
4.1 Abstract.....	74
4.2 Introduction.....	75
4.3 Experimental methods.....	78
4.3.1 Chemicals.....	78
4.3.2 Surface Forces Apparatus (SFA).....	78
4.3.3 Apparatus modifications.....	79
4.3.3 Experimental procedure.....	81

4.3.4 Nickel thickness determination.....	82
4.4 Results and Discussion	83
4.5 Conclusions.....	94
References.....	96
Chapter 5: Molecular network formation in alkali-activated aluminosilica cements	100
5.1 Abstract.....	100
5.2 Introduction.....	101
5.3 Experimental methods	104
5.3.1 Synthesis of IPB-like aluminosilica network.....	104
5.3.2 Scanning electron microscopy and X-ray diffraction	104
5.3.3 Surface forces apparatus (SFA)	105
5.3.4 1D and 2D solid-state DNP NMR	105
5.4 Results and discussion	106
5.4.1 Long-range order and morphology of aluminosilica materials crosslinked for short reaction times	106
5.4.2 Changes in the local ^1H , ^{23}Na , ^{27}Al , and ^{29}Si environments formed at early reaction times (24-72 h).....	108
5.4.3 Characterizing early dissolution behavior of aluminosilica network formation.....	123
5.5 Summary and conclusions	126
References.....	127
Chapter 6: Conclusions	132

Chapter 1: Introduction and Background

1.1 Motivation and Objectives

Non-equilibrium processes are prevalent at confined solid-liquid-solid interfaces where intermolecular and surface forces play an important role. In many naturally occurring and technologically important processes, for example, catalysis, corrosion, network formation of cements, and bioadhesion, the dynamic changes within the system occur primarily at the surface. Characterizing and understanding the interfacial phenomena involved in these non-equilibrium processes relies on the full consideration of the dynamic changes occurring at the interface and how it influences the overall system behavior. Van der Waals forces, electrostatic forces, hydrogen bonding, and hydrophobic forces may be present which will influence how the interface may evolve with time. Characterizing how the intermolecular and surface forces influence the changes occurring at the interface is paramount to obtaining a fundamental understanding of various non-equilibrium processes and how to control them for technological applications.

This dissertation focuses on non-equilibrium processes that occur at inorganic solid-liquid-solid interfaces where intermolecular interactions, specifically electrostatic forces, dramatically influence the evolution of the system. Each of the systems discussed herein involve confined solid-liquid-solid interfaces where dissolution and subsequent network formation or restructuring occurs. These processes which involve dissolution are especially important in many natural and technological systems, from structural materials^{1,2} to microelectronics^{3,4} and catalysts.⁵ Although the materials in each system may differ in chemical composition, morphology, and local structure, they each exhibit similar dissolution

reactions that release charged species from the surface into solution which are available for further reactions and effect the local ionic concentration. Specifically, this dissertation examines non-equilibrium processes where surface interactions strongly influence the development of the system for two different processes: (i) electrochemically enhanced dissolution processes observed in silica, alumina, diamond, and nickel (Chapters 3 and 4) and (ii) molecular network formation in alkali-activated aluminosilica cements (Chapter 5). In each of these processes, the influence of environmental conditions on the macroscopic properties of the material are empirically understood, but the changes at a molecular level are poorly understood. A combination of the Surface Forces Apparatus (SFA), Nuclear Magnetic Resonance (NMR) spectroscopy, and standard characterization techniques is used to characterize the molecular forces and structures and correlate them with changes in the macroscopic structure and properties. The objective of this work is to characterize the role of surface interactions on these non-equilibrium processes to develop better methods to influence, and potentially control, the evolution of the interface and specific macroscopic properties.

Each of the non-equilibrium processes mentioned in this dissertation are phenomena that have been known and studied for decades, however a fundamental understanding of the molecular interactions and forces in these phenomena remain poorly understood. In part, this has been due to the challenges associated with the molecular characterization of changes which occur at the solid-liquid-solid interface while the processes are occurring. Advancements in characterization techniques are required to develop the proper tools to study the complex interactions and changes that occur at the solid-liquid-solid interface. Chapter 2 discusses the development of chemically functional silica surfaces for the SFA using various

photolithography and vacuum deposition techniques. These composite surfaces have an ultra-smooth (<0.4 nm RMS roughness) silica layer which can be functionalized using deposition, chemisorption, or adsorption from solution to create novel inorganic and organic surfaces which were previously unobtainable with standard SFA techniques. These composite surfaces provide the basis for studying more complex and complete interfaces using optical and interferometry techniques which enables further molecular characterization of non-equilibrium processes at confined solid-liquid-solid interfaces.

Dissolution processes have been extensively characterized for many inorganic materials; however, there are several naturally occurring and technologically important phenomena that exhibit enhanced dissolution, such as pressure solution and chemical mechanical polishing, which remain poorly understood. Chapters 3 and 4 discuss the enhanced dissolution phenomena observed at confined solid-liquid-solid interfaces involving silica, alumina, diamond, and nickel using a combination of SFA and standard materials characterization techniques. Chapter 3 focuses on the influence of electrostatic forces on the observed enhanced dissolution at confined, asymmetric solid-liquid-solid interfaces for silica, alumina, and diamond in aqueous solutions and provides a semi-quantitative model for understanding electrochemically enhanced dissolution phenomena. Chapter 4 discusses the electrochemical dissolution (e.g., crevice corrosion) of confined, asymmetric solid-liquid-solid interfaces for nickel in aqueous solutions and characterizes the changes in surface structure with regards to the electrochemical dissolution behavior.

Dissolution at confined interfaces is also an important step in network formation processes for inorganic oxide materials. Network formation is initiated by the dissolution and subsequent reaction (e.g., condensation) of surface species to form inorganic oxide networks

with useful macroscopic properties. The structure, which dictates the macroscopic properties, of the resulting inorganic oxide material is controlled by the relative concentration of surface species in solution near the surface based on the dissolution of each surface. Chapter 5 discusses the observed dissolution and formation of aluminosilica networks in highly alkaline solutions using a combination of SFA and NMR spectroscopy methods. Changes in molecular structure with increased reaction times are correlated with macroscopic properties to understand the early stage dissolution and formation of aluminosilica networks. The remainder of this Introduction discusses the basic concepts and techniques used to understand and characterize the different phenomena. The scientific questions motivating the research for each phenomenon are further expanded upon in their respective chapters.

1.2 Electrostatic forces between surfaces in aqueous environments

At a fundamental level, surfaces exhibit overall attractive or repulsive behavior based on the individual contributions from non-specific and specific interactions between atoms and molecules in the system. Electromagnetic forces, which arise from the electronic properties of atoms and molecules, are effective over large distances and are the basis of the commonly known intermolecular interactions such as van der Waals forces, electrostatic forces, hydrogen bonding, and hydrophobic forces.⁶ Van der Waals forces are dependent on the dipoles, polarizability, and dispersion forces between atoms and acts between all atoms and molecules. Electrostatic interactions occur between charged species through Coulombic interactions and results in the formation of an electrostatic double layer which screens the surface charge so that it is neutral when far from the surface. The van der Waals and electrostatic forces in a liquid medium can be collectively described by the DLVO theory (Derjaguin, Landau, Verwey, and Overbeek) which provides an analytical expression of the distance dependence

of the colloidal forces between two surfaces.^{7,8} Hydrogen bonding forces exist in systems to varying degrees between electronegative atoms and hydrogen atoms covalently bound to similar electronegative atoms. It is accepted that the hydrogen bond is predominately an electrostatic interaction,^{9,10} but this force is still not fully understood at a fundamental level. Hydrophobic forces, which describe the strong attraction between hydrophobic molecules and surfaces in water due to the inability to form hydrogen bonds, are also not fully understood at a fundamental level but recent progress has been made in deriving an interaction potential.¹¹

Electrostatic forces are the primary focus of this dissertation due to the strong influence they have on ionic species over a relatively long range compared to other surface forces. A more detailed description of the electrostatic double layer is required to understand the impact it has on non-equilibrium processes such as dissolution. As mentioned above, electrostatic interactions between charged species results in the formation of an electrostatic double layer to balance the surface charge and achieve a net neutral system. The electrostatic double layer is comprised of a Stern or Helmholtz layer, comprised of transiently bound counterions on the surface, and a diffuse electric double layer, an atmosphere of ions in rapid thermal motion loosely correlated with the surface depicted in Figure 1.1.

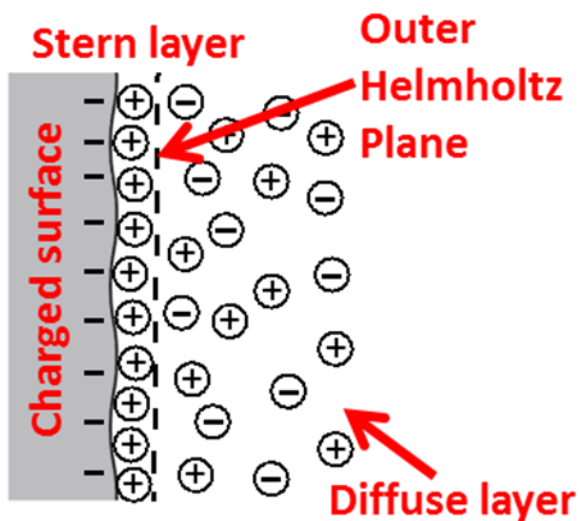


Figure 1.1 Structure of the electrostatic double layer comprised of the Stern or Helmholtz layer and the diffuse electric double layer. Ions bound to a surface are not rigidly bound but can exchange with other ions in solution. The lifetime on the surface is dependent on the strength of the interaction with the charged surface.

For two charged surfaces in an aqueous solution, the Poisson-Boltzmann equation describes the ionic distribution near planar charged surfaces in water and is given by:

$$\frac{d^2\psi}{dx^2} = - \left(\frac{ze\rho_0}{\epsilon_0\epsilon} \right) e^{-\frac{ze\psi}{kT}} \quad (1.1)$$

where ψ is the electrostatic potential, x is the coordinate position between the surfaces with $x = 0$ as the midplane, ϵ_0 is the permittivity of free space, ϵ is the bulk dielectric permittivity of the aqueous solution, k is the Boltzmann constant, T is the temperature, ρ_0 is the number density of ions with valency z at the midpoint between the surfaces, and e is the elementary charge of an electron.¹² The solution to this equation gives the potential ψ , electric field $E = -\frac{d\psi}{dx}$, and counterion density ρ at any point x in the gap between the surfaces. Jönsson et al. showed that most of the counterions that effectively balance the surface charge are located within the first few ångstroms from the surface (i.e., the Stern layer). However, for lower surface charge densities, the layer of counterions extends well beyond the surface and becomes more diffuse (i.e., the diffuse double layer).¹³

The thickness of the Stern and Helmholtz layers is on the order of a few ångstroms and reflects the finite size of the charged surface groups (coions) and the transiently bound counterions. Within this region, the Poisson-Boltzmann equation cannot hold and the potential drop across the Stern and Helmholtz layer is linear.¹⁴⁻¹⁶ Outside of the Stern and Helmholtz layer, the potential follows the Poisson-Boltzmann equation.

The Poisson-Boltzmann equation was derived for two charged surfaces in water, however most charged surfaces interact across a solution which already contains electrolyte ions. For charged surfaces which have a bulk reservoir of electrolyte ions, the Poisson-Boltzmann equation can be simplified to the Grahame equation,¹² which is further simplified for potentials less than 25 mV:

$$\sigma = \varepsilon_0 \varepsilon \kappa \psi_0 \quad (1.2)$$

where, for a monovalent electrolyte at 25°C,

$$\kappa^{-1} = \left(\frac{\varepsilon_0 \varepsilon k T}{2 \rho_{\infty} e^2} \right)^{1/2} \quad (1.2)$$

Under these assumptions, the potential is now proportional to the surface charge density. The characteristic length of the diffuse layer, $1/\kappa$, is known as the Debye length and it depends solely on the solution properties of the system. The Debye length is an effective length scale to describe the range that the electrostatic forces extend from the surface. There are now several key parameters to the electrostatic double layer: (i) the surface potential ψ_0 , which is dependent on the material interface, and (ii) the Debye length $1/\kappa$, which is only dependent on the solution conditions.

The electrostatic forces directly influence the local ion concentration near a surface which can play an important role in non-equilibrium processes such as dissolution, restructuring, and network formation. The electrostatic double layer interaction and its influence on non-equilibrium processes is further discussed for enhanced dissolution at asymmetric solid-liquid-solid interfaces in Chapter 3 and in the reduction in adhesion energy through the application of the extended DLVO theory in Chapter 6.

1.3 Experimental approaches

The comparison of molecular level changes at the interface with development of macroscopic material properties relies on a broad range of characterization techniques which can span the different length scales. In this work, a combination of the Surface Forces Apparatus (SFA) with materials characterization techniques such as Nuclear Magnetic Resonance (NMR) spectroscopy, ellipsometry, X-ray diffraction, scanning electron microscopy with energy dispersive spectroscopy, and X-ray photoelectron spectroscopy, were used to characterize the molecular to macroscopic changes of the non-equilibrium processes.

The SFA is the primary characterization technique used in this work to measure surface interaction forces as well as the dissolution of surface materials with a resolution of 3 Å. This combination allowed us to characterize the molecular interactions and correlate them with macroscopic dissolution. 1D and 2D NMR spectroscopy were also important in characterizing the changes in local molecular structure during the network formation of aluminosilica materials. A brief description of the SFA technique is provided below while descriptions of the other characterization techniques are provided in the relevant chapters.

1.3.1 The Surface Forces Apparatus

The surface forces apparatus (SFA) is used to measure and analyze the intermolecular interactions between two cylindrically-curved surfaces. The SFA has been used to characterize the dynamic behavior in a wide range of systems, including electrochemical and biological systems.¹⁷ The SFA measures the interaction forces (attractive or repulsive) between two surfaces as they are controllably brought together and retracted. The bottom surface is attached to a double cantilever spring which deflects when force is applied which can be measured using Hooke's Law, $F = k\Delta x$, where F is the force, k is the spring

constant, and Δx is the deflection of the spring.¹⁸ The double cantilever spring ensures that the surfaces move in a vertical motion without significant horizontal sliding. The position of the surfaces is controlled to within 1 Å using a high-voltage piezoelectric tube.

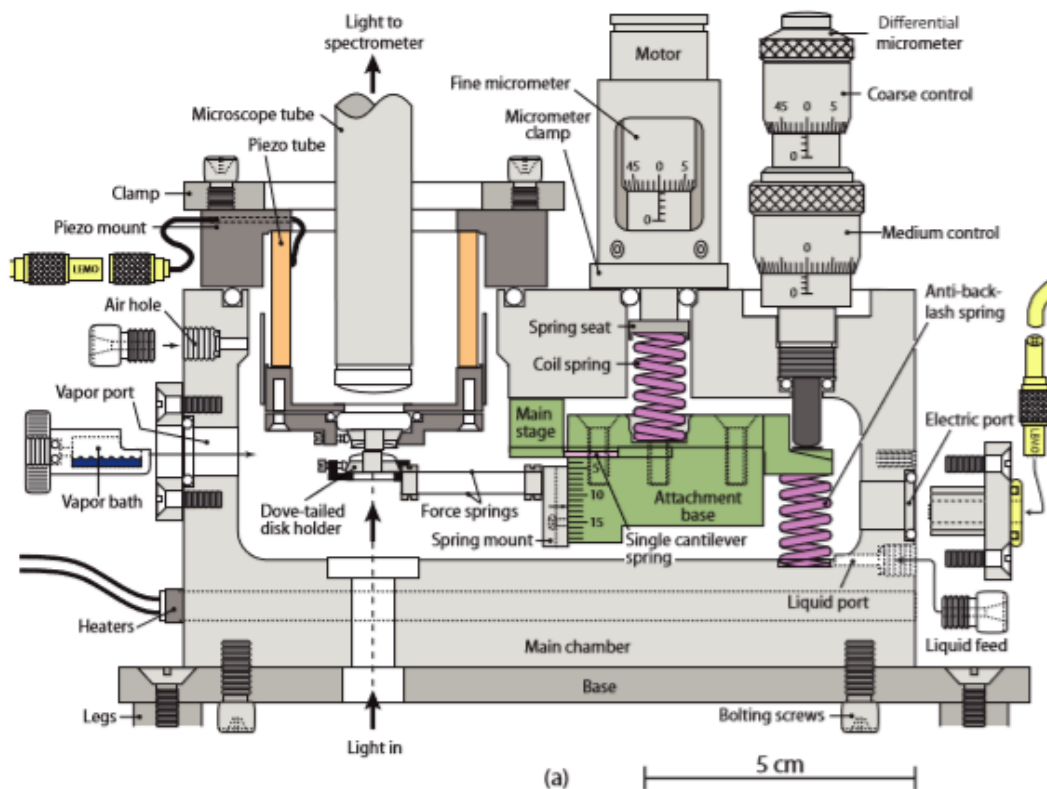


Figure 1.2 A section through the center of the SFA apparatus (adapted from reference 17). The SFA has a wide range of control over the variables involved in force measurements including positional control and force spring stiffness. The different ports allow for control of temperature, humidity, or vapor and liquid environment. Additionally, different disk mounts can be used to achieve additional functionality for friction shear measurements or electrochemical measurements.

The SFA uses multiple-beam interferometry to measure the absolute distance between two surfaces which each have a reflective (1% transmissive, >90% reflective) layer. White light passes through the two surfaces where it reflects between the two reflective layers, resulting in constructive and destructive interference. The interference pattern can be visualized in wavelength space by transmitting the light into a spectrometer which results in observable fringes of equal chromatic order (FECO). The wavelength position of the fringes

will change based on the distance between the two surfaces, specifically between the two reflective layers, which allows for distance measurements with Ångstrom-level resolution as shown in Figure 1.3.¹⁹ The FECO are also sensitive to any deformations in the reflective layer which enables the visualization of the surface profile. This allows the SFA technique to measure force with a resolution of 10^{-8} N to characterize intermolecular interactions and provide information on macroscopic changes to the surface thickness or profile throughout the experiment.

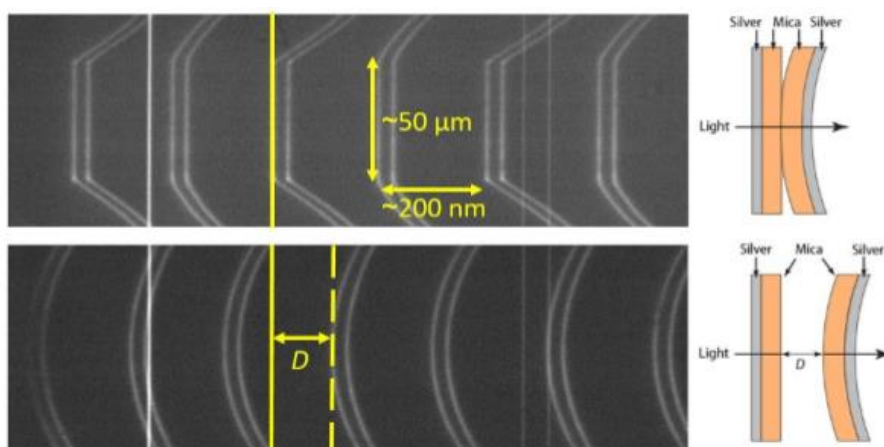


Figure 1.3 Multiple-beam interferometry between two back-silvered muscovite mica surfaces in air. White light passes through the surfaces resulting in constructive and destructive interference which can be viewed as fringes of equal chromatic order (FECO) using a spectrometer. The distance between the reflective layers can be determined based on the FECO spacing and the shape of the FECO gives information on the surface profile.

References

1. Bjornstrom J, Martinelli A, Matic A, Borjesson L, Panas I (2004) Accelerating effects of colloidal nano-silica for beneficial calcium-silica-hydrate formation in cement. *Chem. Phys. Lett.* 392:242-248
2. Brand AS, Bullard JW (2017) Dissolution Kinetics of Cubic Tricalcium Aluminate Measured by Digital Holographic Microscopy. *Langmuir* 33:9645-9656

3. Krishnan M, Nalaskowski JW, Cook LM (2010) Chemical Mechanical Planarization: Slurry Chemistry, Materials, and Mechanisms. *Chem. Rev.* 110:178-204
4. Yan W, Zhang Z, Guo X, Liu W, Song Z (2015) The Effect of pH on Sapphire Chemical Mechanical Polishing. *ECS J. Solid State Sci. Technol.* 4(3):108-111
5. Zhai D, Zhao L, Liu Y, Xu J, Shen B, Gao, J (2015) Dissolution and Absorption: A Molecular Mechanism of Mesopore Formation in Alkaline Treatment of Zeolite. *Chem. Mater.* 27(1):67-74
6. Feynman, R. P. Forces in Molecules. *Phys. Rev.* 1939, 56 (4), 340–343
7. Derjaguin, B. V.; Churaev, N. V.; Muller, V. M. The Derjaguin—Landau—Verwey—Overbeek (DLVO) Theory of Stability of Lyophobic Colloids. In *Surface Forces*; Springer US: Boston, MA, 1987; pp 293–310.
8. Verwey, E. J. W. *Theory of the Stability of Lyophobic Colloids; the Interaction of Sol Particles Having an Electric Double Layer*; Elsevier Pub. Co.: New York, 1948.
9. Coulson, C.A. (1961) *Valence* (2nd ed.). New York: Oxford University Press
10. Umeyama, H.; Morokuma K. (1977) The origin of hydrogen bonding. An energy decomposition study. *J. Am. Chem. Soc.* 99(5):1316-1332
11. Donaldson, S. H.; Røyne, A.; Kristiansen, K.; Rapp, M. V.; Das, S.; Gebbie, M. A.; Lee, D. W.; Stock, P.; Valtiner, M.; Israelachvili, J. Developing a General Interaction Potential for Hydrophobic and Hydrophilic Interactions. *Langmuir* 2015, 31 (7), 2051–2064.
12. Israelachvili JN (2011) *Intermolecular and Surface Forces*, 3rd ed. (Elsevier, California, USA)

13. Jönsson, B.; Wennerström, H. (1981) Thermodynamics of ionic amphiphile-water systems. *Journal of Colloid and Interface Science* 80(2):482-496
14. Stern, O. (1924) The theory of the electrolytic double-layer. *Z. Elektrochemie und Angewandte Physikalische Chemi* 30:508
15. Verwey, E.J.W.; Overbeek, J.T.G. (1948) Theory of the stability of lyophobic colloids. Amsterdam:Elsevier
16. Hiemenz, P.; Rajagopalan, R. (1997) Principles of colloid and surface chemistry. New York: Marcel Dekker, Inc.
17. Israelachvili J, Min Y, Alig A, Carver G, Greene W, Kristiansen K, Meyer E, Pesika N, Rosenberg K, Zeng H (2010) Recent advances in the surface forces apparatus (SFA) technique. *Rep. Prog. Phys.* 73:036601
18. Tabor, D.; Winterton, R. H. S. The Direct Measurement of Normal and Retarded van der Waals Forces. *Proc. R. Soc. A Math. Phys. Eng. Sci.* 1969, 312 (1511), 435–450
19. Israelachvili, J. Thin Film Studies Using Multiple-Beam Interferometry. *J. Colloid Interface Sci.* 1973, 44 (2), 259–272

Chapter 2: Ultra-smooth, chemically functional silica surfaces for surface interaction measurements and optical/interferometry-based techniques

Reproduced with permission from Howard Dobbs, Yair Kaufman, Jeff Scott, Kai Kristiansen, Alex Schrader, Szu-Ying Chen, Peter Duda III, Jacob Israelachvili, *Advanced Engineering Materials* 2018, 20, 1700630.

2.1 Abstract

In this chapter, the development of chemically functional silica surfaces for use in surface characterization interferometry techniques is demonstrated to enable a wider range of available surface chemistries that were previously unobtainable in studying interfacial phenomena. The study of interfacial phenomena is central to a range of chemical, physical, optical, and electromagnetic systems such as surface imaging, polymer interactions, friction/wear, and ion-transport in batteries. Studying intermolecular forces and processes of interfaces at the sub-nano scale has proven difficult due to limitations in surface preparation methods. Here we describe a method for fabricating reflective, deformable composite layers that expose an ultra-smooth silica (SiO₂) surface (RMS roughness <0.4 nm) with interferometric applications. The robust design allows for cleaning and reusing the same surfaces for over a week of continuous experimentation without degradation. The electric double-layer forces measured using the composite surfaces are within 10% of the theoretically predicted values. We also demonstrate that standard chemisorption and physisorption procedures on silica can be applied to chemically modify the surfaces; as a demonstration of this, the composite surfaces were successfully modified with octadecyltrichlorosilane (OTS)

to study their hydrophobic interactions in water using a surface force apparatus (SFA). These composite surfaces provide a basis for the preparation of a variety of new surfaces and should be particularly beneficial for the SFA and colloidal probe methods that employ optical/interferometric and electrochemical techniques, enabling characterization of previously unattainable surface and interfacial phenomena.

2.2 Introduction

Surface and interfacial science has been a major focus across a range of diverse and interdisciplinary fields. The ability to measure the molecular interaction forces and energies is crucial for shedding light on interfacial phenomena where van der Waals, electrostatic, adhesion, polymer, or hydration forces can all be important depending on the system. Studying these physical forces is critical to developing an understanding of the fundamental and technologically relevant processes that occur at different interfaces – processes such as electrochemical reactions,^{1,2} catalysis,^{3,4} adhesion/repulsion,⁵⁻⁷ frictional wear,⁸⁻¹⁰ and self-assembly of mono- and multilayers.^{11,12,47}

The characterization of surface and interfacial phenomena has progressed significantly due to the development of experimental techniques capable of interrogating the physical and chemical nature of surfaces. Such instruments include Atomic Force Microscopes (AFM), the Johnson, Kendall and Roberts (JKR) apparatus, nano- and micro- indenters, tribometers, Raman and infrared spectrometers, interferometers, and the Surface Force Apparatus (SFA). The most diverse characterization methods developed for studying interfaces are interferometry-based techniques, such as Fabry-Pérot interferometers¹³ or reflection interference contrast microscopy (RICM),¹⁴ which optically visualize the surface topography by observing interference patterns that occur when shining monochromatic or white light

between two surfaces. Interference between the two reflecting layers gives rise to Newton's rings where constructive and destructive interference appear as a series of alternating bright and dark rings centered around the point of contact, as demonstrated in the RICM column of **Figure 2.1b** for *monochromatic* light. The distance between the two surfaces can be measured by studying the variation in light intensity across the large contact area, allowing characterization of the surface height profile, especially roughness, with nanometer resolution in the height, z , direction.¹⁵

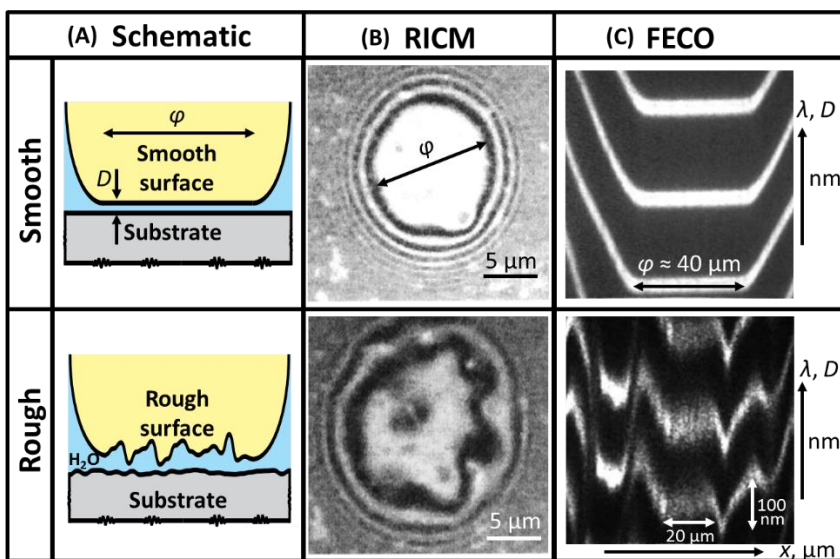


Figure 2.1 Examples of interferometry-based surface analysis techniques to measure smooth and rough surfaces, shown schematically in the left column for sphere on flat geometry, under both static and dynamic conditions. Newton ring interference patterns using monochromatic ($\lambda_{\text{Hg}} = 546.1 \text{ nm}$) light and reflection interference contrast microscopy (RICM) for smooth and rough vesicles on a flat SiO_2 surface adapted from Albersdörfer et al. 1997.¹⁵ FECO fringe interference patterns using white light for smooth and rough SiO_2 surfaces dissolving in an acidic environment adapted from Greene et al. 2009.¹⁶

Prominent interferometry-based techniques are the Surface Forces Apparatus (SFA)¹⁷ and its derivatives¹⁸⁻²² which use *white* light interferometry to measure the absolute surface separation (distances) between two surfaces. The SFA allows sub-nanometer resolution measurements by separating the Newton's rings into different wavelengths of light to observe

‘Fringes of Equal Chromatic Order’ (FECO), which are shown in the SFA column of **Figure 2.1c**.¹⁶ By measuring the wavelength of each fringe, the absolute distance (sub-nm resolution) between the surfaces, and the surface profiles (μm resolution) can be directly measured. In addition, the wavelength of the consecutive fringes allows for measurement of the refractive index of the medium between the surfaces.¹⁷

The SFA presents several unique advantages to the many other techniques available for surface characterization. First, the SFA has the ability to measure *absolute* surface separation (distances) as opposed to displacement or *relative* distances that are measured by AFM. Thus, the SFA allows for measuring the force vs. the absolute distance between the surfaces, and then the measurements can be fitted to well-known colloidal force models, e.g., the Derjaguin, Landau, Verveij, and Overbeek (DLVO) model.^{23,24} Second, the SFA can visualize (with a lateral resolution of 1 micron and sub-nm vertical resolution) the contact area and contact zone deformations (surface shape) during force measurements as seen in **Figure 2.1c**, which is necessary for converting the measured force to energy and to observe dynamic processes and deformations of the surface *in situ* (e.g., wear tracks, particle build-up, and condensed capillary bridges), respectively.¹⁷ Third, the SFA can study extended surfaces (i.e., those with radii of curvature > 1 cm) with atomically smooth mica surfaces (RMS roughness of about 0.1 nm) which allows for measurement of short- and long-range forces. Atomically smooth surfaces are required to accurately measure short-range forces, such as van der Waals and hydration forces that occur at less than 3 nm separation.²⁵ Direct measurement of the absolute distance and surface profile with 0.1 nm height resolution has enabled characterization of the physical interactions (e.g., van der Waals, electrostatic, hydration, etc.) for various interfaces

and physico-chemical processes, making the SFA the standard techniques for static and dynamic surface and interfacial science characterization.

While the SFA (and related techniques including the AFM) has proven to be an invaluable characterization technique for surface and interfacial phenomena,^{26,27} there are several significant challenges that inhibit widescale use. One of the biggest challenges is the need for atomically smooth surfaces to measure short- and long-range interaction forces, which results in the use of primarily single-crystalline sheets of mica for the surfaces. If the surface roughness is larger than the interaction regime of the forces, it is difficult to distinguish the true forces from steric repulsion of overlapping asperities. Hand-cleaving single-crystalline sheets of mica approximately 2-3 μm thick (for optimal resolution using the FECO technique) is difficult and time-consuming, providing another barrier to widespread use of these techniques. Furthermore, the mica surfaces must be prepared immediately before use to avoid surface contamination, thus new surfaces must be made before each experiment. Due to mechanical degradation of the mica surface during experiments or with cleaning, the mica surface is usually limited to a single experiment. For example, aggressive solvents will dissolve the exposed glue layer and aggressive sonication will result in mica cleaving. Another major challenge with mica is that its basal plane does not readily react, which makes it difficult to modify the surface chemistry to produce new interfaces.²⁸ Current studies are limited to a small number of polymer-reacted mica surfaces,^{29,30} thin-film metal deposition,^{1,31} and some physisorbed bilayer systems.³² Many of these surfaces are prepared by deposition on traditional mica surfaces which is difficult due to the heterogeneous nature and low reactivity of the mica surface. Each of the above challenges has limited the functionality of many optical and surface probing techniques and further advancements are stagnated while the mica surface

preparation is the only readily available method for producing surfaces capable of force measurements.

Here, we present a new method for making *composite surfaces* for the SFA and other optical/interferometric techniques. The same method can be used for making surfaces for its derivatives and for other interferometric techniques as well. These composite surfaces overcome the limitations of traditional mica surfaces while broadening the functionality required for use in interferometric and physico-chemical probing techniques. The new composite surfaces have 4 main advantages over traditional mica surfaces: First, the top layer is silica, which can be more easily modified using well-known silane chemistry procedures. Second, these composite surfaces can be cleaned more effectively than mica surfaces (e.g., with solvents, plasma, UV ozone, or by etching a few nm off of the surface), and reused for several experiments, for at least nine consecutive days in aqueous solutions before degradation occurs (compared to approximately 2-3 days for traditional mica surfaces). Third, these composite surfaces can be mass produced ahead of time and remain stable for at least four months in ambient conditions or under vacuum. Fourth, the reflective, buried polymer, and silica layers can all be adjusted to tune to the optical (including making a reflective layer with a specific bandwidth), electrical, structural (including roughness), and mechanical properties of the surfaces. Additionally, the metal reflective layer can serve as a protected electrode for studying electrochemical systems, similar to experiments performed using the electrochemical SFA (EC-SFA).⁴⁸ Like glued mica surfaces, the new composite surfaces maintain the ability to deform upon contact which makes it possible to measure the (finite) contact area and surface forces, and hence energies, due to the compressible polymer sub-layer.

In this work, we describe the fabrication of the composite surfaces using standard deposition techniques to achieve ultra-smooth (roughness RMS < 0.4 nm), silica surfaces with a compressible sub-layer supporting white-light interferometry and other optical techniques. The characterization of the fabricated disks is reported along with the tunability of surface roughness by varying the silica deposition parameters (and mechanical compliance by varying the polymer chemistry). Then, we show that the double-layer forces, measured with the composite surfaces, are comparable to those predicted by the electrostatic double-layer theory. We also describe various methods to modify the surface chemistry of the silica through deposition, chemisorption, and physisorption. We demonstrate the preparation and measurement of hydrophobic interactions between two octadecyltrichlorosilane (OTS) modified surfaces using standard, well documented silane chemistry techniques.^{33,34} The successful fabrication of an ultra-smooth, chemically modifiable, and compressible silica surface (i.e., *composite surfaces*) for the SFA, and other optical/interferometry techniques, provides a new surface that overcomes the difficulties associated with traditional mica surfaces to improve the accessibility of interferometry techniques and the number of distinct surfaces that can be studied.

2.3 Experimental Methods

2.3.1 Fabrication of silica surfaces

Prior to fabrication, the SiO₂ substrates (a 10 mm diameter, 2 cm radius cylindrically-curved disk for the surfaces presented in the above experiments) were cleaned for 1 hour in a piranha solution (3:1 H₂SO₄:H₂O₂). The substrates were sonicated in acetone, isopropanol, and DI H₂O for 2 minutes each at 80°C and subsequently dried at 180°C in an oven for 3

minutes. After the dehydration bake, the SiO₂ substrates were plasma cleaned in O₂/plasma at 300 mT and 100 W for 2 minutes to ensure no organic contaminants remained on the surface. A 3 nm-thick layer of Ti deposited with an electron beam evaporator (e-beam evaporator, Temescal CV-6S) on top of the SiO₂ substrate served as a sacrificial layer to facilitate repurposing of damaged fabricated surfaces.

An approximately 120 μm-thick SU-8 (SU-8 3050, MicroChem) epoxy negative photoresist layer was spin-coated on top of the Ti layer by spinning at 300 rpm for 30 seconds followed by 1000 rpm for 120 seconds with a ramp of 100 rpm s⁻¹. The SU-8 layer was reflowed at 95°C for 15 minutes before curing the polymer with i-line exposure (365 nm wavelength UV radiation) in a 7 mm circle on the 10 mm disk using a shadow mask for 1 minutes and 30 seconds at an intensity of 4,800 μW cm⁻². A post exposure bake for 5 minutes at 55°C followed by 15 minutes at 95°C with a ramp of 5°C min⁻¹ was used. The SU-8 was allowed to cool for 10 minutes before developed with propylene glycol methyl ether acetate (PMGEA, SU-8 developer, MicroChem) for 30 seconds. The SU-8 layer was rinsed with fresh PMGEA and isopropanol and air dried. The substrates were heated at 55°C for 5 minutes and 150°C for 30 minutes using a ramp rate of 5°C min⁻¹ to fully cure the SU-8 layer. The mechanical properties of the polymer layer, such as modulus of elasticity, can be tuned by adjusting the polymer density/type used though it was not done within this paper.

A 3 nm-thick Ti layer was deposited by e-beam evaporation (Temescal CV-6S) on top of the SU-8 layer to serve as an adhesion promoting layer, followed by 50 nm of Ag which serves as the reflecting layer for interferometry applications, and finally another 3 nm-thick Ti layer for adhesion promotion. The optical properties, such as bandpass wavelengths or reflectance, of the multi-layered surfaces can be adjusted by utilizing different reflecting or semi-reflecting

layers. The final, approximately 800 nm, SiO₂ layer is deposited by radio frequency (RF) sputtering at 300 W with a RF bias of 80 W which has a RMS roughness of 0.32 ± 0.05 nm for the smoothest surfaces produced. Further modifications to the surface chemistry can be made via additional depositions of various inorganic and metal materials, including oxide and nitride variations, adsorption of self-assembled monolayer or bilayer films, or chemical reactions with the surface through various silane chemistry reactions.

2.3.2 Octadecyltrichlorosilane (OTS) silica surface modification

Octadecyltrichlorosilane [OTS, CH₃(CH₂)₁₇SiCl₃, purity 90%, Aldrich Co., Ltd] was prepared with a concentration of 0.1 mM at 295 K using 100% toluene as the solvent for the silane reaction. OTS was added to the solvent and the surfaces were submerged for 12 and 24 hours under vacuum, as the organic silanes will react with moisture in the air to polymerize. After the allotted reaction time, the OTS-modified surfaces were rinsed with approximately 5 mL of chloroform to wash away excess, unreacted silane deposits. The surfaces were dried with N_{2(g)} and stored in a desiccator until measurements were performed in the SFA.

2.3.3 Characterization of thin film physical properties

Ellipsometry measurements were performed to verify the refractive index of the deposited thin films using a Woolam M2000DI variable angle spectroscopic ellipsometer. Measurements were taken at 45, 60, and 75 degrees to provide the widest flexibility for characterization of the optical properties of the deposited films.

Atomic force microscopy (AFM) measurements were performed to characterize the surface roughness of the fabricated disks under different deposition conditions and after surface modification procedures using a Dimension 3100 AFM system from Veeco, operated

in contact mode to maximize resolution in the z-direction for both the dense SiO₂ surfaces and elastic OTS surface layers.

2.3.4 Surface force measurements using the SFA

SFA measurements were performed with an SFA 2000 (manufactured by SurForce LLC., Goleta, California) to measure the electrostatic and hydrophobic interaction forces between symmetric SiO₂ and OTS-modified SiO₂ surfaces. The surfaces were fabricated as discussed above, on cylindrically curved silica disks ($R \approx 2$ cm) and mounted in the SFA in a crossed cylinder geometry. Prior to all SFA experiments, the SFA system was allowed to fully equilibrate at room temperature (295 K) until no drift was observed. For the SFA experiments involving the OTS-modified surfaces, the SFA was filled with deaired, deionized water to reduce the formation of air bubbles between the surfaces. FECO interferometry was used to measure the surface separation and shape during the experiment and the interaction forces were determined from the deflection of calibrated force measuring springs.

2.4 Results and Discussion

2.4.1 Characterization of the fabricated ultra-smooth SiO₂ disks

Figure 2.2a illustrates the structure of the fabricated composite surfaces exposing the top-most silica surface. A high-density photopolymer, SU8 3050, was spin-coated on a fused silica substrate to create a circular, compressible layer with a Young's modulus of approximately 2.0 Gpa.³⁵ The compressible SU8 layer was made with a smaller radius than the substrate to improve the stability and lifetime of the fabricated disks by encapsulating and effectively sealing the layered structure, preventing ingress of water that would delaminate the deposited layers.

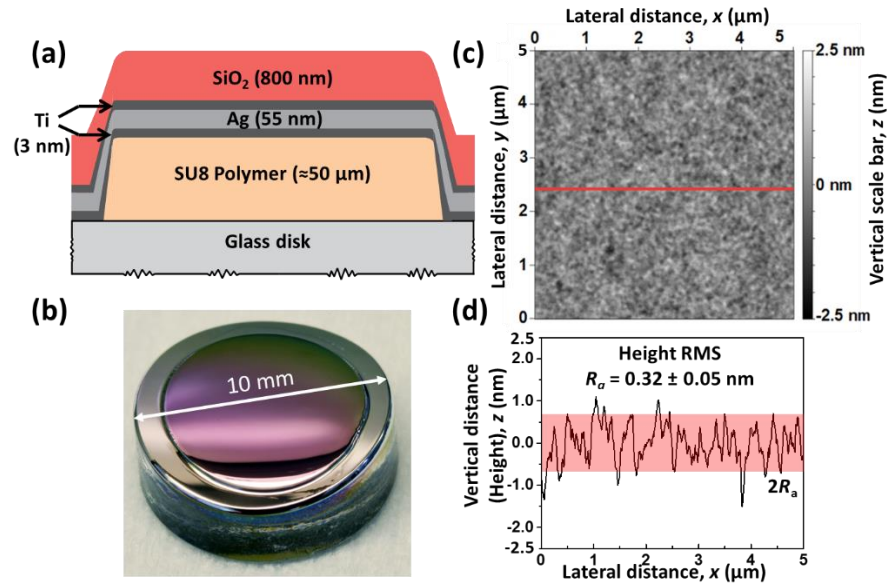


Figure 2.2 (a) Schematic of the fabricated SiO₂, cylindrically curved surfaces which uses a compressible SU8 layer island covered with Ti, Ag, Ti, and SiO₂ to allow surfaces to be used with interferometry techniques. (b) A picture of the actual 10 mm disks post fabrication. (c) AFM scan of the fabricated disk surface roughness with the red line indicating the slice shown below. (d) The roughness average of this surface is $R_a = 0.32 \pm 0.05$ nm and the shaded region illustrates $2R_a$.

A reflective layer of silver (approximately 50 nm thick) is electron-beam deposited between two adhesion-promoting 3 nm titanium layers on the SU8 polymer. At this thickness, the silver reflective layer has high reflectivity, low absorbance, and approximately 1% transmittivity in the visible light regime, making it suitable for use with spectroscopic and interferometry techniques. A final 800 nm layer of silica is radio frequency (RF) sputter coated on top of the Ti adhesion-promoting layer to provide a thick dielectric material for use in interferometry and spectroscopy measurements (the 800 nm silica layer gives good FECO resolution; a thicker layer will increase the roughness while a thinner layer comprises the FECO technique). The RF sputter technique prevents charge build-up and defects from forming as opposed to typical direct current (DC) sputtering.³⁶ The deposited silica layer using RF back-sputtering is denser compared to other vacuum deposition techniques,^{49,50} resulting

in stable, non-porous silica, similar to fused silica, which is ultra-smooth (RMS of 0.32 ± 0.05 nm, as measured by AFM) and does not absorb significant amounts of water in aqueous environments – a common issue with non-optimized deposition methods of silica-like materials.³⁷ In an aqueous environment, the porous silica layer thickness increases a few nanometers due to hydration of the surface; however, water can also be absorbed by the porous silica film, which increases the refractive index of the layer as air is replaced by water (from air with refractive index of 1.00 to water of 1.33). The increased refractive index of the silica film causes an ‘apparent’ swelling of the surfaces, thereby increasing the measured optical thickness from a few to tens of nanometers, that can be measured to $\pm 1 \text{ \AA}$ with multiple beam interference fringes (FECO).⁵¹ The deposited silica films used in this work show no such shift in the fringe position, within $\pm 1 \text{ \AA}$, indicating that the RF-sputtered silica films are not porous and do not absorb any measurable amounts of water. The electron-beam and sputter deposited materials coat the entire substrate surface area, encapsulating the compressible polymer layer and enhancing stability of the composite surface, as previously mentioned. The fabricated SiO₂ surfaces can be cleaned with a variety of solvents, including organic solvents, strong acids, or even basic solutions, as well as standard thin film cleaning techniques such as O₂/plasma. Acid etch cleaning can remove 1-2 nm of silica to remove chemisorbed films so that the same set of fabricated surfaces can be reused many times over before the silica becomes too thin or rough for use in various experiments.³⁸ Furthermore, the surfaces can be handled and stored for long time as the silica surface is robust (in contrast to mica surfaces that are very fragile and easily scratched or damaged). Composite surfaces, that were exposed to an aqueous environment, remained stable for up to nine days of experimentation before delamination (i.e., failure) occurred. Unstable composite surfaces show clear signs of

delamination of the deposited layers, such as cracks, hairlines, etc. These signs can be clearly seen by the naked eye and as distortions in the fringe position of the FECO (by a few hundred nanometers) due to the varying distance between the reflective layers, as shown in **Figure 2.3**.

(a) Delaminated composite surface (b) FECO of delaminated composite surface

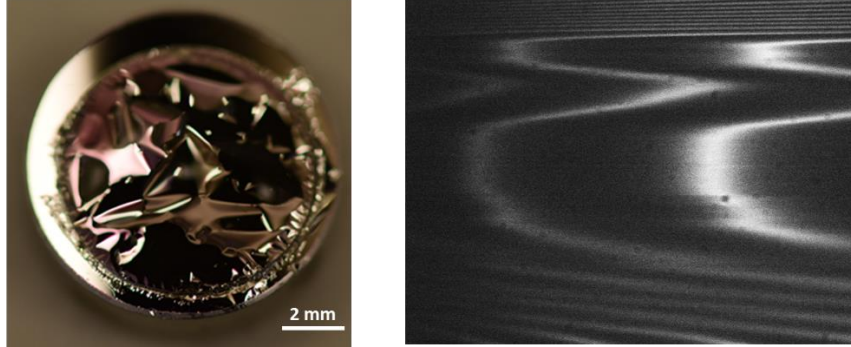


Figure 2.3 (a) Final stages of failure of the composite surfaces and (b) the resultant distortions in the FECO after exposure to deionized water after a period of eight days. The initial stage of failure is due to penetration of the aqueous solution at the edges of the disk, through cracks and defects present on the disk itself before deposition, which causes the deposited metal and silica layers to delaminate from the base silica disk and SU8 layers. Once the initial delamination occurs, it propagates quickly through the entire composite surface over a few hours and results in catastrophic failure of the surfaces as demonstrated by the release of the deposited silica and metal layers.

Signs of delamination typically appeared after approximately nine days of use in aqueous environments, and these cracks and hairlines quickly (within a few hours) led to failure of the deposited layers. The delamination of the silica and metal layers (or loss of metal-SU8 adhesion) is caused by water penetrating along the edges of the surface through defects and cracks present on the base silica disk before deposition. If stored in ambient conditions, the fabricated surfaces have a shelf life of at least 3-4 months before initial signs of delamination are observed. These features assist in removing one of the largest barriers to current SFA use, the surface preparation procedures, and facilitates the expansion and growth of surface force characterization and other optical/interferometry techniques. The complete silica composite surface is shown in **Figure 2.2b** when deposited on a cylindrically-curved ($R = 2$ cm) disk,

though the process is easily modified to work with flat and spherical geometries as well. See the experimental section at the end of the paper for exact details regarding fabrication.

For the composite surfaces to be relevant and useful for accurate measurements of surface and interface phenomena, the roughness of the surfaces must be carefully controlled to satisfy desired conditions. In many cases, surface force measurements require a knowledge of the contact area and very smooth surfaces, sub-nanoscale roughness, to accurately measure surface forces such as hydration (at separation distances < 3 nm), electrostatic (at separation distances < 10 nm), and adhesion forces. **Figure 2.2c** shows a representative atomic force microscopy (AFM) scan of the fabricated surfaces using an RF backsputter power, P_{RF} , of 80 W. The single scan highlighted in **Figure 2.2d** demonstrates that the surfaces are randomly rough with a mean roughness of 0.32 ± 0.05 nm and a peak-to-peak roughness of 1.3 nm, which is acceptable for measuring surface forces and roughness in most systems, especially those of engineering interest.

The bulk mechanical properties, such as the modulus of elasticity or coefficient of thermal expansion, can also be readily modified by adjusting the SU8 polymer used in the compressible layer. This can be adjusted independently of the surface chemistry (of the silica surface) to allow for combinations of surface chemistry and modulus of elasticity that are unobtainable for most current systems, including the JKR apparatus and SFA.

In addition to modifying the surface chemical and bulk mechanical properties, there are systems where modifying the surface roughness is desired to observe the effect of changing roughness on surface interactions and/or chemical processes. The surface roughness can be modified by adjusting the RF sputter deposition parameters, especially the height, pressure, and backsputtering power, P_{RF} . By adjusting any of these conditions, the desired surface

roughness can be tailored as measured by AFM and is demonstrated in **Figure 2.4** through variation of P_{RF} . Further exploration of the various deposition parameters would allow for a greater variation in obtainable surface roughness.

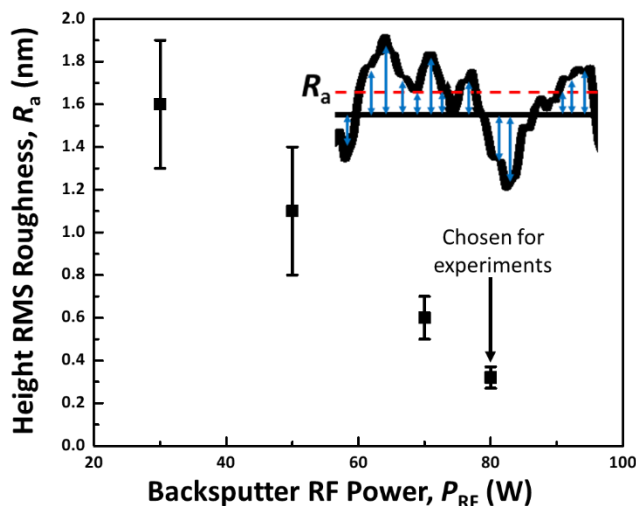


Figure 2.4 The surface roughness of the composite surfaces can be controlled through variation in radio frequency (RF) power, PRF, during RF sputtering of the SiO₂ layer. For the composite surfaces with different surface roughness, no shift in the FECO position or film thickness was determined to within $\pm 1 \text{ \AA}$ in aqueous environments, indicating that no observable change in the porosity occurred. The vertical bars at each data point represents the variance in the average surface roughness, R_a . The inset picture is a representation of how R_a is determined by averaging the height of each peak and valley, using evenly spaced points, across the sample.

The composite surfaces with tunable random roughness should allow for the direct measurement of the effects of random or patterned roughness on the forces and friction between extended surfaces in a variety of systems, which has previously been difficult to measure due to the limited capabilities of traditional mica surfaces in the SFA. Additionally, there are systems which are naturally rough where understanding the effects of roughness on different surface forces is necessary to understand the relevant parameters in surface and interface processes, as is relevant in the adhesion of bio-organic membranes³⁹ as well as the effect of roughness on electrostatic forces in battery-like environments.⁴⁰

2.4.2 Double layer interactions using the fabricated disks

The ultra-smooth silica layer (RMS roughness < 0.4 nm) allows for measurement of surface forces in the SFA with accuracy and resolution comparable to traditional mica and other surfaces that have perfect cleavage. **Figure 2.5a** shows the FECO for the fabricated surfaces in a cross-cylinder geometry for an 800 nm thick silica layer with a 50 nm reflective silver layer. The smooth surfaces are comparable to the FECO of traditional mica surfaces shown in **Figure 2.1c** and show significant compressibility to indicate the flattening of the surfaces in hard contact. The diameter of the totally flattened area, ϕ , at the same contact wavelength, λ_n , is 60 μm , showing that the adhering surfaces are molecularly smooth with no asperities or particles between them.

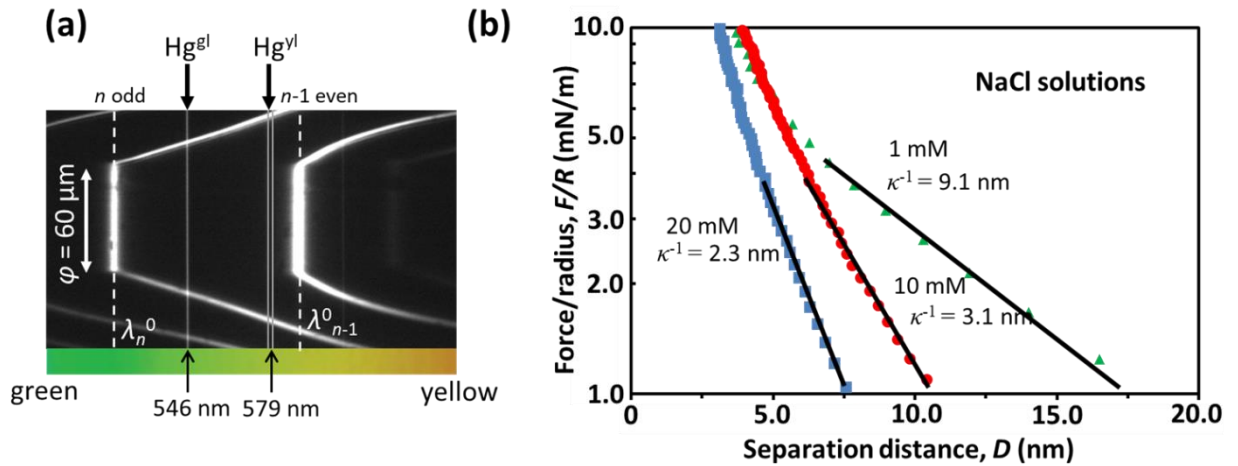


Figure 2.5 (a) FECO of fabricated SiO_2 (800 nm thick) surfaces in air using the SFA. Due to how thin the SiO_2 layer is, the wavelength regime that fringes span is larger for the fabricated surfaces compared to traditional mica SFA. (b) Force runs in varying concentration (1, 10, and 20 mM) NaCl solutions using the fabricated surfaces. The double-layer decay length, κ^{-1} , for electrostatic forces was fit using an exponential function. The theoretical decay lengths for 1, 10, and 20 mM NaCl solutions are 9.6 nm, 3.0 nm, and 2.1 nm, respectively. The measured decay lengths were all within 10% of the theoretically predicted values. The measurements were performed and verified over the course of 72 hours using surfaces previously stored for one month at 22°C and 600 mT.

Previous studies in the literature have studied surface forces on silica in different environments by depositing thin-films of silica onto mica or with thin sheets of glass-blown silica. The deposited silica thin-films could not be thicker than 15 nm to avoid delamination due to internal stresses and still suffered from the stability issues of traditional mica surfaces.³⁷ The blown-glass silica surfaces are significantly thicker than typical hand-cleaved mica sheets and not cylindrical, reducing resolution and complicating the contact geometry. The new composite surfaces provide new opportunities for surface force analysis with silica surfaces that were previously unobtainable.

The composite silica surfaces were used to measure the van der Waals and electric double-layer forces between the two silica surfaces in various NaCl solutions as shown in **Figure 2.5b** to verify the accuracy of the force measurements with the fabricated surfaces. The force runs for silica composite surfaces in 1, 10, and 20 mM NaCl were fit with exponentials to give decay lengths of 9.1, 3.1 and 2.3 nm, respectively. The values for the decay lengths were within 10% of the theoretically predicted values (Eq. (14.37) in ref. 25) for 1:1 electrolytes for dynamic force runs. Additionally, the van der Waals adhesion force/radius, F/R , was measured in air to be 11.5 mN m^{-1} while the theoretical force calculated using $F/R = -A/6D^2$ for cross-cylinder surfaces was -10 mN m^{-1} .²⁵ The accurate measurement of surface forces with the composite silica surfaces in NaCl solutions demonstrates that the composite surfaces match the force measuring capabilities of traditional mica surfaces yet have the advantage of tunability and reusability as previously discussed.

2.4.3 Surface chemistry modification through silane chemistry

The benefit to composite silica surfaces is that silica (and its glassy variants) is one of the most broadly used inorganic materials across a multitude of fields. As such, the manipulation,

chemical modification and functionalization of SiO₂ materials is well documented and characterized, providing a vast library of references for modification procedures that can easily be adopted to work on the composite surfaces.^{41,42} **Figure 2.6** demonstrates a few of the methods typically used to modify SiO₂ materials, such as deposition, chemical reactions, or adsorption, which can be extended to modification of the composite silica surfaces. Using these procedures, the surfaces and interfaces available to the scientific community can be greatly expanded to allow for measurement of interfaces that are more like those of fundamentally and technologically relevant systems.

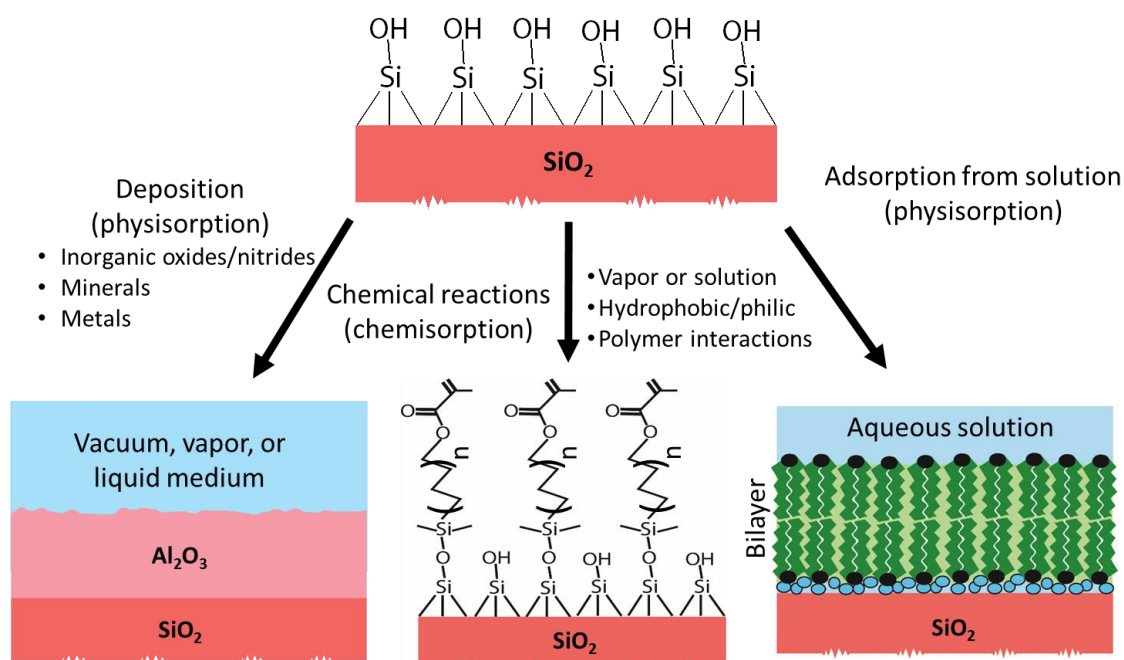


Figure 2.6 Different ways through which the silica fabricated disks can be modified via chemical reaction (i.e., chemisorption), deposition (i.e., physisorption), adsorption from solution, etc. to produce novel inorganic/organic surfaces for surface and interface analysis in a variety of environments.

The application of silane reaction chemistry highlights an example of how the composite surfaces can be modified. The octadecyltrichlorosilane (OTS) (dissolved in toluene) adsorbs and reacts with the silanol groups of the silica composite surfaces, which changes the hydrophobicity of the surface drastically from fully-wetting (hydrophilic) to hydrophobic with

a contact angle of approximately 110° .^[34] Here, the initially unmodified silica composite surfaces have a water contact angle of 0° and water will fully wet the surface due to the hydrophilic nature of the partially-silanated surface. **Figure 2.7** shows how the water contact angle of the unmodified SiO₂ surfaces goes from 0° to 105° after reaction with OTS for 12 hours, and to 112° after a reaction with OTS for 24 hours, which indicates an extremely hydrophobic surface and successful modification. Recently, OTS-modified mica surfaces were prepared which were used to study OTS interface interaction mechanisms.⁴⁵ Due to the low reactivity of the mica surface, the OTS-modified surfaces had significantly lower contact angles compared to traditional OTS self-assembled monolayers reported here and in the literature.

OTS layers after different reaction times, t_r , on the composite silica surfaces

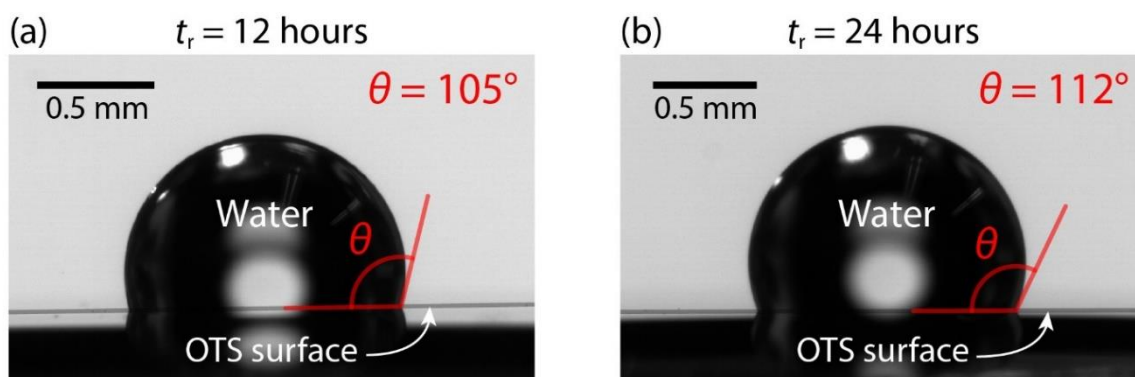


Figure 2.7 Measured water contact angle for OTS-modified composite silica surfaces at (a) 12-hour and (b) 24-hour reaction times (t_r) in OTS. The grey line indicates the actual position of the OTS surface as the reflective layer of the disks creates a reflection that is observed below this line. The unmodified SiO₂ surface of the fabricated disks demonstrated complete wetting (water contact angle of 0°).

The reaction of alkylchlorosilane compounds at silica surfaces have been widely studied and is known to form a self-assembled monolayer which has applications in passivating layers, anti-stiction coatings, and preparation of functional materials.^{43,44} Using the SFA, the

interactions of the OTS surfaces in aqueous environments can be studied to understand their adhesion and passivating properties which are important to a wide range of systems.

The result of an OTS modification of the composite silica surfaces can be observed by direct changes in the FECO fringes, as seen in **Figure 2.8**. The silica surfaces were coated with OTS using a reaction time, t_r , of 12 hours using OTS in toluene and the roughness of the surfaces slightly increased, as can be seen by the broadening of the FECO fringe near contact in **Figure 2.8b**. The increased roughness is confirmed using an AFM which shows an increase in RMS surface roughness from 0.35 to 0.72 ± 0.05 nm (see **Figure 2.8d**). Using the slight shift in the positioning of the fringes, the thickness of the OTS layer on each surface was determined to be around 8 nm, which suggests approximately three layers of OTS remain on the surface. A longer reaction time, t_r , of 24 hours, presented in **Figure 2.8c**, results in further broadening of the FECO fringe at contact, indicating a larger increase in roughness of the surfaces. Due to the highly compressible nature of the film, quantitative determination of the roughness using AFM was too difficult.

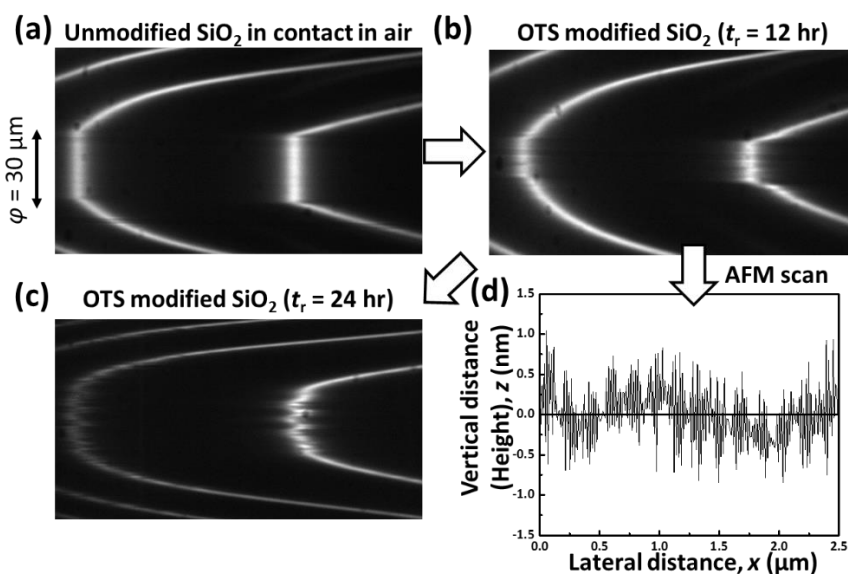


Figure 2.8 FECO for (a) as-fabricated, unmodified SiO₂ surfaces, (b) OTS modified SiO₂ surfaces with 12 hours of reaction time, and (c) OTS modified SiO₂ surfaces with 24 hours of reaction time (t_r) in contact in air using the SFA. The increase in roughness is apparent through the increased variation in intensity at contact along the fringe. (d) Roughness characterization of the OTS modified SiO₂ surfaces with 12 hours of reaction time by AFM. The RMS roughness has increased from 0.35 nm for the unmodified surfaces to 0.72 ± 0.05 nm.

Figure 2.9 shows the physical effects of the OTS multilayer formed on the SiO₂ surface, we measured the interaction forces between two OTS-modified SiO₂ surfaces ($R \approx 2.5$ cm) in de-ionized water using the SFA. A strong, hydrophobic adhesion force was measured during separation, again indicating successful modification of the surfaces compared to the unmodified surfaces which only exhibited DLVO forces with no hydrophobic adhesion. The strong adhesion force $F_{ad}/R = 270 \pm 20$ mN m⁻¹, which corresponds to an interfacial energy of $W_0 = 58 \pm 4$ mJ m⁻², of the two OTS surfaces is due to interaction between the hydrophobic chains of the OTS on each surface, with the adhesion energy $W_0 = 2F_{ad}(D_j)/3\pi R$ given by the JKR theory.²⁵ The strong hydrophobic adhesion force measured was of similar magnitude to the hydrophobic adhesion measured using the SFA for hexadecyltrimethylammonium bromide (CTAB) of approximately 100 mN m⁻¹.⁴⁶ This verifies the success of the silanol chemistry-based surface modification procedure to produce OTS surfaces. Further analysis of these OTS surfaces in different interfaces and environments can yield new insights into their role in passivation layers and anti-stiction coatings that were previously inaccessible due to the limitations in current surface and interface characterization methods. This is especially important for the SFA which can easily measure the interaction forces, including friction and wear, with relevant interfaces and solution environments, though further investigation is beyond the current scope of this paper.

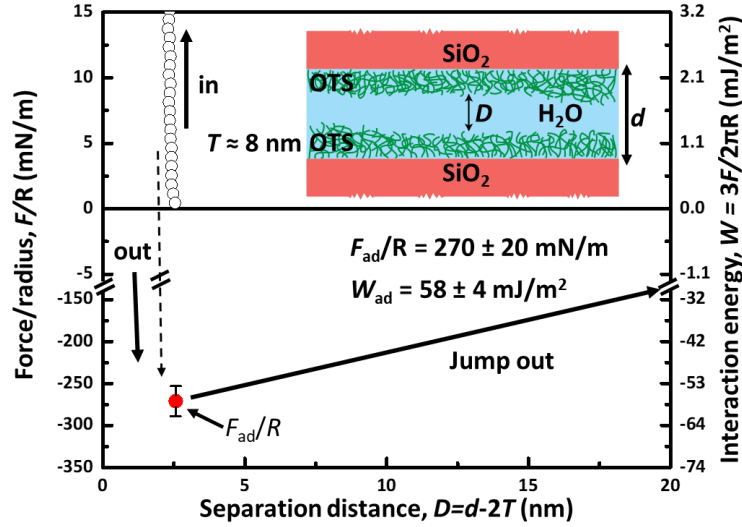


Figure 2.9 Measured adhesive hydrophobic interaction force for adsorbed layers of octadecyltrichlorosilane (OTS) on SiO_2 in deaerated, deionized H_2O . The adhesion force measured was $F_{ad}/R = 270 \pm 20$ mN m^{-1} which corresponds to an adhesion energy of $W_{ad} = 58 \pm 4$ mJ m^{-2} . The OTS reaction procedure was not fully optimized to form a perfectly smooth monolayer which is why there is separation even for hydrophobic surfaces in water. A typical error bar is shown for the measured adhesion forces.

2.5 Conclusions

We presented a procedure for fabricating ultra-smooth, deformable, chemically functional silica composite surfaces for the SFA, and other sub nano-scale optical/interferometric techniques, that drastically enhances the accuracy, range, and complexity of interfaces that can be studied using surface interaction measurement techniques. The composite surfaces include a compressible polymer layer to support monitoring contact mechanics and observing deformations (important for measuring the contact area), a reflective layer used for optical/interferometry measurements, and a silica terminal layer which is the exposed interacting interface that can be easily functionalized. Each of the layers can be modified to vary the physical (i.e., mechanical), optical, and chemical properties of the surfaces to simulate a broad range of systems of fundamental and practical interest. The surfaces are more robust than traditional (hand-cleaved) “model” mica surfaces commonly used in SFA, AFM,

and various characterization techniques that require molecularly smooth surfaces, and can be cleaned and reused for several different experimental setups over a prolonged period before failing, as compared to the single experimental use of mica surfaces. We also demonstrated the ability to vary the surface roughness from sub-nm to the nm scale (which is difficult with traditional mica surfaces). Finely-tuned modifiable surface roughness enables further studies of the effect of roughness on surface forces and interactions.

Using the composite surfaces, we accurately measured the electric double-layer Debye lengths (decay lengths) between silica in various weak electrolyte solutions, with an accuracy comparable to that achieved using mica surfaces. We propose that the top silica layer could be modified by deposition, adsorption, or reaction to control the chemical nature of the silica surface, and we demonstrated one method of modification through silanol reaction with OTS to form hydrophobic OTS multi-layers on the silica surface and quantitatively measured their strong hydrophobic interaction forces in water using the SFA.

We conclude that the procedure for generating fabricated composite surfaces opens new possibilities for experimental measurements and characterization techniques. For the SFA especially, these surfaces are capable of reproducing the force-measuring capabilities of traditional mica surfaces, but with the modifiability of silica that enables a much broader range of surfaces and interfaces to be fabricated using deposition, adsorption, or chemical reaction. Combining these new functionalities with the ability to also manipulate the mechanical properties (e.g., deformability) of the surfaces enables the study of more realistic systems that are relevant to engineering applications. Further applications of these composite surfaces to other techniques, like AFM, colloidal probes, or the JKR apparatus, may provide opportunities

to overcome limitations in current surface measurement techniques for studying previously unattainable surface phenomena across a multitude of scientific and engineering disciplines.

References

1. B. R. Shrestha, Q. Hu, T. Baimpos, K. Kristiansen, J. N. Israelachvili, M. Valtiner, *J. Electrochem. Soc.* **2015**, *162*, C327.
2. C. O. Laoire, S. Mukerjee, K. M. Abraham, E. J. Plichta, M. A. Hendrickson, *J. Phys. Chem. C* **2010**, *114*, 9178.
3. M. Soorholtz, L. C. Jones, D. Samuelis, C. Weidenthaler, R. J. White, M. M. Titirici, D. A. Cullen, T. Zimmermann, M. Antonietti, J. Maier, R. Palkovits, B. F. Chmelka, F. Schuth, *ACS Catal.* **2016**, *6*, 2332.
4. J. Van Aelst, D. Verboekend, A. Philippaerts, N. Nuttens, M. Kurttepel, E. Gobechiya, M. Haouas, S. P. Sree, J. F. M. Denayer, J. A. Martens, C. E. A. Kirschhock, F. Taulelle, S. Bals, G. V. Baron, P. A. Jacobs, B. F. Sels, *Adv. Funct. Mater.* **2015**, *25*, 7130.
5. E. D. Kaufman, J. Belyea, M. C. Johnson, Z. M. Nicholson, J. L. Ricks, P. K. Shah, M. Bayless, T. Pettersson, Z. Feldot, E. Blomberg, P. Claesson, S. Franzen, *Langmuir* **2007**, *23*, 6053.
6. E. Charlaix, J. Crassous, *J. Chem. Phys.* **2005**, *122*, 184701.
7. M. C. Audry, S. Ramos, E. Charlaix, *J. Colloid Interface Sci.* **2009**, *331*, 371.
8. Y. Niiyama, N. Shimizu, A. Kuwayama, H. Okada, T. Takeno, K. Kurihara, K. Adachi, *Wear* **2017**, *378–379*, 27.
9. M. Kasuya, K. Tomita, M. Hino, M. Mizukami, H. Mori, S. Kajita, T. Ohmori, A. Suzuki, K. Kurihara, *Langmuir* **2017**, *33*, 3941.

10. R. Carpick, M. Salmeron, *Chem. Rev.* **1997**, 97, 1163.
11. T. Pettersson, A. Naderi, R. Makuška, P. M. Claesson, *Langmuir* **2008**, 24, 3336.
12. D. W. Lee, X. Banquy, K. Kristiansen, Y. Kaufman, J. M. Boggs, J. N. Israelachvili, *Proc. Natl. Acad. Sci.* **2014**, 111, E768.
13. A. Perot, C. Fabry, *Astrophys. J.* **1899**, 9, 87.
14. J. Rädler, E. Sackmann, *J. Phys. II* **1993**, 3, 727.
15. A. Albersdörfer, T. Feder, E. Sackmann, *Biophys. J.* **1997**, 73, 245.
16. G. W. Greene, K. Kristiansen, E. E. Meyer, J. R. Boles, J. N. Israelachvili, *Geochim. Cosmochim. Acta* **2009**, 73, 2862.
17. J. N. Israelachvili, *J. Colloid Interface Sci.* **1973**, 44, 259.
18. J. Klein, *Nature* **1980**, 288, 248.
19. F. Restagno, J. Crassous, É. Charlaix, C. Cottin-Bizonne, M. Monchanin, *Rev. Sci. Instrum.* **2002**, 73, 2292.
20. J. L. Parker, H. K. Christenson, B. W. Ninham, *Rev. Sci. Instrum.* **1989**, 60, 3135.
21. P. Frantz, N. Agrait, M. Salmeron, *Langmuir* **1996**, 12, 3289.
22. A. Tonck, J. M. Georges, J. L. Loubet, *J. Colloid Interface Sci.* **1988**, 126, 150.
23. B. Derjaguin, L. Landau, *Prog. Surf. Sci.* **1993**, 43, 30.
24. E. J. W. Verwey, *Nature* **1946**, 631.
25. J. N. Israelachvili, *Intermolecular and Surface Forces, 3rd ed.*, Elsevier, USA **2011**.
26. J. N. Israelachvili, D. Tabor, *Proc. R. Soc. Lond. A.* **1972**, 331, 19.
27. W. A. Ducker, T. J. Senden, R. M. Pashley, *Langmuir* **1992**, 8, 1831.
28. Z. Z. Zhang, G. W. Bailey, *Clays Clay Miner.* **1998**, 46, 290.
29. G. Luengo, J. Pan, M. Heuberger, J. N. Israelachvili, *Langmuir* **1998**, 14, 3873.

30. S. H. Donaldson, S. Das, M. A. Gebbie, M. Rapp, L. C. Jones, Y. Roiter, P. H. Koenig, Y. Gizaw, J. N. Israelachvili, *ACS Nano* **2013**, *7*, 10094.
31. L. Chai, J. Klein, *Langmuir* **2007**, *23*, 7777.
32. Y. Min, K. Kristiansen, J. M. Boggs, C. Husted, J. a Zasadzinski, J. Israelachvili, *Proc. Natl. Acad. Sci.* **2009**, *106*, 3154.
33. A. Poda, A. Anderson, W. R. Ashurst, *Appl. Surf. Sci.* **2010**, *256*, 6805.
34. V. Kumar, P. Puri, S. Nain, K. N. Bhat, N. N. Sharma, *AIP Conf. Proc.* **2016**, 1724.
35. Microchem, SU-8 3000 Permanent Epoxy Negative Photoresist,
www.microchem.com, accessed: June, 2015.
36. P. D. Davidse, L. I. Maissel, *J. Appl. Phys.* **1966**, *37*, 574.
37. G. Vigil, Z. H. Xu, S. Steinberg, J. Israelachvili, *J. Colloid Interface Sci.* **1994**, *165*, 367.
38. J. K. Kang, C. B. Musgrave, *J. Chem. Phys.* **2002**, *116*, 275.
39. M. Benz, K. J. Rosenberg, E. J. Kramer, J. N. Israelachvili, *J. Phys. Chem. B* **2006**, *110*, 11884.
40. M. Valtiner, K. Kristiansen, G. W. Greene, J. N. Israelachvili, *Adv. Mater.* **2011**, *23*, 2294.
41. C. Haensch, S. Hoepfner, U. S. Schubert, *Chem. Soc. Rev.* **2010**, *39*, 2323.
42. J. B. Brzoska, I. Ben Azouz, F. Rondelez, *Langmuir* **1994**, *10*, 4367.
43. Y. Wang, M. Lieberman, *Langmuir* **2003**, *19*, 1159.
44. P. Fontaine, D. Goguenheim, D. Deresmes, D. Vuillaume, M. Garet, F. Rondelez, *Appl. Phys. Lett.* **1993**, *62*, 2256.

45. J. Huang, X. Liu, X. Qiu, L. Xie, B. Yan, X. Wang, Q. Huang, H. Zeng, *J. Phys. Chem. B* **2017**, *121*, 3151.
46. J. N. Israelachvili, R. M. Pashley, **1984**, *98*, 500.
47. A. Tulpar, Z. Wang, C.-H. Jang, V. Jain, J. R. Heflin, W. A. Ducker, *Nanotechnology* **2009**, *20*, 155301.
48. M. Valtiner, X. Banquy, K. Kristiansen, G. W. Greene, J. N. Israelachvili, *Langmuir* **2012**, *28*, 13080.
49. H. Fritzsche, C. C. Tsai, *Solar Energy Materials* **1979**, *1*, 471.
50. V. Godinho, P. Moskovkin, R. Alvarez, J. Caballero-Hernandez, R. Schierholz, B. Bera, J. Demarche, A. Palmero, A. Fernandez, S. Lucas, *Nanotechnology* **2014**, *25*, 355705.
51. J. Israelachvili, Y. Min, M. Akbulut, A. Alig, G. Carver, W. Greene, K. Kristiansen, E. Meyer, N. Pesika, K. Rosenberg, H. Zeng, *Rep. Prog. Phys.* **2010**, *73*, 036601.

Chapter 3: Electrochemically enhanced dissolution at confined, asymmetric interfaces

3.1 Electrochemically enhanced dissolution of silica and alumina in alkaline environments

3.1.1 Abstract

Using a surface forces apparatus (SFA), we determine the influences of electrostatic surface potential and ionic strength on the enhanced dissolution of alumina and silica in confinement (< 3 nm) with dissimilar charged surfaces in aqueous environments. We find more rapid dissolution of alumina and silica in close proximity to mica compared to isolated alumina or silica materials in bulk solutions, consistent with previous observations. Furthermore, we demonstrate that the dissolution of silica in close proximity with a gold electrode in weakly alkaline solutions depends directly on the applied electrostatic potential. We propose that the enhanced dissolution phenomenon arises from overlap of the electrostatic double layers between the dissimilar charged surfaces at small inter-surface distances (< 3 nm). A simple, semi-quantitative model shows that overlap of the electrostatic double layers changes the magnitude and direction of the electric field at the surface of the dissolving material, which our results suggest drives enhanced dissolution of the surface with the higher potential. We show that dissolution rates of silica and alumina may be increased by up to two orders of magnitude by changing the surface electrochemical properties and solution conditions. Our findings yield fundamental insights into the influences of electrostatics on dissolution processes at asymmetric solid-liquid-solid interfaces and provide new methods for manipulating dissolution with relevance for diverse technological applications.

3.1.2 Introduction

Dissolution of inorganic oxide materials, such as silica and alumina, plays a crucial role in the development and formation of macroscopic properties in many natural and technological systems, from structural materials^{1,2} to microelectronics^{3,4} and catalysts.⁵ Enhanced dissolution, defined as dissolution that is greater than the single-surface dissolution rate measured in the same bulk solution conditions, is observed at confined, asymmetric solid-liquid-solid interfaces. For example, increased dissolution is observed in many geologic environments at mineral-mineral grain boundaries (e.g., quartz-muscovite mica) in aqueous environments and is known as pressure solution.⁶ Chemical-mechanical polishing/planarization (CMP) of wafer materials is important for semiconductor processing and involves an aqueous slurry of silica particles used to polish a wafer of a much harder material.^{7,8} Inorganic polymer binders are produced from partial dissolution and condensation of aluminosilicate particles in a dense slurry under highly alkaline conditions to form high-strength cementitious networks with applications for low-CO₂ structural materials.^{9,10} Inorganic oxide materials with applications for drug delivery and heterogeneous catalysis have been shown to crystallize via non-classical mechanisms involving dissolution and reprecipitation of precursor species in alkaline conditions.^{5,11,12} In each of these examples, dissolution of surface silica or alumina species in aqueous environments is an important step in the development of macroscopic properties of interest, such as compressive and tensile strength in cements, resistance to corrosion in structural materials, increased material removal rates for semiconductor processing, or pore structure of porous oxide catalyst supports.

As dissolution of alumina and silica materials is important for many different applications, the kinetics of silica and alumina dissolution under a variety of technologically

relevant conditions have been widely characterized; however, the mechanism of silica and alumina dissolution remains poorly understood.¹³⁻¹⁵ Specifically, the fundamental physico-chemical driving forces related to differences in dissolution rates in different aqueous environments are still largely unknown.¹⁶⁻¹⁸ Improved understanding of enhanced dissolution of inorganic oxide materials, especially silica and alumina, will yield improved understanding of many industrial processes, ranging from CMP of oxide materials to formation of structural materials.

Under most conditions, inorganic oxide materials such as silica and alumina exhibit very low dissolution rates; however, under certain aqueous conditions, dissolution rates of silicates and aluminates in asymmetric, confined solid-liquid-solid interfaces have been observed to increase dramatically. For example, Greene et al. studied a natural phenomenon known as “pressure solution,” where mineral solubility increases at grain boundaries with ground water present. This phenomenon had previously been attributed to high pressures under the geologic conditions.^{19,20} At such confined solid-liquid-solid interfaces, muscovite mica has been observed to penetrate into quartz (e.g., a silica material), despite the fact that mica is significantly softer than quartz.²¹ It was concluded that quartz had dissolved along the quartz-mica interface, allowing the mica to penetrate through the significantly harder quartz grain. Greene et al. studied dissolution at the asymmetric silica-water-mica interface and found that the silica surface exhibited enhanced dissolution, even without high geologic pressure.²² Further work by Kristiansen et al. showed that the pressure solution phenomena depended on the relative potentials of the surfaces under the same geologic solution conditions.²³ However, the relationship between surface electrochemical properties and

dissolution rates has not been determined for surfaces in other geologic and non-geologic solution conditions.

Enhanced dissolution phenomena are also observed in chemical-mechanical polishing (CMP) of inorganic materials, such as silicon or aluminum wafers for semiconductor processing, where dissolution rates and material removal rates are orders-of-magnitude faster than the rates of dissolution of single isolated surfaces. The origin of the increased dissolution rates is widely debated. A leading explanation for the enhanced dissolution observed in CMP is that chemical reactions of the solution with the surfaces form surface layers that are softer than the bulk material of the substrate. For example, previous studies show that colloidal particles tens to hundreds of nanometers in diameter or polishing pads with micron-scale roughnesses can polish wafer materials to achieve sub-nanometer surface roughness.⁸ The polishing of silicon wafers with alumina nanoparticles has been suggested to proceed through formation of surface aluminosilica layers that are susceptible to mechanical abrasion, resulting in increased dissolution rates and polishing of surfaces.^{4,24} This hypothesis is in contradiction with well-established evidence suggesting that the limit of surface roughness achievable in mechanical polishing processes depends on the roughness of the material used to polish the substrate.²⁵ The disparity between the roughness of the abrading surface and the much lower roughness of the polished surface calls for a new explanation for dissolution of the surface layer. Moreover, the relationship between the composition of the colloidal slurry, electrolyte concentration, pH, and the observed dissolution rates are only empirically understood.⁴ Further studies on the physico-chemical driving forces influencing the dissolution phenomena are required to develop a deeper understanding of enhanced dissolution and better control of CMP processes. However, similar to the pressure solution phenomenon, the CMP process can

be considered as an asymmetric solid-liquid-solid interface in nanoscale proximity due to the high-density slurry used to polish the wafer materials.

In this work, we studied the enhanced dissolution of alumina and silica in close proximity to muscovite mica (i.e., silica-solution-mica or alumina-solution-mica). Using a surface forces apparatus (SFA), we measured the dissolution of alumina and silica materials in confinement with mica under different weakly alkaline, solution conditions. We find more rapid dissolution of alumina and silica in close proximity to mica when compared to single-surface dissolution of alumina or silica in similar bulk solutions, consistent with previous results. We propose that this dissolution enhancement results from changes in the electrostatic potential distribution between the asymmetric surfaces due to overlap between electrostatic double layers. We also demonstrate that the dissolution rate of silica in contact with a gold electrode, under similar weakly alkaline solution conditions, can be directly manipulated by changing the applied potential of the gold electrode. Based on these results, we propose that the dissolution enhancement results from changes in the electrostatic potential distribution between the asymmetric surfaces due to overlap between electrostatic double layers. Our findings support a general concept for dissolution enhancement based upon the surface electrochemical properties and solution conditions, which can be applied to manipulate dissolution rates by several orders of magnitude for typically slow-dissolving alumina or silica materials.

3.1.3 Experimental methods

3.1.3.1 Surface forces apparatus dissolution measurements

Dissolution measurements of the change in silica and alumina nanoparticle height, Δd , were performed using a Surface Forces Apparatus (SFA). A detailed description of the SFA technique can be found in Ref. 26 and a schematic of the instrument is shown in **Figure 3.1**. Briefly, the distance between the surfaces was monitored with multiple beam interferometry and controlled with a piezoelectric crystal or micrometer. The deflection of a double cantilever spring was used to determine the interaction force between the two surfaces. Using the SFA, distances and forces are measured with experimental errors of $F/R = \pm 0.02$ mN/m and $D = \pm 2$ Å.

Amorphous SiO₂ 25-50 wt% solutions of 200 ± 50 nm (NanoComposix, 10 mg/mL suspension in water) and polycrystalline Al₂O₃ (puriss., $\geq 99.8\%$ Al₂O₃ basis) colloidal nanoparticle solutions were prepared in an aqueous solution made using de-ionized water (3 MΩ·cm, TOC < 7 ppb), pH 10 to 11, 0 to 10 mM NaCl. The nanoparticle solution was injected between two freshly prepared single-crystalline mica surfaces. with the surfaces were then compressed to 2-3 atm, compressing 1-3 nanoparticles in the contact area, and the height of the particle is measured to ± 3 Å using interference fringes (fringes of equal chromatic order, FEKO) as shown schematically in **Figure 3.1**.

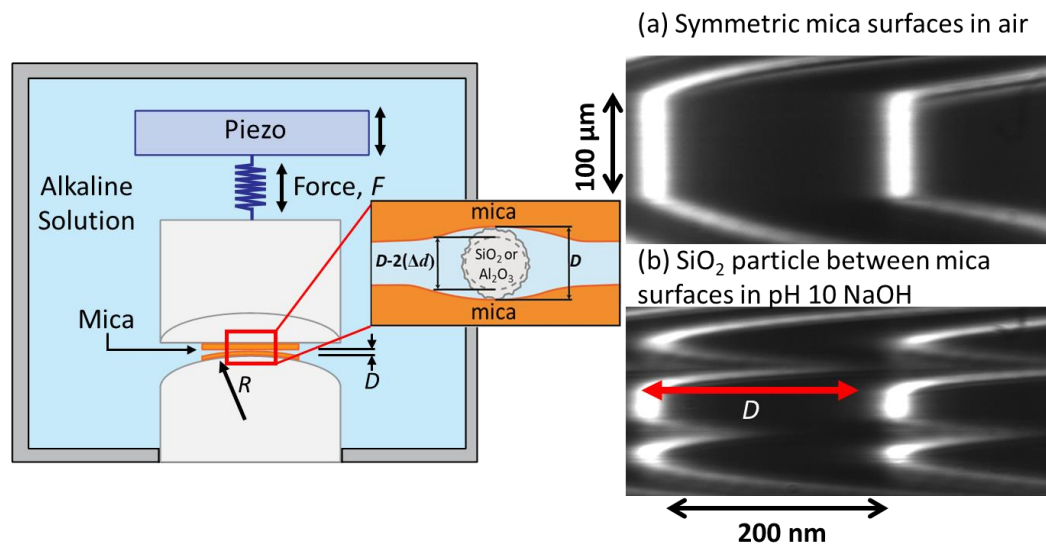


Figure 3.1 Schematic of SFA experimental setup used to measure the dissolution of alumina or silica nanoparticles trapped between mica surfaces in alkaline solution. The FECO images show the surface profile for (a) symmetric mica surfaces in air and (b) a silica (or alumina) particle confined between the same mica surfaces in pH 10 NaOH. The deformation in the FECO is caused by the height of the particle, D , which is tracked over the course of the experiment to measure the dissolution.

Surface deformation caused by the confined particles appear as distortions in the FECO. Dissolution of the compressed nanoparticle was calculated from the change in the distortion height over time and is shown in **Figure 3.3**. The remaining volume, approximately 200 mL, of the SFA is filled with the same alkaline solution, an approximately ‘infinite reservoir’ condition for the dissolution based on the solubility of alumina and silica.

3.1.3.2 Electrochemical pressure-cell dissolution measurements

Dissolution measurements of silica surfaces in contact with a gold electrode were performed using a custom-built electrochemical pressure-cell. The Teflon pressure-cell had a total volume of approximately 200 mL. The bottom surface was spring loaded where the applied force was measured with strain gauges. Two surfaces in a sphere-on-flat geometry were compressed to 2-3 atm in the pressure cell to ensure that the surfaces remain in close

proximity throughout the experiment. The spherical surface was a gold electrode (roughness = 2 nm RMS) prepared by template stripping from an atomically smooth mica surface and connected to a potentiostat via a gold wire.^{38,39} The bottom, flat surface was an approximately 500 nm thick SiO₂ film, (roughness = 1 nm RMS) on a Si wafer, with thickness measured by ellipsometry (Woollam Spectroscopic Ellipsometer). A schematic of the cell is shown in **Figure 3.2**. A potentiostat (Gamry, Model Reference 3000) was used to control the surface potential of the gold electrode. For each silica dissolution experiment, the pressure-cell was filled with aqueous solution, pH = 10, prepared using NaOH (Sigma-Aldrich, ≥ 98%). The silica was then allowed to dissolve for 24 hours at each applied potential. After dissolution at each potential, the thickness of the silica layer was measured again with ellipsometry. The average dissolution rate for each applied potential was calculated by dividing the change in silica thickness by the 24-hour time interval.

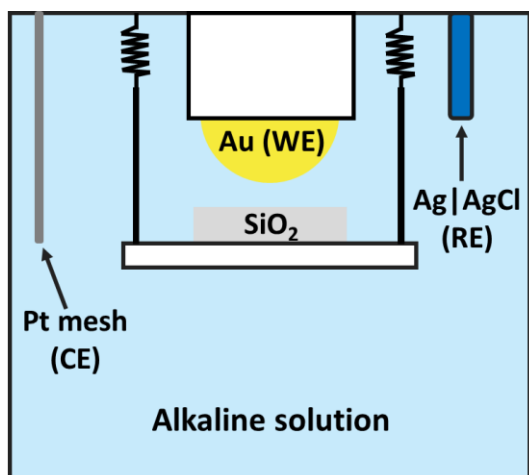


Figure 3.2 Schematic of the electrochemical pressure cell used to measure the dissolution rate of a flat silica surface at various applied surface potentials in a pH 10 NaOH solution. The silica surface is on a spring-loaded platform that can be compressed to maintain high pressure which ensures the surfaces stay in close proximity (< 3 nm) throughout the experiment. A potentiostat is used to apply a constant potential to the gold surface (working electrode) using a Ag|AgCl reference electrode and a platinum mesh counter electrode. Ellipsometry measurements of the silica thickness before and after the dissolution were used to determine the average dissolution rate over a 24-hour time period.

3.1.4 Results and Discussion

3.1.4.1 Enhanced dissolution of alumina and silica

The dissolution rate of silica and alumina particles in aqueous alkaline solution conditions is increased by proximity to a muscovite mica surface, forming asymmetric solid-liquid-solid interfaces with solid-solid separation distances of 1 to 10 nanometers. For these particle dissolution experiments, silica or alumina nanoparticles (20-300 nm in diameter) in aqueous solutions are compressed between two extended mica surfaces using a Surface Forces Apparatus (SFA).²⁶ A schematic of the SFA experimental setup and pictures of the interference fringes taken before and after the nanoparticles are compressed are shown in SI **Fig. 3.3**. The nanoparticles were compressed to 2-3 atm between the mica surfaces in pH 10 and 11 alkaline solutions and the particle diameter was measured as a function of time (**Fig. 3.3**, schematic inset). The initial time, $t = 0$, is designated as after the compression of the nanoparticle and adjustment of the optics in the SFA, which results in an average delay of 2 ± 1 minutes during which particles are exposed to the alkaline solution in contact with mica, but particle diameter is not measured. Additional details of the experiment setup are provided in the Materials and Methods section. **Figure 3.3** shows the changes in the particle height, Δd , as a function of time for confined silica and alumina nanoparticles in different solution conditions (circular points) are compared to the single-surface dissolution for similar alumina and silica materials under the excess solution conditions (dashed lines). The initial dissolution rate of each nanoparticle is large, shown by the steep slope at early times in the inset of **Fig. 3.3**, but decreases exponentially with time.

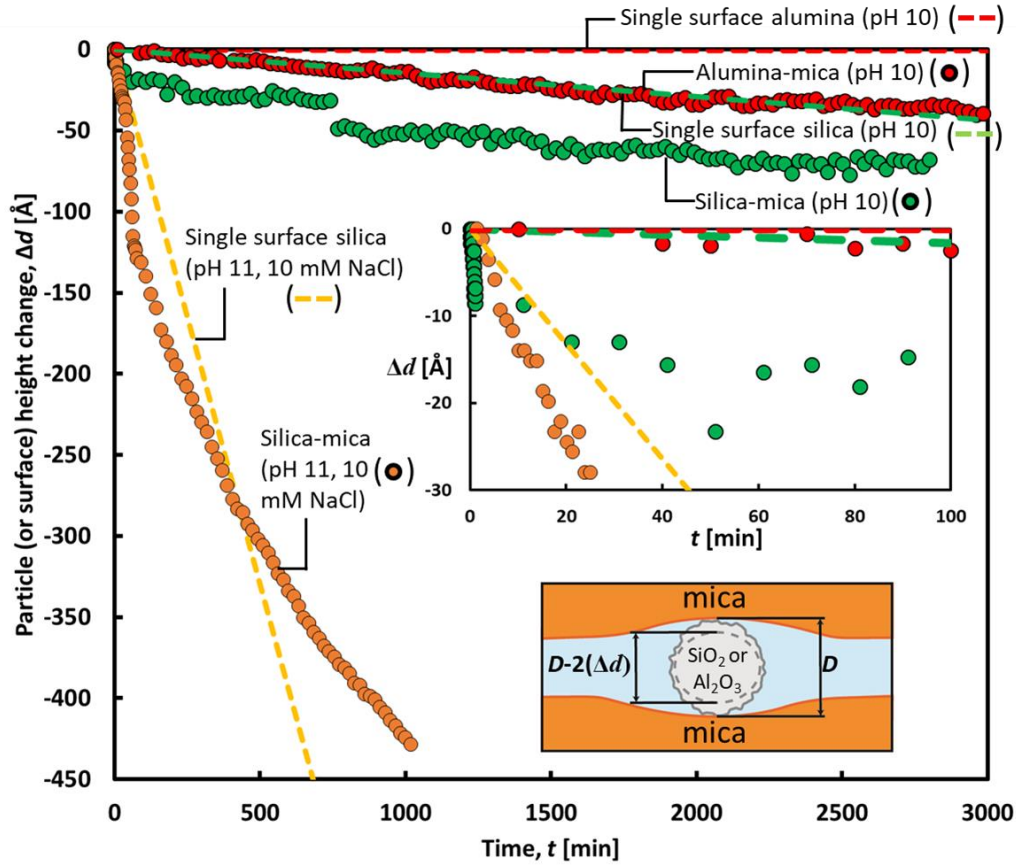


Figure 3.3 Measured change in particle height, Δd , as a function of time for spherical amorphous silica (green and orange) and polycrystalline alumina (red) particles trapped between mica surfaces in alkaline solutions of 0.1 mM NaOH (pH 10, red and green) and 1.0 mM NaOH (pH 11) with 10 mM NaCl (orange) are shown as individual data points. The error of each data point is ± 3 Å. The dashed lines represent linear extrapolations of the measured single-surface dissolution rate as labelled reference from the literature as indicated in the text.^{18,27,28} The decrease in the particle heights over time indicates dissolution of the particle between the surfaces, which is enhanced relative to the dissolution of the extended surfaces.

The dissolution of each nanoparticle, i.e. the change in height of the trapped nanoparticles, can be empirically fit with an exponential equation as the dissolution rate decreases over the reported experiment time. For the dissolution of the polycrystalline alumina nanoparticle, the dissolution can be fit to:

$$\Delta d = D_0 e^{-t/\tau_0} \text{ \AA} \quad (3.1)$$

where D_0 is the initial particle diameter, t is time, and τ_0 is the time constant where the particle height has decreased to D_0/e .

The dissolution of alumina and silica nanoparticles near mica surfaces exhibit exponentially decaying dissolution over the long experiment times. For the dissolution of alumina nanoparticles between mica surfaces at pH 10, shown in **Figure 3.3** as the red points, D_0 is $58 \pm 3 \text{ \AA}$ and τ_0 is 2600 ± 100 minutes. For the dissolution of silica nanoparticles between mica surfaces at pH 10, shown in **Figure 3.3** as the green points, D_0 is $71 \pm 3 \text{ \AA}$ and τ_0 is 990 ± 20 minutes; however, the behavior does not perfectly fit an exponential decay due to the observed ‘stepping’ behavior where periods of active dissolution and periods where the dissolution rate is strongly inhibited are observed. It has been hypothesized in the literature that the periods where dissolution is significantly slowed is due to the formation of pits at the surface which leads to local saturation of the silicate ions. Eventually, the pits collapse and allow the saturated solution to diffuse out of the pits located within the confined interface and into the bulk solution which is undersaturated with regards to the silicate ions.²² During dissolution, the presence of nanometer scale surface structure inhomogeneity significantly influences the formation and geometry of pits through the preferential dissolution at point defects as described by Dove et al.⁴⁰

For the dissolution of silica nanoparticles between mica surfaces at pH 11 and 10 mM NaCl, shown in **Figure 3.3** as the orange points, D_0 is $476 \pm 3 \text{ \AA}$ and τ_0 is 797 ± 3 minutes analyzing from after 70 minutes. The initial time behavior, for $t < 70$ minutes, exhibits strong variation in the observed dissolution rates which may also be due to the ‘stepping’ behavior observed for the dissolution of silica nanoparticles between mica surfaces at pH 10.

The decrease in the dissolution rate over time may be due to local saturation of the dissolved species in addition to the limited transport of the dissolved species from the confined gap, however studies to verify this are beyond the scope of this paper and will be explored in future work.

The average dissolution rate, calculated by dividing the total height change, Δd , by the total time of the experiment, can be used to determine the degree of dissolution enhancement, ϵ , compared to the single-surface bulk dissolution rate, where adequate (and still) volumes were used such that saturation does not occur.

$$\epsilon = \frac{\text{electrochemically asymmetric surface dissolution rate}}{\text{single surface solution dissolution rate}} \quad (3.2)$$

The degree of enhancement provides a means for quantifying and comparing the influence of asymmetric interfaces on dissolution enhancement for different materials, such as silica and alumina, which have different base dissolution rates under given solution conditions. For example, the dissolution rate of single-surface polycrystalline alumina in pH 10 bulk solution is approximately $-(2.5 \pm 0.1) \times 10^{-6} \frac{\text{\AA}}{\text{s}}$, as previously reported for a similar material in a pH 10 NaOH solution in the literature.²⁷ For comparison, the average dissolution rate of the polycrystalline alumina particle confined between two mica surfaces (**Fig. 3.3**, red points) was measured to be $-(1.1 \pm 0.1) \times 10^{-4} \frac{\text{\AA}}{\text{s}}$, which is 44 times larger than the dissolution of isolated polycrystalline alumina surfaces in pH 10 bulk solution (**Fig. 3.3**, dashed red line), an enhancement factor of $\epsilon = 44$. Therefore, the dissolution rate of polycrystalline alumina increased by over one order-of-magnitude when confined between mica surfaces compared to a single-surface exposed to bulk solution.

The reported dissolution rate²⁸ for amorphous silica in pH = 10 solution is $-(2.7 \pm 0.1) \times 10^{-4} \frac{\text{\AA}}{\text{s}}$ (Fig. 1, dashed green line) and the measured average initial dissolution rate for an amorphous silica nanoparticle confined between mica surfaces is $-(1.0 \pm 0.1) \times 10^{-3} \frac{\text{\AA}}{\text{s}}$ (**Fig. 3.3**, green points), which gives an enhancement factor of $\epsilon = 4$. For both alumina and silica, enhanced dissolution occurs upon introduction of a surface (mica) that has a more negative surface potential than the dissolving surface. While the degree of enhancement is an order of magnitude lower compared to the alumina-mica case discussed above, the dissolution of amorphous silica is still enhanced through the introduction of an electrochemically distinct surface (*i.e.*, mica). To understand the importance of surface electrochemical properties, the degree of enhancement can be compared with respect to the electrochemical surface potentials for silica, alumina, and mica.

Although the initial dissolution rate of particles in close proximity to a mica surface is higher than the dissolution rate of isolated surfaces of the same material, at longer times the single isolated surface dissolution rate is larger. We attribute this to diffusion (or transport) limitations and local saturation of dissolved species near the confined particles. In the particle dissolution experiments, the particles are confined between two mica surfaces and dissolved species must diffuse through the gap containing the particle to the bulk solution, similar to results reported by Alcantar et al.²⁹ Transport from the gap will be limited due to the high pressure in the contact area and the small mica-mica separation (*ca.* 10 Å) around the trapped particle. This decreased transport will result in local saturation of the dissolved silicate species and reduction of the dissolution rate. Single-surface dissolution environments involve less transport limitations, so the dissolution rate at long times is expected to be higher for isolated surfaces than for surfaces confined at an asymmetric solid-liquid-solid interface.

Enhanced dissolution occurs at solid-liquid-solid interfaces where the two solid surfaces are electrochemically distinct (i.e., different surface materials or structures) but not in systems with similar electrochemical properties, as shown by Greene et al.²² At pH = 10, the surface potentials of alumina, silica, and mica are approximately -20 mV, -90 mV, and -110 mV, respectively.³⁰⁻³² The difference between the surface potentials of alumina and mica is larger than for silica and mica, which correlates to the significantly greater degree of enhanced dissolution observed for the alumina particle confined between mica surfaces. This suggests that one of the most important parameters for dissolution enhancement is the relative surface potentials of the two electrochemically distinct surfaces at a solid-liquid-solid interface. Pourbaix diagrams have been used in the study of corrosion processes to understand whether materials will dissolve under specific solution and electric potentials, which can provide an indicator for which material dissolves.⁵⁶

The impact of the ionic strength, and therefore the Debye length of the electrostatic double layer, on dissolution was also tested. An electrical charged surface (or surface with non-zero electric potential) in aqueous solution develops an electrostatic double layer, a region of counterions, to screen the surface charge. Some of the counterions are bound to the surface within the Stern or Helmholtz layer, while others form an atmosphere of ions in rapid thermal motion close to the surface known as the diffuse electric double layer, which distribution follows the Poisson-Boltzmann equation.³³ At low surface potentials (<25 mV), the Debye length is the characteristic length of this diffuse layer region of the electrostatic double layer and depends only on the properties of the bulk solution. The Debye length, κ^{-1} , is given by the following equation simplified from the Grahame equation for a monovalent electrolyte at 25°C:³³

$$\kappa^{-1} = \left(\frac{\epsilon_0 \epsilon k T}{2 \rho_\infty e^2} \right)^{1/2} = \frac{0.304 \times 10^{-9}}{\sqrt{M}} m \quad (3.3)$$

where ϵ_0 is the permittivity of free space, ϵ is the bulk dielectric permittivity of the aqueous solution, k is the Boltzmann constant, T is the temperature, ρ_∞ is the concentration of ions in the bulk, e is the elementary charge of an electron, and M is the molar concentration of the monovalent ion in the aqueous solution.

To test the impact of a significant change in the Debye length, **Figure 3.3** also shows particle dissolution data for the same type of silica particles confined between mica surfaces, but in a pH = 11 (1 mM NaOH) solution with 10 mM NaCl. This is a change in Debye length from 30.4 nm in the pH = 10 solution to 2.9 nm in the pH = 11 solution with 10 mM NaCl. The reported dissolution rate¹⁸ for amorphous silica in pH = 11 solution with 10 mM NaCl is $-(1.1 \pm 0.1) \times 10^{-2} \frac{\text{\AA}}{\text{s}}$ and the measured initial dissolution rate, at $t < 100$ minutes, for amorphous silica particles between mica surfaces is $-(2.5 \pm 0.1) \times 10^{-2} \frac{\text{\AA}}{\text{s}}$, which gives a degree of enhancement of $\epsilon = 2.5$. The enhancement factor appears to be reduced with the shorter decay length; however, the surface potentials also change with the solution properties. The change in decay length significantly influences the degree to which the diffuse layer portions of the electrostatic double layer overlap. A larger decay length will have more overlap compared to a shorter decay length for the constant 3 nm separation. The more the diffuse layer portions overlap, the stronger the influence on the local electrostatic potential change. The surface potentials of mica and silica are approximately -70 mV and -50 mV, respectively, in a pH = 11 solution with 10 mM NaCl.³⁴ In addition, silica dissolves at a faster rate in pH 11, 10 mM NaCl solutions, which provides a significantly faster baseline as the enhancement is on the isolated surface natural dissolution rate. As the dissolution rate increases, further

enhancement of the dissolution rate will become more difficult. At this point, we cannot determine if the absolute magnitude of the surface potentials also has an impact on the enhancement factor compared to the difference between the two surfaces potentials. The data suggest that solution conditions with longer Debye lengths have greater enhancement factors, however, further experiments are required to thoroughly test this concept.

3.1.4.2 Electrochemically manipulated dissolution of silica

We hypothesize that dissolution is enhanced due to electrochemical effects arising from differences in the electrostatic surface potentials of different surfaces in nanoscale proximities. To test this hypothesis, an electrochemical pressure cell (see **Figure 3.2**) was used to measure the dissolution rate of an extended silica surface in contact with a gold electrode at different, controlled potentials and constant solution conditions (pH = 10), as shown in **Figure 3.2**. The height of the silica was measured using ellipsometry before and after a 24-hour dissolution period. **Figure 3.4** shows the average dissolution rates for different applied negative potentials on the gold surface.

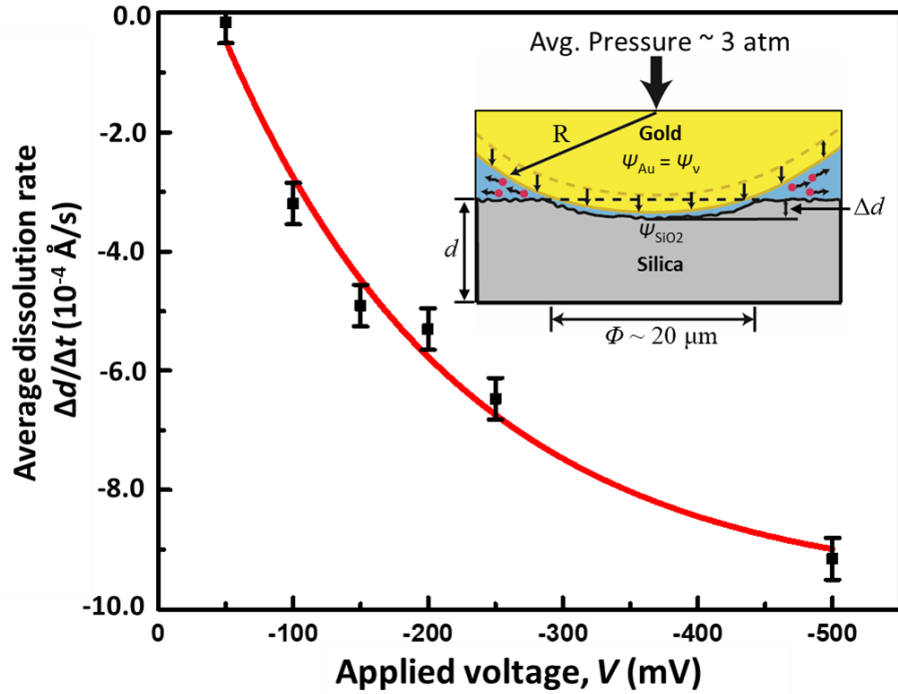


Figure 3.4 Dissolution of silica measured using an electrochemical pressure cell with a gold electrode with controllable surface potential is in contact with a silica surface in 0.1 mM NaOH (pH 10) solution. A potentiostat was used to maintain constant potential at the gold electrode. Each data point represents a single, 24-hour dissolution period at a given constant potential with the surface thickness measured before and after dissolution using ellipsometry. The dissolution rate is calculated as the total decrease in surface height averaged over the entire period. The bars on each data point indicate the error in the calculated dissolution rate and the red line indicates an exponential fit to the data with the equation provided in the text. The schematic inset shows the inelastic contact of the gold electrode with the silica surface under an average pressure of 3 atm. As the surface dissolves, the electrode continues to push down to maintain contact/close proximity (<5 nm) with the silica surface. The red dots indicate silicate ions diffusing away from the dissolution pit.

The silica dissolution rate increases with increasingly negative applied potentials, V , at the gold electrode, and was described by the following empirical equation:

$$\frac{\Delta d}{\Delta t} = C e^{\frac{V}{V_0}} + B_0 \quad (3.4)$$

$$\frac{\Delta d}{\Delta t} = (-12 \pm 1) \times 10^{-4} e^{\frac{V}{180 \text{ mV}}} + (10 \pm 1) \times 10^{-4} \text{ \AA/s} \quad (3.5)$$

where V_0 is the exponential potential constant, C is the pre-exponential constant, and B_0 is the intercept used to recreate the observed dissolution rate behavior. The empirical model is used

to fit the data as the measured dissolution rates are a combination of the reaction kinetics, transport principals, and electrochemical response of the system, where the relevant physical parameters have been absorbed into C and B_0 . The dissolution rate of the silica surface increased by an order of magnitude over the range of negative potentials applied at the gold electrode (-50 to -500 mV).

The dissolution rate decays exponentially with the applied potential, which indicates that at large negative applied potentials, the dissolution rate approaches an upper limit. The dissolution rate may be limited by local saturation of solution-phase silicate ions due to transport limitations of dissolved species in the confined solid-liquid-solid interface. Ion diffusion may be additionally complicated by the formation of pits or surface roughening and local saturation effects.²² Additionally, increased adsorption of surface counterions (e.g., Na^+) can inhibit the transport of surface ionic species along the electrostatic double layer, especially at the outer Helmholtz plane.³⁵ If the counterion concentration at the surface is too high, the probability of hydroxyl ions existing near the surface will lower and the ability of silicate ions to transport away from the surface will be inhibited. This can occur despite the catalytic effect that cations have on the silica dissolution reaction¹⁶ and can decrease the frequency of dissolution reactions occurring. Understanding the role of ion adsorption and transport on enhanced dissolution requires a model capable of accounting for transport principals, reaction kinetics, and electrostatics of the confined, asymmetric solid-liquid-solid interface.

3.1.4.3 Electrochemically enhanced dissolution model

Our experimental results indicate that enhanced dissolution of confined solid-liquid-solid interfaces in aqueous conditions depends on the electric field at the interface, which arises from the overlap of the electrostatic double layers of the two surfaces and therefore depends

on the relative surface potentials, the Debye length, and the surface separation distance. We propose the following physiochemical driving force for the observed dissolution enhancement. A charged surface in an electrolyte solution causes the ions in solution to arrange in an electrostatic double layer satisfying the Poisson-Boltzmann (PB) equation.³³ Within this double layer, the electrostatic potential decays exponentially from its maximum at the surface to zero within the bulk solution. The electric field is the gradient of the electrostatic potential $\psi(x)$ using the equation $E = -\frac{d\psi}{dx}$, where x is the coordinate normal to the surface.³³ When two charged surfaces are brought together close enough that their electric double layers overlap, the ion distribution, and hence the electrostatic potential and the electric field near the surfaces, rearrange to preserve the distribution following the PB equation. For two surfaces with different electrostatic surface potentials, the potential distribution that develops as the double layer structures overlap can result in a reversal of the direction of the electric field at one of the surfaces. This is illustrated in **Figure 3.5** with a plot of the electrostatic potential profile between electrochemically symmetric and asymmetric surfaces given by the Hogg-Healy-Fuerstenau equation:

$$\psi = \psi_{0_1} \cosh(\kappa x) + \left(\frac{\psi_{0_2} - \psi_{0_1} \cosh(2\kappa D)}{\sinh(2\kappa D)} \right) \sinh(\kappa x) \quad (3.6)$$

where ψ_{0_1} is the surface potential of the first surface, ψ_{0_2} is the surface potential of the apposing surface, κ is the inverse Debye length, D is the separation distance of the two surfaces, and x is the position between the surfaces.³⁶

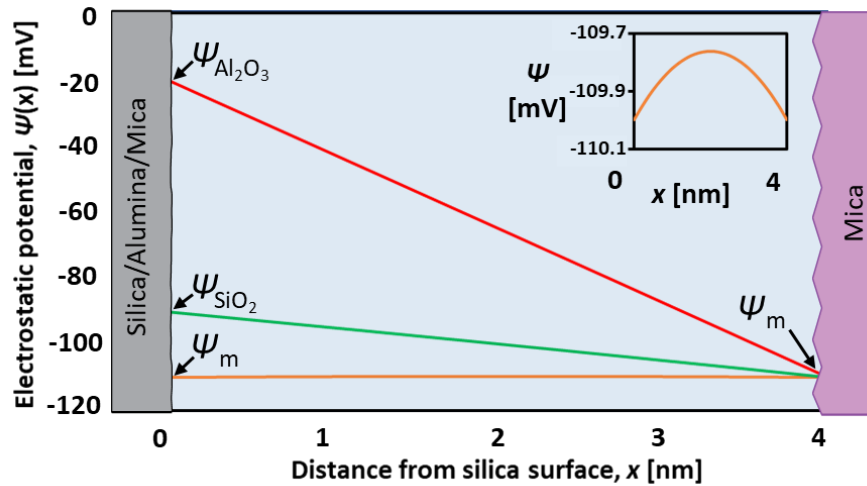


Figure 3.5 Electrostatic potential profiles calculated for an electrochemically asymmetric solid-liquid-solid interface separated by 4 nm in a 0.1 mM NaOH (pH 10) solution. The electrostatic profile is shown for an alumina, silica, or mica surface, with surface potentials of -20, -90, and -110 mV respectively, in close proximity to a second mica surface. The $\Psi(x)$ curves were plotted using the Hogg-Healy-Fuerstenau asymmetric double layer equation (Eq. 3.6). The inset shows an enlarged view of the electrostatic potential profile between the two identical mica surfaces.

The electrostatic potential profile changes significantly as a function of separation distance, D , as shown in the **Figure 3.6**. At large separations, when $D \gg \kappa^{-1}$, the potential gradient appears similar to a symmetric system such as two mica surfaces, where a maximum occurs between the two surfaces as seen in the inset of **Figure 3.5**, providing no driving force for ions to be released from the surface as the direction of the electric field at the surface remains unchanged.

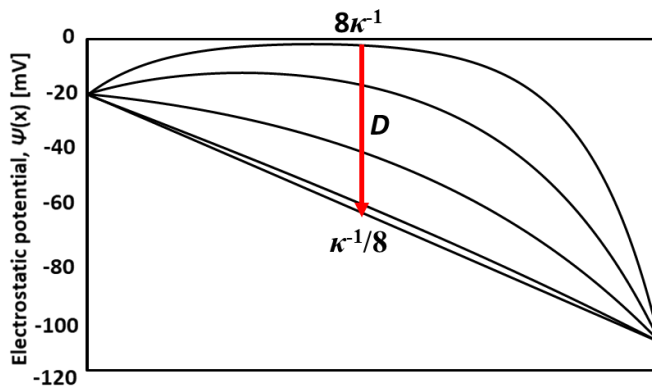


Figure 3.6 Electrostatic potential profiles for an asymmetric solid-liquid-solid interface of alumina (-20 mV) and mica (-110 mV) in a pH = 10 solution calculated using the Hogg-Healy-Fuerstenau equation for a range of separation distances, D , from $8\kappa^{-1}$ to $\kappa^{-1}/8$. At large separations, the electrostatic potential exhibits a maximum potential ‘hill’ which acts as an energy barrier to ion transport between the surfaces. As the separation distance decreases, the potential profile collapses to an almost linear potential gradient between the alumina and mica surfaces.

For surfaces with different negative potentials, the electric field at the less negatively charged surface can reverse direction. While the silica and alumina dissolution processes are not fully understood, the reactants, intermediate products, and products involve charged species.^{15,18} We propose that the reversed electric field at the alumina or silica surface in close proximity to mica drives ion release at one or more steps in the dissolution reaction, increasing the dissolution rate. An analogous situation is the application of tensile force to a bond that lowers the bond lifetime, a phenomenon described by the Bell theory.³⁷

Our proposed dissolution enhancement process is depicted schematically in **Figure 3.7** for silica and mica surfaces. When the mica and silica surfaces are separated by a large distance $D \gg \kappa^{-1}$ ($t < 0$, **Fig. 3.7a**), the electrostatic double layers of each surface do not overlap. At $t = 0$, the surfaces are brought into nanoscale proximity of each other ($D < \kappa^{-1}$), their electrochemically asymmetric diffuse layers overlap, and the reversal of electric field at the less negatively charged surface results in enhanced dissolution (**Fig. 3.7b**).

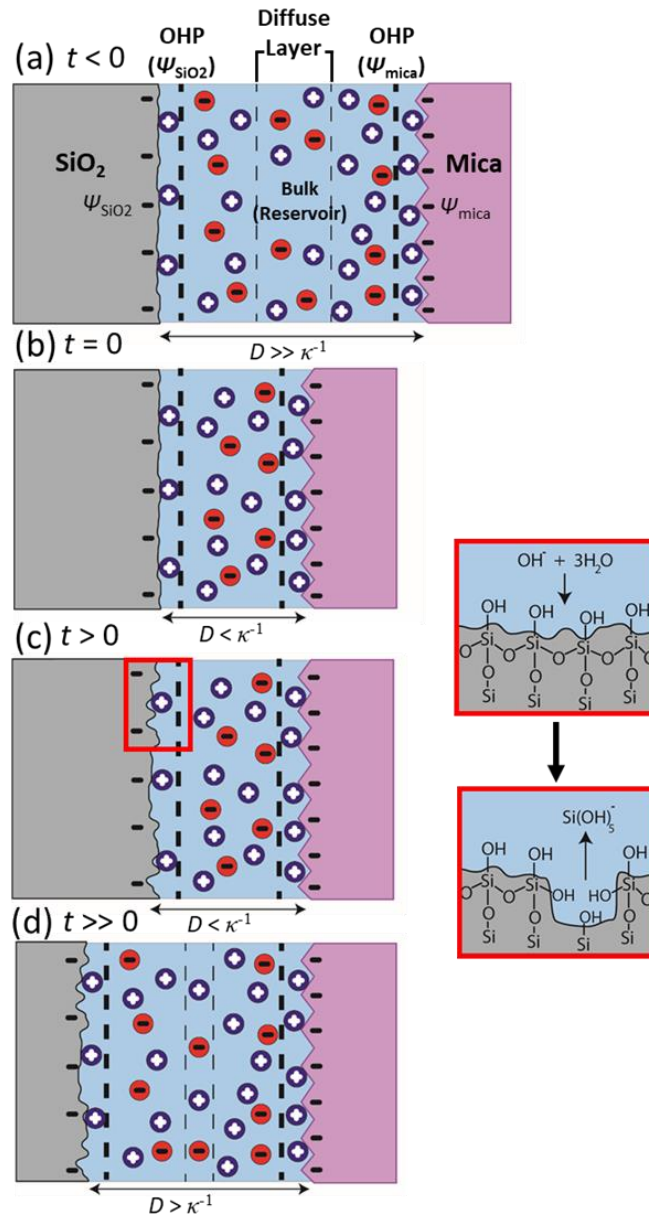


Figure 3.7 Schematic representation of the proposed model of electrochemically enhanced dissolution. **(a)** When surfaces are separated by relatively large distances, $D \gg \kappa^{-1}$, each surface can develop a complete electrostatic double layer (EDL) structure largely screens the surface potential, Ψ , of each surface over a characteristic length known as a Debye length, κ^{-1} . **(b)** Immediately (at $t = 0$) when the surfaces are brought close together, $D < \kappa^{-1}$, the diffuse electrostatic double layers of each surface overlap across the asymmetric solid-liquid-solid interface resulting in a steep potential gradient between the surfaces which reverses the electric field at the lower negative potential surface. **(c)** For $t > 0$, the potential gradient enhances the dissolution of the surface with a lower electrostatic potential. In this case, silica dissolves by successive hydrolysis reactions as shown schematically in the inset, while the mica surface shows no signs of dissolution/etching. **(d)** As time progresses, $t \gg 0$, the surface with the lower

electrostatic potential will undergo enhanced dissolution until the complete EDL structure is re-established as shown in **Figure 3.6**.

The reaction inset in **Figure 3.7** shows dissolution of silica in an alkaline environment following a mechanism proposed by Iler.¹³ For $t > 0$, dissolution leads to material removal and surface roughening (**Fig. 3.7c**). As the surfaces dissolve, the distance between them increases and the double layers overlap less, reducing the enhancement of dissolution. After very long times, $t \gg 0$, the separation distance increases to the extent that each surface has a complete, uninhibited electrostatic double layer ($D \gg \kappa^{-1}$, **Fig. 3.7d**). At this point, the dissolution rate is no longer enhanced and returns to the dissolution rate of a single-surface in bulk solution. From our results, it is apparent that the overlapping electrostatic double layers and the corresponding reverse in the electric field at the surface plays an important role in the enhanced dissolution of alumina and silica.

3.1.5 Discussion and Conclusions

The enhanced dissolution of silica and alumina in weakly alkaline environments that we report is in consistent with previous studies on pressure solution under acidic, geologic conditions. Our work clearly demonstrates the influence of the difference in surface potential between two surfaces on the extent of dissolution enhancement observed. By manipulating the applied electrostatic surface potential of a gold electrode, we increased the dissolution rate of silica by an order of magnitude. Furthermore, higher ionic strength (i.e., shorter Debye length) leads to a reduced degree of overlap of the electrostatic double layer, and results in lower enhancement of dissolution rates. Shorter Debye lengths resulted in a lower degree of enhancement due to less overlap of the diffuse layer regime, however further experiments are required to fully characterize the influence of the Debye length. These two examples

exemplify the dependence of enhanced dissolution on the electrochemical nature of surfaces in asymmetric solid-liquid-solid environments.

In our measurements of the dissolution of confined alumina and silica systems, electrochemical dissolution enhancement was observed in the initial time periods of each experiment, with slower dissolution at longer times. Each experiment was performed in a confined system without active transport, leading to local ion saturation due to the limited diffusion-only transport which reduced the dissolution rates. A similar saturation in dissolution rate enhancement was observed when using an electrochemically applied potential to manipulate dissolution in the silica-gold confined system. These results indicate that while electrochemically enhanced dissolution is important to increasing dissolution rates, the subsequent transport of ions away from the surface is equally important to avoid local saturation and thus limiting the observed dissolution rates. Future work will study the impact of active (i.e., convective) transport on dissolution rates, toward a model for dissolution which encompasses reaction kinetics, transport mechanics, and electrostatic theory.

We propose that our model for electrochemically enhanced dissolution at confined, asymmetric solid-liquid-solid interfaces explains the enhanced dissolution seen in CMP and geologic pressure solution. More broadly, our model seeks to explain the driving force behind the restructuring/degradation observed in confined, aqueous environments that are relevant to crevice corrosion (ref Ni crevice corrosion with Markus), crystallization of catalysts, bioadhesives, and structural materials. The insights provided here on the relationship between surface electrochemical properties and dissolution processes are expected to inform new methods for improved control of dissolution and restructuring processes.

3.2 Electrochemically controlled dissolution of inorganic materials

Reactivity in confinement is central to a wide range of applications and systems, such as geological and technological processes, for example, pressure solution,^{41,42} chemical mechanical polishing (CMP),⁴³ electropolishing,⁴⁴ and corrosion,^{45,46} including biocorrosion, for example, implants and dental fillings.^{47,48} In some cases, increased dissolution rates are desired, such as CMP; however, in other systems, particularly involving pitting and crevice corrosion, increased reactivity leads to material degradation and damage. In each of these systems, the confinement (close apposition) of two asymmetric surfaces in an aqueous environment is a common factor where increased reactivity is observed. However, unlike systems exposed to bulk solutions, the difficulties introduced by reactivity and transport (e.g., diffusion) in confinement lead to complications in developing an understanding of reaction processes under these conditions. Further application of the reported electrochemically enhanced dissolution model for confined, asymmetric solid-liquid-solid interfaces provides an opportunity to better understand and control technologically important dissolution processes.

3.2.1 Electrochemically enhanced dissolution of diamond

CMP-related processes have been primarily founded on empirical testing and characterization of different slurry and substrate combinations to achieve different dissolution rates and surface roughness.⁴⁹⁻⁵¹ Understanding of fundamental processes which are involved in CMP have been thoroughly investigated, however the fundamental questions regarding the driving forces behind the change in dissolution rates with solution and slurry composition remain.^{3,52,53} Due to the diverse range of materials relevant to important technological processes, there is no shortage of experiments to empirically characterize the necessary CMP

processes. Determining a widely applicable method to influence enhanced dissolution regardless of the materials involved is key to further developing CMP technologies.

The influence of electrostatic forces on the dissolution rate of alumina and silica was previously demonstrated, however the proposed electrochemically enhanced dissolution model is a general model that only requires two asymmetric surfaces which develop distinct surface potentials in the solid-liquid-solid interface. In this case, if we can satisfy the confined, asymmetric solid-liquid-solid interface such that overlap of the electrostatic double layers is achieved, enhanced dissolution of other materials should be observed. The electrochemical pressure cell (see **Figure 3.2**) was used with ellipsometry to study the enhance dissolution of single crystal diamond surfaces as shown in **Figure 3.8**.

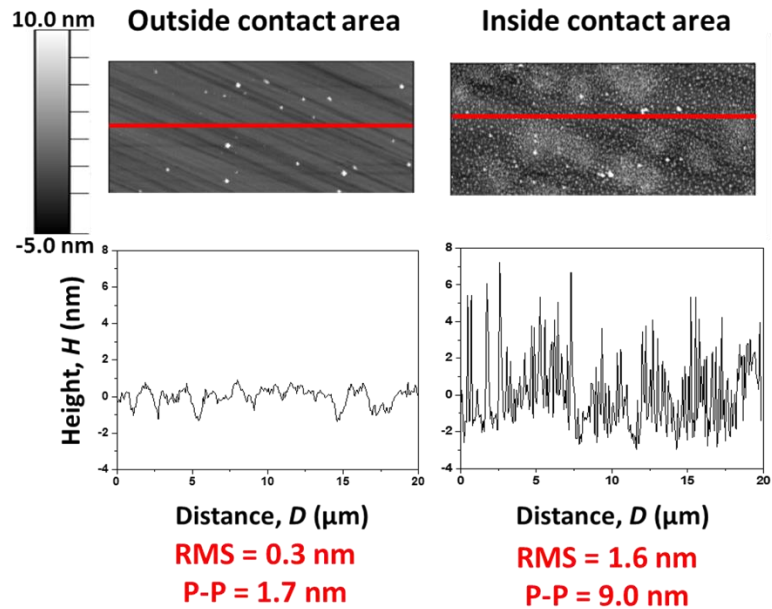


Figure 3.8 Electrochemically enhanced dissolution of polished, single crystal diamond surfaces using the electrochemical pressure cell setup. The diamond was placed in contact with a gold electrode at -210 mV in 5 mM KCl at pH 7, 295 K, and under 1 atm of pressure for 24 hours. The surface potential of diamond in a 5 mM KCl, pH 7 solution is around -50 mV.⁵⁴ The surface roughness before and after dissolution was verified using atomic force microscopy (AFM).

Within the contact area of the gold electrode, the diamond surface roughness increased by a factor of 5, from 0.3 nm RMS to 1.6 nm RMS. Similarly, the increase in the maximum peak-to-peak distance also increased by a factor of 5. Outside of the contact area of the gold electrode, the surface roughness and peak-to-peak distance remain the exact same as the original diamond surface. When the asymmetric, confined solid-liquid-solid interface condition is achieved, enhanced dissolution of diamond is achieved even though there is no known dissolution pathway for diamond at room temperature in aqueous environments. Previously, diamond surfaces were reported to dissolve in high pressure and high temperature melts, greater than 3 GPa and 1400°C.⁵⁵

The observed dissolution of diamond through application of electrostatic force further reinforces our electrochemically enhanced dissolution model for confined, asymmetric solid-liquid-solid interfaces as a general model to understand enhanced dissolution processes in naturally occurring and technologically important processes. Development of the electrochemically enhanced dissolution model may inform new methods for improved control and manipulation of dissolution phenomena at confined interfaces.

References

1. Bjornstrom J, Martinelli A, Matic A, Borjesson L, Panas I (2004) Accelerating effects of colloidal nano-silica for beneficial calcium-silica-hydrate formation in cement. *Chem. Phys. Lett.* 392:242-248
2. Brand AS, Bullard JW (2017) Dissolution Kinetics of Cubic Tricalcium Aluminate Measured by Digital Holographic Microscopy. *Langmuir* 33:9645-9656
3. Krishnan M, Nalaskowski JW, Cook LM (2010) Chemical Mechanical Planarization: Slurry Chemistry, Materials, and Mechanisms. *Chem. Rev.* 110:178-204

4. Yan W, Zhang Z, Guo X, Liu W, Song Z (2015) The Effect of pH on Sapphire Chemical Mechanical Polishing. *ECS J. Solid State Sci. Technol.* 4(3):108-111
5. Zhai D, Zhao L, Liu Y, Xu J, Shen B, Gao, J (2015) Dissolution and Absorption: A Molecular Mechanism of Mesopore Formation in Alkaline Treatment of Zeolite. *Chem. Mater.* 27(1):67-74
6. Anzalone A, Boles J, Greene G, Young K, Israelachvili J, Alcantar A (2006) Confined fluids and their role in pressure solution. *Chemical Geology* 230:220-231
7. Nair RR, Gupta A, Victoria SN, Manivannan R (2017) Chemical mechanical planarization of germanium using oxone based silica slurries. *Wear* 376-377:86-90
8. Zhou Y, Pan G, Shi X, Zhang S, Gong H, Luo G (2015) Effects of ultra-smooth surface atomic step morphology on chemical mechanical polishing (CMP) performances of sapphire and SiC wafers. *Tribology International* 87:145-150
9. Duxson P, Fernandez-Jimenez A, Provis JL, Lukey GC, Palomo A, van Deventer JSJ (2007) Geopolymer technology: the current state of the art. *J. Mater. Sci.* 42:2917-2933
10. Hajimohammadi A, Provis JL, van Deventer JSJ (2010) Effect of Alumina Release Rate on the Mechanism of Geopolymer Gel Formation. *Chem. Mater.* 22:5199-5208
11. Carrier X, Lambert JF, Che M (1997) Ligand-Promoted Alumina Dissolution in the Preparation of MoOX/ γ -Al₂O₃ Catalysts: Evidence for the Formation and Deposition of an Anderson-type Alumino Heteropolymolybdate. *J. Am. Chem. Soc.* 119:10137-10146

12. Piana S, Gale JD (2005) Understanding the Barriers to Crystal Growth: Dynamical Simulation of the Dissolution and Growth of Urea from Aqueous Solution. *J. Am. Chem. Soc.* 127(6):1975-1982
13. Iler R (1979) *The Chemistry of Silica: Solubility, Polymerization, Colloid and Surface Properties and Biochemistry of Silica* (John Wiley and Sons, New York, USA) pp.3-76, 356-385
14. Dove PM, Han N, Wallace AF, De Yoreo JJ (2008) Kinetics of amorphous silica dissolution and the paradox of the silica polymorphs. *Proc. Nat. Acad. Sci. USA* 105(29):9903-9908
15. Tombacz E, Szekeres M (2001) Interfacial Acid–Base Reactions of Aluminum Oxide Dispersed in Aqueous Electrolyte Solutions. 1. Potentiometric Study on the Effect of Impurity and Dissolution of Solid Phase. *Langmuir* 17(5):1411-1419
16. Dove PM, Nix CJ (1997) The influence of the alkaline earth cations, magnesium, calcium, and barium on the dissolution kinetics of quartz. *Geochim. Cosmochim. Acta* 61:3329-3340
17. Dove PM (1999) The dissolution kinetics of quartz in aqueous mixed cation solutions. *Geochim. Cosmochim. Acta* 63:3715-3727
18. Dove PM, Elston SF (1992) Dissolution kinetics of quartz in sodium chloride solutions: analysis of existing data and a rate model for 25°C. *Geochim. Cosmochim. Acta* 56:4147-4156
19. Green HW (1984) “Pressure Solution” Creep: Some Causes and Mechanisms. *J. Geophys. Res.: Solid Earth* 89:4313-4318

20. Kruzhanov V, Stockhert B (1998) On the Kinetics of Elementary Processes of Pressure Solution. *Pure appl. geophys.* 152:667-683
21. Israelachvili JN, Kristiansen K, Gebbie MA, Lee DW, Donaldson SH, Das S, Rapp MV, Banquy X, Valtiner M, Yu J (2013) The Intersection of Interfacial Forces and Electrochemical Reactions. *J. Phys. Chem. B* 117(51):16369-16387
22. Greene GW, Kristiansen K, Meyer EE, Boles JR, Israelachvili JN (2009) Role of electrochemical reactions in pressure solution. *Geochim. Cosmochim. Acta* 73:2862-2874
23. Kristiansen K, Valtiner M, Greene GW, Boles JR, Israelachvili JN (2011) Pressure solution – The importance of the electrochemical surface potentials. *Geochim. Cosmochim. Acta* 75:6882-6892
24. Lee H, Lee H, Jeong H, Choi S, Lee Y, Jeong M, Jeong H (2012) Macroscopic and Microscopic Investigation on Chemical Mechanical Polishing of Sapphire Wafer. *J. Nanosci. Nanotechnol.* 12:1256-1259
25. Steigerwald JM, Murarka SP, Gutmann RJ (1997) *Chemical Mechanical Planarization of Microelectronic Materials* (John Wiley and Sons, New York, USA)
26. Israelachvili J, Min Y, Alig A, Carver G, Greene W, Kristiansen K, Meyer E, Pesika N, Rosenberg K, Zeng H (2010) Recent advances in the surface forces apparatus (SFA) technique. *Rep. Prog. Phys.* 73:036601
27. Carroll-Webb SA, Walther JV (1988) A surface complex reaction model for the pH-dependence of corundum and kaolinite dissolution rates. *Geochim. Cosmochim. Acta* 52:2609-2623

28. Seidel A, Lobbus M, Vogelsberger W, Sonnefeld J (1997) The kinetics of dissolution of silica ‘Monospher’ into water at different concentrations of background electrolyte. *Solid State Ionics* 101-103:713-719
29. Anzalone A, Boles J, Greene G, Young K, Israelachvili J, Alcantar N (2006) Confined fluids and their role in pressure solution. *Chemical Geology* 230:220-231
30. de Lint WBS, Zivkovic T, Benes NE, Bouwmeester HJM, Blank DHA (2006) Electrolyte retention of supported bi-layered nanofiltration membranes. *Journal of Membrane Science* 277:18-27
31. Shin YJ, Su CC, Shen YH (2006) Dispersion of aqueous nano-sized alumina suspensions using cationic polyelectrolyte. *Materials Research Bulletin* 41:1964-1971
32. Morga M, Adamczyk Z, Godrich S, Ocwieja M, Papastavrou G (2015) Monolayers of poly-l-lysine on mica – Electrokinetic characteristics. *Journal of Colloid and Interface Science* 456:116-124
33. Israelachvili JN (2011) *Intermolecular and Surface Forces*, 3rd ed. (Elsevier, California, USA)
34. Nishimura S, Tateyama H, Tsunematsu K, Jinnai K (1992) Zeta Potential Measurement of Muscovite Mica Basal Plane-Aqueous Solution Interface by Means of Plane Interface Technique. *Journal of Colloid and Interface Science* 152:359-367
35. Anson FC (1975) Patterns of Ionic and Molecular Adsorption at Electrodes. *Acc. Chem. Res.* 8(12):400-407
36. Hogg R, Healy TW, Fuerstenau DW (1966) Mutual Coagulation of Colloidal Dispersions. *Trans. Faraday Soc.* 62:1638-1651

37. Bell GI (1978) Models for the Specific Adhesion of Cells to Cells. *Science* 200:618-627
38. Chai L, Klein J (2007) Large Area, Molecularly Smooth (0.2 nm rms) Gold Films for Surface Forces and Other Studies. *Langmuir* 23(14):7777-7783
39. Valtiner M, Kristiansen K, Greene GW, Israelachvili JN (2011) Effect of Surface Roughness and Electrostatic Surface Potentials on Forces Between Dissimilar Surfaces in Aqueous Solution. *Adv. Mater.* 23:2294-2299
40. Dove PM, Han N, De Yoreo JJ (2005) Mechanisms of classical crystal growth theory explain quartz and silicate dissolution behavior. *Proc. Nat. Acad. Sci. USA* 102(43):15357-15362
41. de Boer RB, Nagtegaal PJC, Duvys EM (1977) Pressure solution experiments on quartz sand. *Geochim. Cosmochim. Acta* 41:257.
42. Alcantar N, Israelachvili J, Boles J (2003) Forces and ionic transport between mica surfaces: Implications for pressure solution. *Geochim. Cosmochim. Acta* 67(7):1289-1304.
43. Mishra N, et al. (2014) Controlling the surface roughness of epitaxial SiC on silicon. *J. Applied Phys.* 115:203501.
44. Piotrowski O, Madore C, Landolt D (1998) The mechanism of electropolishing of titanium in methanol-sulfuric acid electrolytes. *J. Electrochem. Soc.* 145:2362.
45. Laycock NJ, Stewart J, Newman RC (1997) The initiation of crevice corrosion in stainless steels. *Corros. Sci.* 39(10-11):1791-1809.
46. Lott SE (1989) The Role of Inclusions on Initiation of Crevice Corrosion of Stainless Steel. *J. Electrochem. Soc.* 136(4):973.

47. Grippo J, Simring M, Coleman T (2012) Abrfraction, abrasion, biocorrosion, and the enigma of nancarious cervical lesions: a 20-year perspective. *J. Esthet. Restor. Dent* 24:10.
48. Lin H, Bumgardner JD (2004) In vitro biocorrosion of Co-Cr-Mo implant alloy by macrophage cells. *J. Orthop. Res* 22:1231.
49. P.B. Zantye, A. Kumar, and A.K. Sikder, "Chemical mechanical planarization for microelectronics applications," *Mater. Sci. Eng. R* 45, 89–220 (2004)
50. M.S. Miller, M.A. Ferrato, A. Niec, M.C. Biesinger, T.B. Carmichael (2014) Ultrasmooth Gold Surfaces Prepared by Chemical Mechanical Polishing for Applications in Nanoscience. *Langmuir* 30:14171-14178
51. Z. Zhang, B. Wang, P. Zhou, D. Guo, R. Kang, B. Zhang (2016) A novel approach of chemical mechanical polishing using environment-friendly slurry for mercury cadmium telluride semiconductors. *Scientific Reports* 6:22466
52. Matijevic, E.; Babu, S. V. (2008) Colloid aspects of chemical-mechanical planarization. *J. Colloid Interface Sci.* 320:219-237
53. K. Kawaguchi, H. Ito, T. Kuwahara, Y. Higuchi, N. Ozawa, M. Kubo (2016) Atomistic Mechanisms of Chemical Mechanical Polishing of a Cu Surface in Aquoues H₂O₂: Tight-Binding Quantum Chemical Molecular Dynamics Simulations. *ACS Appl. Mater. Interfaces* 8:11830-11841
54. A. Härtl, J.A. Garrido, S. Nowy, R. Zimmermann, C. Werner, D. Horinek, R. Netz, M. Stutzmann (2007) The Ion Sensitivity of Surface Conductive Single Crystalline Diamond. *J. Am. Chem. Soc.* 129:1287-1292

55. A.I. Chepurov, V.M. Sonin, E.I. Zhimulev, A.A. Chepurov, B.S. Pomazansky, A.L. Zemnukhov. (2018) Dissolution of diamond crystals in a heterogeneous (metal-sulfide-silicate) medium at 4 GPa and 1400°C. *Journal of Mineralogical and Petrological Sciences* 113:59-67
56. Roberge PR (2008) *Corrosion Engineering: Principles and Practice* (McGraw-Hill, USA)

Chapter 4: In Situ nano-to-microscopic imaging and growth mechanism of electrochemical dissolution (eg, corrosion) of a confined metal surface

Reproduced with permission from C. Merola, K. Schwenzfeier, K. Kristiansen, Y.-J. Chen, H. Dobbs, J.N. Israelachvili, M. Valtiner. *Proc. Nat. Acad. Sci.* 2017, 114(36), 9541-9546

4.1 Abstract

Reactivity in confinement is central to a wide range of applications and systems, yet it is notoriously difficult to probe reactions in confined spaces in real time. Using a modified electrochemical surface forces apparatus (EC-SFA) on confined metallic surfaces we observe *in-situ* nano-to-micro-scale dissolution and pit formation (qualitatively similar to previous observation on non-metallic surfaces; e.g., silica) in well-defined geometries in environments relevant to corrosion processes. We follow ‘crevice corrosion’ processes in real time in different pH-neutral NaCl solutions and applied surface potentials of nickel (vs Ag|AgCl electrode in solution) for the mica-nickel confined interface of total area $\sim 0.03 \text{ mm}^2$. The initial corrosion proceeds as self-catalyzed pitting, visualized by the sudden appearance of circular pits with uniform diameters of 6-7 μm and depth $\sim 2\text{-}3 \text{ nm}$. At concentrations above 10 mM NaCl, pitting is initiated at the outer rim of the confined zone, while below 10 mM NaCl, pitting is initiated inside the confined zone. We compare statistical analysis of growth kinetics and shape evolution of individual nanoscale deep pits with estimates from macroscopic experiments to study initial pit growth and propagation. Our data and experimental techniques reveal a mechanism that suggests initial corrosion results in formation of an aggressive interfacial electrolyte that rapidly accelerates pitting, similar to

crack initiation and propagation within the confined area. These results support a general mechanism for nanoscale material degradation and dissolution (e.g., crevice corrosion) of poly-crystalline non-noble metals, alloys, and inorganic materials within confined interfaces.

4.2 Introduction

Reactivity in confinement is central to a wide range of applications and systems, such as geological and technological processes, for example, pressure solution,^{1,2} chemical mechanical polishing (CMP),³ electropolishing,⁴ and corrosion,^{5,6} including biocorrosion, for example, implants and dental fillings.^{7,8} In some cases, increased dissolution rates are desired, such as CMP; however, in other systems, particularly involving pitting and crevice corrosion, increased reactivity leads to material degradation and damage. In each of these systems, the confinement (close apposition) of two asymmetric surfaces in an aqueous environment is a common factor where increased reactivity is observed. However, unlike systems exposed to bulk solutions, the difficulties introduced by reactivity and transport (e.g., diffusion) in confinement lead to complications in developing an understanding of reaction processes under these conditions. Furthermore, few techniques are able to directly measure and study reactivity in confinement *in-situ* at relevant length scales, leaving even more uncertainty surrounding the initiation and early growth of dissolution or corrosion processes in confinement. As a result, the understanding of early stage reactivity in confinement remains challenging and more detailed nanoscale characterization methods are required to develop a deeper understanding.

From an electrochemical viewpoint, crevice corrosion – the focus of this manuscript – and pitting corrosion are related phenomena,⁹⁻¹¹ although there are significant geometrical differences between them. Pitting corrosion is driven by an aggressive ionic environment and

oxygen depletion in the stagnant electrolyte of growing pits on a surface exposed to bulk solution.¹²⁻¹⁴ Crevice corrosion is a related form of *localized/confined* corrosion that may occur within cracks and crevices where depletion and reduced transport of species such as oxygen may lead to the development of aggressive media and local corrosion potentials.¹⁵ Within crevice corrosion, the initiation and growth of pits are observed and, throughout this paper, we will commonly refer to pits within the crevice (which is a separate phenomenon from pitting corrosion).

Crevice corrosion is of particular concern for stainless steels and nickel alloys in contact with chloride containing solutions, commonly found in marine environments.^{5,6} Chloride anions can be found in a wide range of environments such as seawater, industrial raw water and sludge. In particular, the potential gradient that develops in crevice corrosion drives cations out of the crevices and anions, such as chloride, into the crevices.¹⁴ The diffusion of ions into or out of crevices depends on their mobility. Chloride has a very high mobility and it is often present in high concentration in crevices. As such, chloride anions tend to accumulate inside the crevice while the more hydrated and larger cations (e.g. sodium), which typically are less mobile, remain mainly outside the crevice. In addition, the hydrolysis of the dissolving metal ions leads to a stark local variation of the pH.^{11,12,16} The dissolution products of the material (metallic cations) are also driven out of the crevice, which leads to a local change of the pH.

Ex-situ macroscopic studies of pitting corrosion, crevice corrosion and uniform corrosion of nickel alloys in different aqueous media and conditions were reported by various authors.¹⁷⁻¹⁹ However, real time and *in-situ* nanoscale investigations of localized corrosion (both pitting and crevice corrosion) remain a challenge. In particular, localized corrosion processes take

place at very small length scales and highly localized initiation sites that may be buried or hidden within the confined geometry of two closely apposed surfaces. A direct, *in-situ* view into the various crevice corrosion processes at progressing cracks is experimentally difficult. Recently, significant advances have been made using x-ray tomography;²⁰ however, resolution limits still inhibit characterization of the onset of corrosion. Typically, electrochemical pitting corrosion and crevice corrosion tests are carried out in a system-relevant environment and conditions, and the sample surfaces are examined *ex-situ* using a variety of different materials characterization and imaging techniques. Initial pit formation on an extended surface can also be studied *in-situ* by locally resolved probe techniques, such as spectroscopy or x-ray tomography, but, it is not straightforward to detect pitting corrosion since the initiation sites are sparsely distributed and typically hidden inside a confined area where two surfaces are separated by difficult to resolve (temporally and spatially) nanometer-sized gaps or crevices.

Previous observation using a modified electrochemical Surface Forces Apparatus (EC-SFA) on non-metallic surfaces (e.g., silica) of electrochemical reactions, dissolution, and *in-situ* observation of, for example, pit formation has been demonstrated as a valid method to study reactivity in confinement using Multiple Beam Interferometry (MBI).^{21,22} We further demonstrated Ångstrom-resolved real-time visualization of the initial corrosion behavior in a confined environment using white light interferometry to study corrosion of confined aluminum surfaces.²⁴ Here, we extend our studies to crevice corrosion of nickel. In addition to our previous method, a camera was added to visualize and quantify the crevice corrosion process with simultaneous optical microscopy and interferometry (MBI) in real time. We studied the effects of concentration and charging dynamics on the corrosion initiation by

changing the surface potential/charge ramping rate and following the initial dissolution and pit formation of confined nickel surfaces in chloride solutions. Based on our experimental results and methodology, we present a detailed mechanism for the initiation and initial growth of pits during nickel crevice corrosion, which may provide general insights into nanoscale pit formation and growth in other systems.

4.3 Experimental methods

4.3.1 Chemicals

All chemicals were purchased from Sigma-Aldrich at the highest purity available (sodium chloride, 99.9% pure). Sodium chloride (NaCl) solutions (1 mM; 10 mM; 100 mM) were prepared with Milli-Q (Millipore) water with a resistivity $\geq 18 \text{ M}\Omega\cdot\text{cm}$ and a TOC ≤ 2 ppb. Optical grade 1 ruby-mica was obtained from S&J Trading Company (NJ, U. S. A.) as sheets of about $20 \text{ cm} \times 20 \text{ cm}$ and 2 mm thickness. $5\text{--}10 \text{ cm}^2$ mica sheets with thicknesses ranging from $2\text{--}5 \text{ }\mu\text{m}$ were hand-cleaved from raw sheets and used for the experiments (23). Physical vapor deposition (PVD) back-silvered highly flexible mica sheets of $2\text{--}6 \text{ }\mu\text{m}$ thickness were then glued to cylindrical silica disks of nominal radius of curvature $R = 7 - 15 \text{ mm}$. Semitransparent Ni thin films with a thickness, $T_{\text{Ni}} = 30 \text{ nm}$, were prepared by PVD at deposition rates of $\leq 0.5 \text{ \AA/s}$. The microstructure of these films is dominated by grains that are below 20 nm, as estimated by electron microscopy imaging.

4.3.2 Surface Forces Apparatus (SFA)

SFA measurements were performed at 21°C in a cleanroom using the SFA 2000 (SurForce LLC, Santa Barbara, CA, USA). One cylindrical glass disk with an atomically smooth, back-silvered muscovite mica surface and an apposing glass disk with a 30 nm Ni layer were

mounted in the SFA in cross-cylinder geometry. This geometry creates a 2-layer interferometer with the Ni surface facing the solution side, while the back-silvered mica surface acts as the crevice former. Zero distance ($D = 0$) is defined as contact between mica and nickel in dry air (see schematic in **Figure 4.1b** where $\Delta t_E = 0$). Any changes of the separation distance between the Ag and the Ni “mirror” surfaces due to, e.g., ingress of water, or shift of the Ni-mirror surface due to corrosion (conversion into oxide or dissolution), can be tracked *in situ* by following both the distance shift of the mirror and the change of the light intensity (due to the thinning of the reflecting nickel layer). The setup is sensitive to approximately 25–50 picometer absolute shifts of mirror distances, relative to the zero distance, $D = 0$, defined under dry conditions. The electrochemical three-electrode attachment consists of a Ni working electrode and Pt counter and reference electrodes. All measurements were performed in NaCl solutions of different concentrations with a pH of 7–7.5. Every Pt pseudo reference was referenced against a standard 3N Ag|AgCl electrode,²⁴ showing a difference of about +400 mV with typical variations of 50–80 mV depending on the Pt wire used. All data is referenced to the open circuit potential, which is set to zero at -450 mV vs Ag|AgCl. Here, Pt pseudo references are used to limit concentration changes within the small volumes of NaCl electrolytes between the surfaces (e.g., in the crevice). Chloride based reference electrodes potentially leak chlorides and may substantially change the concentration in small volumes (as in our cell) and, in particular, in small concentrations (here e.g. 0.5 mM). As such, Pt wires are a balance between accuracy and chloride concentration stability.

4.3.3 Apparatus modifications

The electrochemical Surface Forces Apparatus (EC-SFA) has been adapted for characterization of corrosion processes in confinement as shown in **Figure 4.1**. In addition to

a standard EC-SFA setup,^{22,24} an optical camera connected to a 10x microscope was added to simultaneously record both (1) optical images of the corroding confined areas and (2) shifts of the corroding metal mirrors via wavelength shifts in the Fringes of Equal Chromatic Order (FECO).²⁵ A typical FECO image showing a flattened contact is depicted in **Figure 4.1(b)**. The two-dimensional FECO pattern or spectrum measured in the spectrometer simultaneously provides a spectroscopic axis to directly measure the distance between the two apposing mirrors with a resolution of 0.1 nm and a lateral axis for an optical image of a section through the contact region with a resolution of about 0.7 μm . For more details on the use of FECO, we refer the reader to a review article by Israelachvili et al.²⁵ A 50/50 beam splitter equally divides the light between the camera (a) and the spectrometer (b). A round shaped confined area was established by pressing a back-silvered mica surface, as a crevice former, onto a nickel coated glass disk (30 nm Ni film, PVD deposited) as previously described.²⁶ In addition, (c) a 3-electrode setup with nickel as the working electrode (WE) and two Pt wires as the reference (RE) and counter electrodes (CE) are built into this setup.

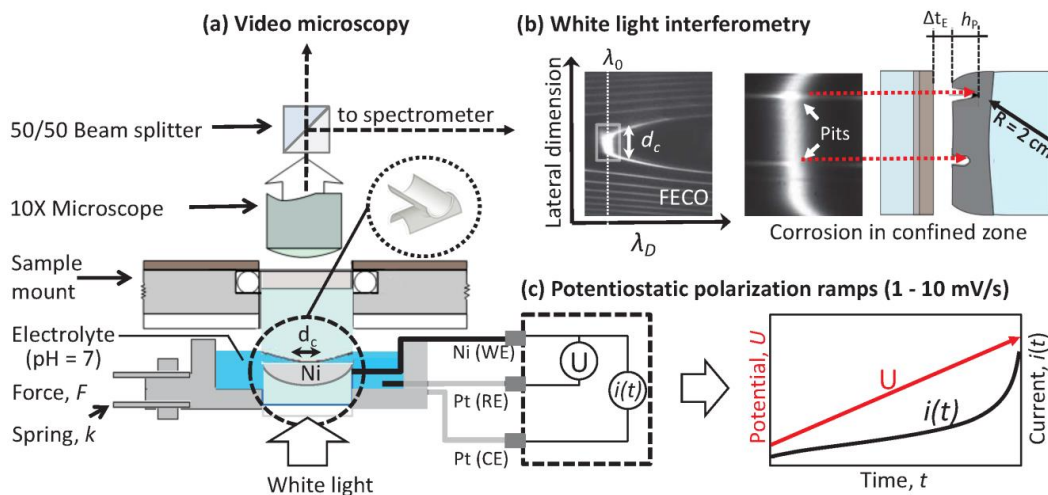


Figure 4.1 Crevice corrosion setup using the Surface Forces Apparatus. Simultaneous (a) optical video microscopy and (b) white light interferometry allow tracking of both optical images of corroding confined areas and depths h_p of corroding areas via shifts of the corroding metal mirrors via wavelength shifts ($\Delta\lambda = \Delta\lambda_D - \lambda_0$) of Fringes of Equal Chromatic Order

(FECO), and via intensity changes due to metal mirror thinning. For establishing a confined round shaped area A back-silvered mica surfaces are used as compliant crevice formers. Typical contact areas have a diameter $d_C \sim 100\text{-}300\ \mu\text{m}$. Depending on the contact force F and the resulting flattening of the compliant mica surface, a controlled pressure can be applied, resulting in a uniform equilibrium electrolyte film thickness Δt_E in the confined zone. In addition, (c) a potentiostat with a 3-electrode setup is used to apply external potential ramps to the nickel surface. Here, nickel was used as the working electrode (WE), and Pt-wires were used as the reference (RE) and counter electrodes (CE). All data is referenced to OCP, which is $-450\ \text{mV vs Ag|AgCl}$.

4.3.3 Experimental procedure.

First, a dry contact (defined as $D = 0$) was established between the mica and the nickel surface (direct contact). Afterwards, aqueous NaCl solution was injected between the two surfaces at concentrations ranging from 1 mM to 100 mM. Fringes of Equal Chromatic Order (FECO) and real-time video were recorded simultaneously as the electrochemical potential was ramped up from OCP = 0 mV (i.e., $-450\ \text{mV vs. Ag|AgCl}$) at varying rates (**Figure 4.1(c)**). During a pre-ramp period of 120 seconds after the electrolyte was injected, the ingress of electrolyte was traced and the open circuit potential (OCP) was recorded to confirm a proper working electrochemical cell. Any changes of the separation distance between the Ag and the Ni ‘mirror’ surfaces due to, e.g., ingress of water, or a shift of the Ni-mirror surface due to corrosion (conversion into oxide or dissolution), can be tracked *in situ* by monitoring three signals: (i) the distance shift of the mirror (wavelength shift of a standing wave), (ii) the change of the light intensity (i.e., more light passing through the nickel mirror due to the thinning of the reflecting nickel layer), and (iii) the width of the FECO fringes, which provides information about the roughness of the reflecting Ni surfaces. As such, all signals and parameters together allow us to distinguish clearly the difference between roughening from oxidation or water ingress. Water ingress will shift the FECO fringes to longer wavelengths, while an oxidation shifts the FECO fringe wavelength *and* increases the intensity of the light

going through the nickel mirror. Moreover, pure roughening leaves the FECO fringe wavelength position unchanged (because the average surface height does not change), yet the *width* of a FECO fringe increases proportionally with the RMS roughness. As of now, the setup is restricted to corroding thin films studied in transmission mode, extensions to bulk samples are easily possible utilizing reflection mode interferometry.²⁷

4.3.4 Nickel thickness determination.

For analyzing and determining Ni thicknesses, we can use both white light interferometry and intensity analysis of the light passing through the interferometer. First, to translate FECO wavelength shifts recorded with the imaging spectrometer using white light interferometry into distance changes, we use an in-house developed software (SFA Explorer from Max-Planck-Innovation). The SFA Explorer uses the multiple matrix method, as proposed by Schubert,²⁸ to simulate and fit interferometric spectra against measured spectra. To fully visualize evolving crevice corrosion in 3D, the part of the surface that is projected into the spectrometer slit can be rastered back-and-forth to obtain FECO for the entire crevice area. Lateral scans of the crevices can be performed with a linear motor, moving at a given speed (here 4.8 $\mu\text{m/s}$), while the frame rate was kept at 10 frames per second (fps) providing a nominal 500 nm resolution with 1 fps time resolution. With this setting, the spectroscopic dimension (wavelength and light intensity changes of 2D slices) can be scanned with frame rates up to 30 Hz. However, the third lateral microscopic dimension can only be scanned at a considerably slower rate (~ 1 Hz) – taking about 100 seconds for the entire crevice scan. As such, the FECO can only be recorded fast enough to visualize initial corrosion at a static position. Hence, we also implemented a faster Ni-thickness determination method based on utilizing the intensity changes in the optical image (top view camera) taken at a given

wavelength. For this, we calculated the intensity of typical standing waves as a function of the Ni thickness using the multiple matrix method for the given interferometer setup. This reveals a linear relation of intensity and Ni thickness (see **Figure 4.2**). Based on this result, a linearized attenuation model with an effective extinction coefficient can be used to directly extract the Ni thickness from optical images with ~ 0.5 nm depth and ~ 500 nm lateral resolution. Over the entire crevice area this analysis can be performed in real-time with frame rates up to 0.1 kHz (depending on the top view camera).

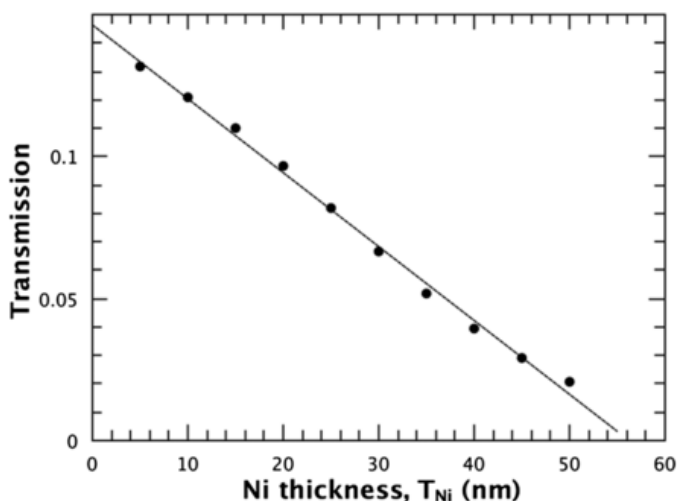


Figure 4.2 Calculated light transmission through interferometer for wavelength of ~ 575 nm using the multiple-matrix method as implemented in the SFA Explorer, indicating a linear relationship with $R^2 \sim 0.99$ for light intensity versus Ni thickness in the range relevant to the experiments discussed in the main text.

4.4 Results and Discussion

A typical corrosion experiment starts with the mica and nickel surfaces pressed together under dry condition to form a circular-shaped crevice with about $300 \mu\text{m}$ diameter. The electrolyte solution is added while the nickel electrode remains at open circuit potential (OCP). **Figure 4.3** shows how $\sim 2\text{-}3$ nm electrolyte ingresses into the confined area (i.e., where the surfaces are in close contact). This can be directly inferred from a positive mirror shift,

detected by a red shift of the FECO fringes, and was routinely recorded during the wetting of the crevice. 120 seconds after wetting the crevice and establishing a stable OCP, a potential ramp with + 1mV/s was started from the OCP towards anodic potentials. There are a number of interesting details that we observe during the corrosion of the 30 nm thick nickel surface in this configuration, which we show and discuss below.

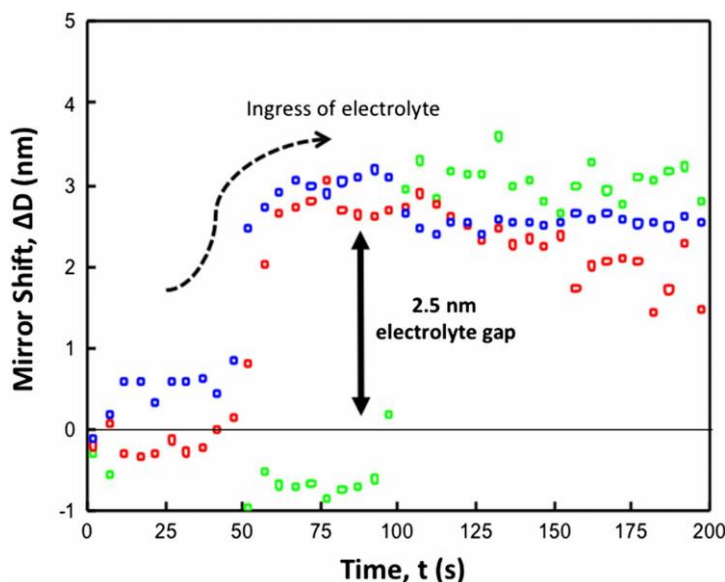


Figure 4.3 Recorded mirror shift measured by FECO during injection of electrolyte. One can clearly see that an electrolyte layer of about 2.5-nm thickness penetrates into the gap. The different colors indicate different locations inside the gap. Green is in the center, red and blue at the crevice mouth.

With the EC-SFA, one can track and quantify in real time the crevice corrosion mechanism upon application of any (here anodic) ramp. The real time imaging (recorded with the top view camera, see again **Figure 4.1(a)** of crevice corrosion initiation shown in **Figure 4.4**) indicates significant qualitative differences in the corrosion mechanism depending on the chloride concentration and the applied ramp rate. At high chloride concentration (> 10 mM), shown in **Figure 4.4(a, b)**, corrosion initiates at the crevice mouth while the inner part of the confined zone remains intact at 1 mV/s ramp rate, while this qualitative effect reverses, with

corrosion initiating inside the confined zone, at slower ramp rates of 0.5 mV/s shown in **Figure 4.4(c, d)**. Furthermore, at low chloride concentrations (<10 mM), shown in **Figure 4.4(e-f)**, corrosion initiates inside the confined zone where the surfaces are separated by only a few molecular layers of solvent (~2.5 nm liquid film, see again **Figure 4.3**), irrespective of the ramp rate (from 0.5-10 mV/s).

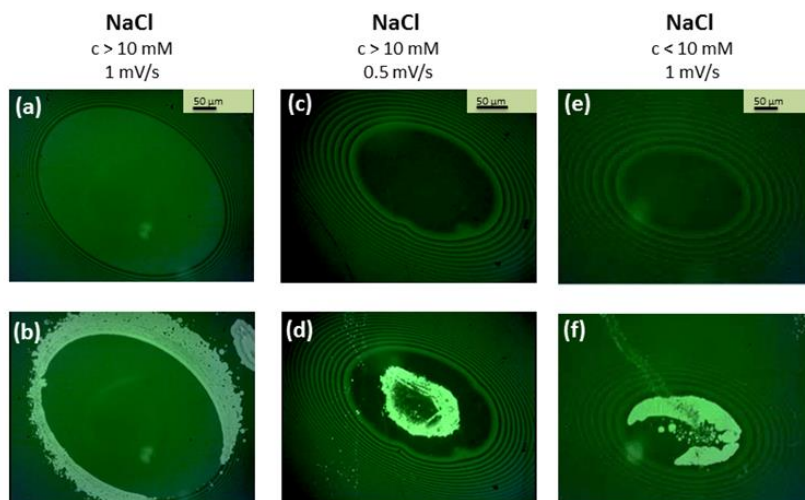


Figure 4.4 Optical microscopy of confined nickel areas while applying a linear potential ramp with $\Delta U = 1$ mV/s (see again **Figure 4.1**). Crevice corrosion (CC) of nickel in NaCl just after injection (top row) and after severe corrosion occurred (bottom row): (a, b) At $c > 10$ mM with a ramp rate of 1 mV/s indicating corrosion along the crevice rim, (c, d) at $c > 10$ mM with a ramp rate of 0.5 mV/s, indicating corrosion inside the crevice, and (e, f) at $c < 10$ mM indicating crevice corrosion again inside the confined zone. The contact (e.g., Newton rings) for each experiment appears visually different due to the different angles arising from different radii/curvatures of the metal surfaces. Interestingly, we do not observe any notable changes in the morphologies and rates of crevice corrosion due to curvature effects, contact area and aqueous separation distances (in the range 1 - 3 nm).

The rate-dependent behavior of the crevice corrosion, as seen in **Figure 4.4(b, d)**, shows the connection between active ion mobility due to the applied potential rate. At high potential rates (>1 mV/s), the chloride ions accumulate at the rim (contact boundary) enhancing the crevice corrosion rate while lower potentials (<0.5 mV/s) allow ions to diffuse into the crevice before crevice corrosion is initiated.

As expected, this behavior supports a simultaneous potential gradient and ion migration kinetic driven mechanism of crevice corrosion. In particular, crevice corrosion, has been explained previously based on a combination of the Ohmic drop (iR drop) into the crevice²⁹ and the location where an aggressive so-called critical crevice solution (CCS) with low pH (formed from the hydrolysis of Ni due to corrosion)³⁰ and high chloride concentration (ion migration to maintain charge neutrality in the crevice) is created and maintained in relation to diffusion and migration of solution species.³¹ We find that the location of crevice corrosion initiation moves towards the center of the crevice with an increasing iR drop at lower chloride concentrations. The observed crevice corrosion behavior in the experiments fits the framework of the iR drop theory because the potential inside the crevice will be lower than outside. This explains why crevice corrosion initiates and also maintains higher rates deeper into the crevice at lower solution concentrations. Conversely, at lower iR drops – i.e., at higher concentrations – crevice corrosion is initiated closer to the crevice mouth. With the lower iR drop, faster ion migration into the rim-region (compared to migration into the center region) triggers the formation of a CCS at a region closer to the crevice mouth (31). As anticipated from macroscopic observations, crevice corrosion depends on a delicate interplay of both the transport and depletion kinetics of active species which profoundly change the qualitative corrosion mechanism.

There are two electrochemical processes going on simultaneously here that need to be distinguished, which we now refer to as the ‘active’ and ‘passive’ processes. The active process involves the applied potential, U , that generated the current flow and is quantified by the iR values and changes as corrosion progresses. However, at zero applied potential there also exists a ‘passive’ or ‘resting’ potential, U_0 , as in a capacitor or battery, even in the absent

of any current flow or electrochemical reactions. The value of U_0 is determined by the difference in the ‘double layer’ surface potentials of the two (dissimilar) surfaces – nickel and non-conducting mica in this case – as well as the aqueous distance between them and the Debye length. This potential, too, will change as corrosion progresses and presumably also contribute to the rate of pit growth. A simple calculation based on electric double-layer theory³⁶ shows that a 3 nm deep pit will cause a change in U_0 of 30-60 mV. We are not able to quantitatively establish which of these processes dominate the iR drop or the change in the different potentials associated with this corrosion process.

Our data not only provides a unique real-time view of this expected behavior during crevice corrosion initiation, but an *in-situ* EC-SFA experiment enables the ability to track and quantify nanoscopic details of the initial growth mechanism. This includes qualitative and quantitative changes of corrosion dynamics into local currents with nano-scale depth (single active site) accuracy and microscale lateral resolution.

Figure 4.5 shows two snapshots of a (left) microscopic image, and (right) a 3D analysis of the Ni thickness at progressing time and increasing potential (+1 mV/s). The displayed experiment was recorded at 1 mM solution concentration of NaCl.

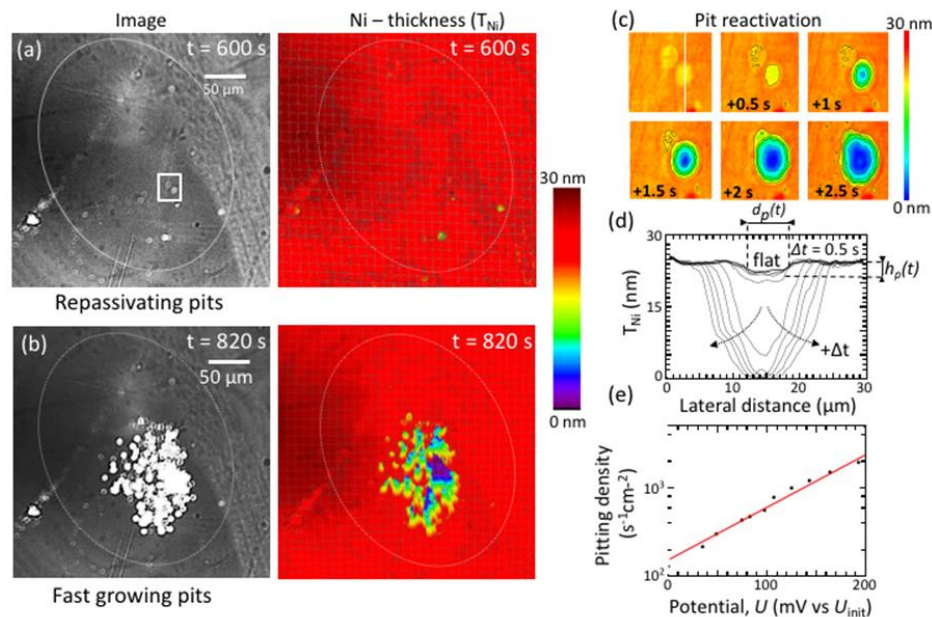


Figure 4.5 Reactivation of initially passivated pits above the critical corrosion potential. (a) Optical image (left) and corresponding Ni thickness contour plot (right) showing initial re-passivating pits inside and outside the confined zone (region marked) after 600 seconds linear anodic polarization with 1 mV/s starting from OCP (-450 mV vs Ag|AgCl). (b) Same confined zone after 820 seconds polarization (i.e., 820 mV vs OCP) showing fast active pitting inside the confined area. (c) Enlarged Ni-thickness contour plot of pit that reactivates (see also a): region marked by square), and (d) depth profile as function of time recorded at line indicated in (c). Pit diameter $d_p(t)$ and pit depth $h_p(t)$ are indicated for the re-passivated state. Corrosion will continue until consumption or re-passivation of the nickel surface. (e) Pitting density of re-passivating pits referenced to the initiation potential $U_{init} \sim 300$ mV (vs. OCP) where the first pit was detected in the field of view. Individual pit counting was terminated once a critical pit started fast corrosion.

First, we observe that crevice corrosion of mica-confined nickel surfaces does not initiate as homogenous, locally uniform corrosion. One can observe the formation of nanoscale-to-microscale pits that evolve with exceptionally rapid kinetics (in the μ s-range) before they become metastable, both inside and outside the crevice before the initiation of nickel crevice corrosion in confinement.

In particular, **Figure 4.5(a)** shows an optical image indicating pits with very similar diameters of $d_p(t) \sim 6-7 \mu\text{m}$. The first pit was detected about 300 second after anodic polarization was started (i.e., at 300 mV vs OCP). The average pit depth of these initial pits is

about $h_p = 2\text{-}4$ nm and the bottom is flat, as can also be seen in the depth profile shown in **Figure 4.5(c, d)**. These pits appear inside and outside the confined zone within less than 500 μs (one recorded frame), indicating a localized and extremely rapid, yet self-inhibiting, corrosion process. These initial pits do not immediately penetrate the entire Ni layer as expected by typically estimated anodic pit current densities.¹⁰ These pits form within less than 500 μs (i.e., within one recorded frame), however, once a typical critical diameter $d_p(t) \sim 6\text{-}7$ μm is reached, the formed pits become inactive and the localized corrosion stops (i.e., arrests). We can directly calculate the local charge that transfers in a single site based on a volumetric analysis of nickel loss. From the estimated local Ni-thickness loss (see **Figure 4.5(c, d)**), we can calculate a charge transfer of 0.97 μC per pit, which estimates a minimum pitting current density of >5 A/cm^2 for these pits that appear within $t < 500$ ms. These directly measured single pit current densities compare well to estimates from penetration time measurements using thin metal films,³² where a range from 1-30 A/cm^2 was estimated. These previous studies find that the anodic pit current density – derived from the penetration time - depends on the thickness of the metal film and the applied potential. Our data extends this view, and demonstrates that initial – non-penetrating - pits show rather uniform diameters and depth, without any strong correlation with the applied potential. **Figure 4.53(e)** shows, that these initial, often referred to as *non-critical*, pits pop up with an exponentially increasing probability with the increasing potential. We argue that these non-critical pits may be central to establishing the local solution conditions that are necessary to catalyze the corrosion rate of a critical pit that will penetrate the thin film. Considering the corroded volume of nickel in such a pit, we estimate that the solution temporarily reaches very high concentrations.

In addition, the low aspect ratio of pit height to diameter ($h_p(t)/d_p(t) \sim 10^{-3}$) of these non-critical pits suggests that the initial *lateral* corrosion is at least three orders of magnitude faster than the initial *vertical* corrosion into the material. The lateral resolution ($\sim 0.5 \mu\text{m}$) constrains the direct observation of the nanoscale morphology (e.g., structural or chemical defects) preventing an accurate description of the pit initiation; however, other studies have observed direct evidence of such defects using *in situ* near-field microscopy techniques.^{12,33,34} Combination of the observed circular shaped pits and the flat bottom (i.e., counter bore shape), suggests that a very local oxide breakdown – possibly at defect sites – triggers the initial pit formation with epitaxial corrosion dynamics. Corrosion triggering defects may significantly lower the activation energy for passive layer dissolution. Once a local defect or impurity in the metal or oxide triggers pit initiation, initially sharp and convex edges of an evolving pit generate a strong electric field gradient that accelerates lateral corrosion, rapidly increasing the lateral diameter of the pit while the depth increases about 3 orders of magnitude more slowly.

Figure 4.6 shows a proposed model of the initial dissolution and early time pit growth based on the electrochemically enhanced dissolution model proposed in Chapter 3. The potentiodynamic ramp of the potential toward positive voltages increases the local potential and surface charging. Initially, the apposing mica and Ni surfaces are negatively charged, thereby constraining the diffusion of chloride ions into the cavity. As the potential of the nickel surface increases, the charge of the nickel surface increases to positive values; this results in the migration of chloride ions into the positively charged cavity to maintain charge neutrality. In addition, the closely apposed negatively charged mica surface further enhances the local electric field.³² A structural surface defect (e.g., a dislocation, or an inclusion) locally

accumulates surface charges and generates a Rayleigh-type instability³⁸ that lowers the interfacial tension of the solid–solution interface and favors dissolution. These defects can then act as corrosion trigger points, where the activation energy for nickel to escape from the surface is lowered as seen in **Figure 4.6(a)**. Once a defect dissolves the top layers of the material, very fast lateral growth starts with pits growing to a size of $\sim 7\ \mu\text{m}$ in diameter and a depth of only a few nanometers within less than $500\ \mu\text{s}$, before corrosion inside these pits arrests again. This indicates that the initial lateral corrosion is at least three orders of magnitude faster than initial corrosion into the material. These initial “noncritical” pits (i.e., pits that stop fast growth) form a very consistent and reproducible “counter-bore” shape with a sharp (i.e., highly curved) edge at the rim. The sharp convex edge generates a strong electric-field gradient that adds another, highly repulsive, electrostatic force between any ions and dipoles. This additional force enhances the nickel dissolution/corrosion at the sharp edge—rapidly increasing the lateral diameter of the pit while the depth increases much more slowly (several orders of magnitude slower) as depicted in **Figure 4.6(b)**. Finally, as the pit grows the edge becomes less sharply curved, leading to a weaker electric-field gradient. The bottoms of the pits were generally not completely flat or smooth, having a gently undulating shape, which is in line with the argument that local high curvature is a factor in governing evolution of growing pits. In addition, due to confinement of the apposing surface (dotted area), the solution within the pit becomes saturated with nickel solutes, which will arrest the corrosion reaction as seen in **Figure 4(c)**.

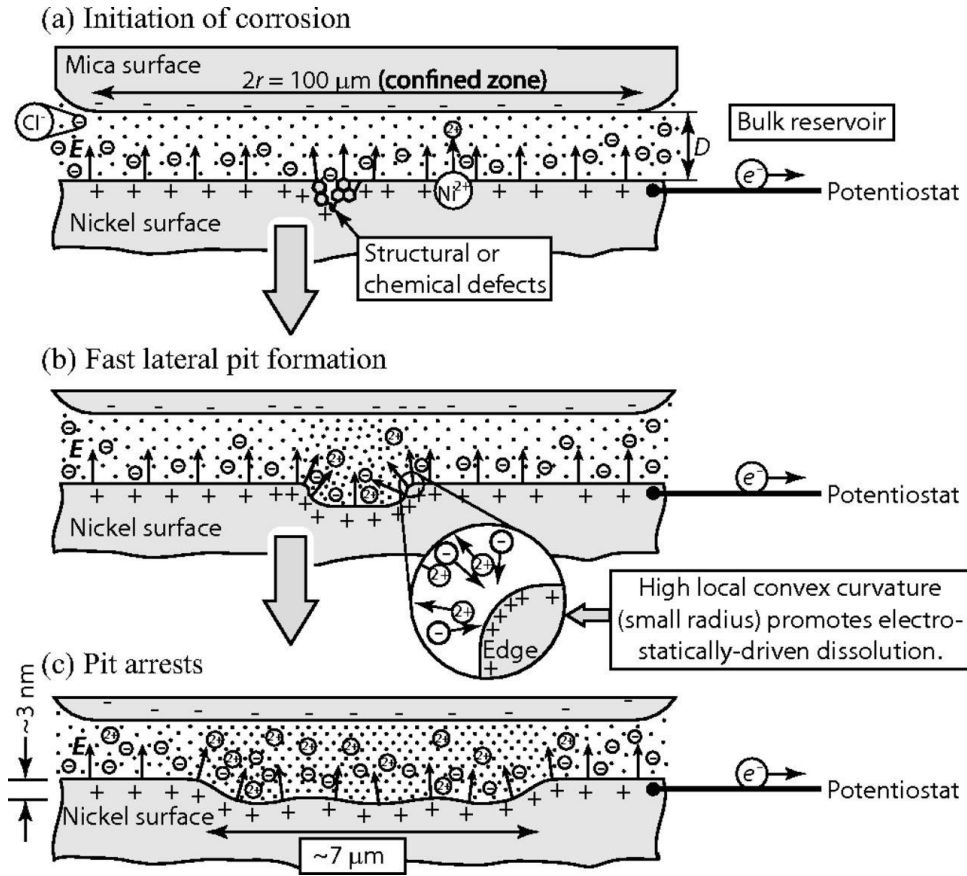


Figure 4.6 Proposed mechanism of nickel/nickel oxide dissolution/corrosion based on the electrochemically enhanced dissolution model reported in Chapter 3.

As shown in **Figure 4.5(c)**, above a critical potential (here at +400 mV vs. OCP), an arrested pit within the confined zone (at the rim or the center depending on the chloride concentration) breaks the initial pit size of $d_p(t) \sim 6-7 \mu\text{m}$ and $h_p(t) \sim 2-3 \text{ nm}$ and rapidly evolves into a larger depth. Again, from the estimated local Ni-thicknesses loss we calculate a charge transfer of $2.75 \mu\text{C}$ for this critical pit, which estimates a pit current density of $\sim 25 \text{ A/cm}^2$, which is up to 5 times faster compared to the growth rate of the re-passivating pits. From **Figure 4.5(d)** the initial depth penetration rate of this critical pit can be estimated at about 25 nm/s or $90 \mu\text{m/hour}$.

Moreover, see **Figure 4.5(b)**, the critical pit triggers and catalyzes a rapid evolution of new pits as well as reactivates other arrested pits in its immediate surroundings. This

collaborative pit growth is most likely due to a strong variation of solute concentrations inside the confined zone (see supporting information for videos of the rapid evolution of pits) and the formation of a critical crevice solution (CCS) with low pH and high chloride concentration.

The collaborative pit growth behavior supports the hypothesis that crevice corrosion of nickel in chloride solutions initiates as *self-catalyzed pitting corrosion due to chemical changes in the crevice solution within the confined areas*. As expected, the ongoing metal dissolution inside the confined region leads to an excess of positive charge in the crevice solutions, and to a lowering of the pH due to metal ion hydrolysis. This excess of local charge is largely compensated by the relatively faster migration of chlorides into the confined zone, while metal ion diffusion out of the crevice is relatively slower due to greater ion mobility of chlorides.³¹ Pits that are formed outside the confined crevice area are all swiftly arrested, even at higher potentials, which may be due to the lack of build-up of local aggressive electrolyte environments.^{31,35}

Based on the corrosion rates found for single pits (together with their measured dimensions and growth kinetics, see above), and for the entire confined zone we can finally compare integral currents (inside and outside of confinement) to currents estimated from volumetric Ni-thickness loss for localized corrosion sites. **Figure 4.7** shows excellent agreement indicating that the deviation from the characteristic exponential Tafel slope (with $i_0 \sim 8 \cdot 10^{-7}$ A/cm²) is caused by the additional current density from defect breakdown into the observed non-critical pits. Also, the corrosion in confinement is fast and consumes the entire confined area within ~100 seconds. Interestingly, the fast corrosion of the confined zone does not add significantly to the overall current due to the small area of our confined zone compared to the entire sample area. Locally in confinement, however, the crevice corrosion current

density ranges up to 300 A/cm^2 , which is a reasonable number given that about 10-20 critical pits with anodic pit current densities of $\sim 25 \text{ A/cm}^2$ (see above) progress at the same time. As such, the EC-SFA provides a unique measure to *in-situ* quantify the local current density in confinement, which is independent of any competitive reduction reactions such as local hydrogen evolution.

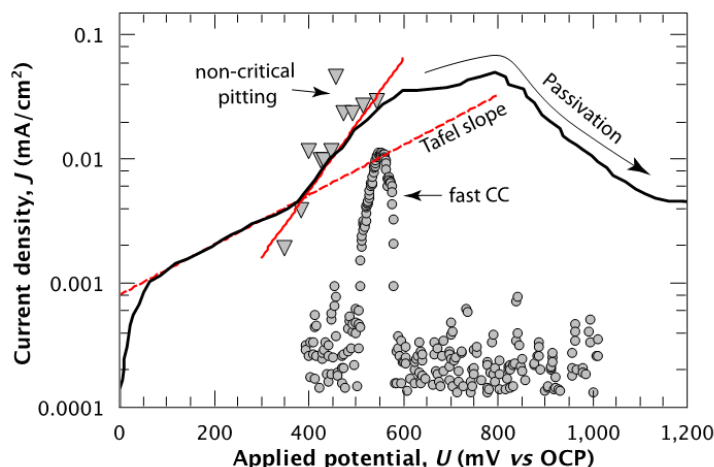


Figure 4.7 Electrochemically measured current density for experiment shown in **Figure 4.5** (solid line). The current estimated from the pitting density of non-critical pits (triangles) as well as the current density originating from the fast crevice corrosion within the confined zone are compared to the integral current (*cf.* text for details). At higher anodic potential of $\sim 800 \text{ mV}$ ($\sim 450 \text{ mV vs Ag|AgCl}$), polarization leads to the expected passivation of the outside region. The solid red line is a guide to the eye for the non-critical pitting curve that deviates from the Tafel slope, as indicated by the dashed red line.

4.5 Conclusions

In summary, the EC-SFA provides a unique setup to directly visualize individual corrosion sites (here pits) in confined spaces in real time and to analyze their initial growth kinetics. Compared to standard optical microscopy with transparent crevice formers, the depth resolution of evolving initial corrosive degradations is superior, allowing measurement of pit depths in 3D with sub-nanometer and ms-time resolution. Also, the EC-SFA uniquely enables

measurement of single pit current densities and growth shapes in 3D (both laterally and in depth), as well as time-evolving pit densities within the confined zone.

Initial corrosion inside nickel crevices proceeds as preferential and self-catalyzed “pitting corrosion” (inhomogeneous localized dissolution with the formation of pits), presumably at surface defects within the confined zone. Our data also confirms that there is a strong interplay between migration kinetics of chlorides, bulk chloride concentrations, and the related iR drop (voltage drop), which leads to pronounced qualitative changes in the location (at the rim or center) at which pits form, and their subsequent kinetics. Importantly, local fast corrosion seems to play a crucial role in the initial development of a critical crevice solution within the crevice that drives the observed pit growth and propagation, suggesting that understanding and controlling surface chemistry and morphology are essential to prevent the onset of corrosion in the present system. Pit current densities are $\geq 5 \text{ A/cm}^2$ for swiftly arresting non-critical pits, and $\sim 25 \text{ A/cm}^2$ for critical pits.

The above conclusions may be general observations for crevice corrosion systems, however further studies with other corroding systems are needed to potentially extract and verify general rules and/or models as well as system dependencies of local corrosion rates *in situ* with nano-to-microscale resolution. The observations of pit growth under influence of an applied electrostatic force is consistent with the proposed electrochemically enhanced dissolution model. A deeper understanding of the changes in the electrochemical environment is required to understand the dynamics of ions relevant to transport mechanics, reaction kinetics, and electrostatics.

References

1. de Boer RB, Nagtegaal PJC, Duvys EM (1977) Pressure solution experiments on quartz sand. *Geochim. Cosmochim. Acta* 41:257.
2. Alcantar N, Israelachvili J, Boles J (2003) Forces and ionic transport between mica surfaces: Implications for pressure solution. *Geochim. Cosmochim. Acta* 67(7):1289-1304.
3. Mishra N, *et al.* (2014) Controlling the surface roughness of epitaxial SiC on silicon. *J. Applied Phys.* 115:203501.
4. Piotrowski O, Madore C, Landolt D (1998) The mechanism of electropolishing of titanium in methanol-sulfuric acid electrolytes. *J. Electrochem. Soc.* 145:2362.
5. Laycock NJ, Stewart J, Newman RC (1997) The initiation of crevice corrosion in stainless steels. *Corros. Sci.* 39(10-11):1791-1809.
6. Lott SE (1989) The Role of Inclusions on Initiation of Crevice Corrosion of Stainless Steel. *J. Electrochem. Soc.* 136(4):973.
7. Grippo J, Simring M, Coleman T (2012) Abfraction, abrasion, biocorrosion, and the enigma of nancarious cervical lesions: a 20-year perspective. *J. Esthet. Restor. Dent* 24:10.
8. Lin H, Bumgardner JD (2004) In vitro biocorrosion of Co-Cr-Mo implant alloy by macrophage cells. *J. Orthop. Res* 22:1231.
9. Jakupi P, Noel JJ, Shoesmith DW (2011) Crevice corrosion initiation and propagation on Alloy-22 under galvanically-coupled and galvanostatic conditions. *Corros. Sci.* 53(10):3122-3130.

10. Böhni H (1992) Localized Corrosion - Mechanisms and Methods. *Materials Science Forum* 111-112:401-414.
11. Böhni H (1987) Breakdown of Passivity and Localized Corrosion Process. *Langmuir* 3(6):924-930.
12. Marcus P, Maurice V, Strehblow HH (2008) Localized corrosion (pitting): A model of passivity breakdown including the role of the oxide layer nanostructure. *Corros. Sci.* 50(9):2698-2704.
13. Maier B, Frankel GS (2010) Pitting Corrosion of Bare Stainless Steel 304 under Chloride Solution Droplets. *J. Electrochem. Soc.* 157:C302.
14. Hastuty S, Nishikata A, Tsuru T (2010) Pitting corrosion of Type 430 stainless steel under chloride solution droplet. *Corros. Sci.* 52(6):2035-2043.
15. Zadorozne NS, Giordano CM, Rodríguez MA, Carranza RM, Rebak RB (2012) Crevice corrosion kinetics of nickel alloys bearing chromium and molybdenum. *Electrochim. Acta* 76:94-101.
16. Laycock NJ, Newman RC (1997) Localised dissolution kinetics, salt films and pitting potentials. *Corros. Sci.* 39(10-11):1771-1790.
17. Malki B, Souier T, Baroux B (2008) Influence of the Alloying Elements on Pitting Corrosion of Stainless Steels: A Modeling Approach. *J. Electrochem. Soc.* 155(12):C583.
18. Kim YH, Frankel GS (2007) Effect of Noble Element Alloying on Passivity and Passivity Breakdown of Ni. *J. Electrochem. Soc.* 154(1):C36.
19. Lu BT, Luo JL, Lu YC (2007) A Mechanistic Study on Lead-Induced Passivity-Degradation of Nickel-Based Alloy. *J. Electrochem. Soc.* 154:C379-C389.

20. Knight SP, *et al.* (2010) In situ X-ray tomography of intergranular corrosion of 2024 and 7050 aluminium alloys. *Corros. Sci.* 52(12):3855-3860.
21. Greene GW, Kristiansen K, Meyer EE, Boles JR, Israelachvili J (2009) Role of electrochemical reactions in pressure solution. *Geochim. Cosmochim. Acta* 73:2862.
22. Israelachvili J, *et al.* (2010) Recent advances in the surface forces apparatus (SFA) technique. *Rep. Prog. Phys.* 73(3):036601.
23. Israelachvili JN, Alcantar NA, Maeda N, Mates TE, Ruths M (2004) Preparing Contamination-free Mica Substrates for Surface Characterization, Force Measurements, and Imaging. *Langmuir* 20:3616-3622.
24. Frechette J, Vanderlick TK (2005) Control of adhesion and surface forces via potential-dependent adsorption of pyridine. *J. Phys. Chem. B* 109:4007-4013.
25. Israelachvili JN (1973) Thin film studies using multiple-beam interferometry. *J. Colloid Interf. Sci.* 44(2):259-272.
26. Shrestha BR, *et al.* (2015) Real-Time Monitoring of Aluminum Crevice Corrosion and Its Inhibition by Vanadates with Multiple Beam Interferometry in a Surface Forces Apparatus. *J. Electrochem. Soc.* 162(7):C327-C332.
27. Connor J, Horn RG (2003) Extending the surface force apparatus capabilities by using white light interferometry in reflection. *Rev. Sci. Instrum.* 74(11):4601-4606.
28. Schubert M (1996) Polarization-dependent optical parameters of arbitrarily anisotropic homogeneous layered systems. *Phys. Rev. B* 53:4265.
29. Scully H (1994) Lifetime Prediction for Organic Coatings on Steel and a Magnesium Alloy Using Electrochemical Impedance Methods. *Corros. Sci.* 50(9):705-716.

30. Lev O, Fan F, Bard A (1988) The application of scanning tunneling microscopy to in situ studies of nickel electrodes under potential control. *Electrochem. Soc.* 135:783.
31. Kelly RG (2003) Crevice Corrosion. *Corrosion and Oxide Films*, Wiley-VCH, Vol 4.
32. Frankel GS, Dukovic JO, Brusica V, Rush BM, Jahnes CV (1992) Pit Growth in NiFe Thin Film. *J. Electrochem. Soc.* 139(8):2196-2201.
33. Maurice V, Klein LH, Marcus P (2001) Atomic Structure of Metastable Pits Formed on Nickel. *Electrochem. Solid-State Lett.* 4:B1-B3.
34. Maurice V, Marcus P (2012) Passive films at the nanoscale. *Electrochim. Acta* 84:129-138.
35. Frankel GS (1998) Pitting Corrosion of Metals A review of the Critical Factors. *J. Electrochem. Soc.* 145(6):2186-2198.
36. Israelachvili JN (2011) *Intermolecular and Surface Forces*, 3rd ed., Academic Press.

Chapter 5: Molecular network formation in alkali-activated aluminosilica cements

5.1 Abstract

The initial formation and development of structure, as well as the influences of structure on macroscopic physical properties, is largely unknown for many aluminosilica materials, especially in the field of inorganic polymer binders (IPBs), which are attractive as low-CO₂ cement materials. Here, we determine the molecular-level structures and compositions during early formation of aluminosilica networks under strong alkaline (pH >14) conditions using amorphous silica and alumina colloidal microparticle precursors as SiO₂ and Al₂O₃ sources, respectively. Specifically, the transient evolution of local ²⁷Al, ²⁹Si, and ¹H environments at early stages of network formation and condensation is determined using dynamic nuclear polarization surface-enhanced solid-state NMR spectroscopy (DNP-SENS) techniques, with complementary X-ray diffraction and electron microscopy analyses. One- and two-dimensional DNP-enhanced ²⁹Si{¹H} and ²⁷Al{¹H} heteronuclear correlation (HETCOR) and ²⁹Si{²⁷Al} heteronuclear multiple quantum correlation (HMQC) spectra establish the hydration environments and ²⁷Al-O-²⁹Si network connectivities of the aluminosilica network, which forms on the surface of the alumina particles. As network formation time increases, the ²⁷Al species in the aluminosilica network become locally-ordered and more condensed, which corresponds with development of macroscopic strength of the aluminosilica material. Additionally, the early dissolution behavior of at the silica and alumina interface is characterized using the SFA, providing insights into the local ion structure near the surface during early network formation steps. The results demonstrate the ability of combining SFA

and DNP-enhanced NMR techniques to measure and characterize local transient structures at surfaces in aluminosilica networks, which provides important insights into the influences of impurities and solution chemistry in developing inorganic networks with desirable macroscopic properties, which is crucial for the development of new IPB formulations.

5.2 Introduction

Aluminosilica materials are present in a wide variety of natural and technological systems with diverse applications in catalysis, structural materials, and separations.¹⁻³ Such materials are composed of corner-sharing AlO_4^- and SiO_4^{2-} tetrahedra and charge-balancing cationic species (e.g., H^+ , Na^+ , Ca^{2+} , etc.) that can assemble into diverse structures and morphologies with properties that vary drastically, even for materials with similar bulk compositions. For example, aluminosilica(te) materials such as zeolites and inorganic polymer binders (IPBs) are highly condensed, partially ordered, and exhibit a wide range of properties which enables their technological applications ranging from low- CO_2 cement materials to heterogeneous catalysis. Such highly-condensed aluminosilica networks may be formed from silica and alumina sources reacted in an aqueous medium, either as a dense gel or a colloidal suspension, often at elevated temperatures and/or pressures. The resulting silica and alumina suspensions formed can be completely or partially dissolved, depending on the reaction conditions and precursor compositions, which results in the formation of mixtures with different morphologies, structures, and properties.¹⁰

Small changes in reaction conditions can lead to significantly different structures with unique geometries and properties; however, the characterization and understanding of the different networks formed is difficult and not well known.⁴ For example, in zeolite syntheses, slightly different reaction conditions (e.g., pH, temperature, ionic concentration, presence of

organic structure directing agents) can significantly alter the pore sizes, shapes, and connectivities, resulting in changes to the macroscopic properties of the materials for applications in catalysis, as ion-exchange, nanoparticle supports, and molecular sieves.⁵⁻⁷ In inorganic polymer binders, the reaction conditions greatly influence the development of macroscopic strength. IPBs have the potential to serve as a low-energy, low-CO₂ alternative to ordinary Portland cement (OPC), however slight variations in precursor composition can result in materials that do not set at all, while other starting materials can yield cements with compressive strength almost three times greater than that of OPC.⁸ The difficulty in obtaining desirable structural properties from IPBs derived from similar starting materials is indicative of our lack of understanding of the formation of the aluminosilica networks and how these networks relate to the development of micro- and macroscopic properties such as the microstructure, network strength, mechanical properties, stability, and durability.⁹

The generally accepted mechanism for aluminosilica material formation includes three distinct steps: (1) initial dissolution of the surface alumina and silica species, (2) nucleation of discrete particles of the new phase, and (3) growth of the aluminosilica network.¹¹ To understand the formation of aluminosilica networks with significantly different properties, further understanding of the initial formation and evolution of the network structure and properties over time is required. At early reaction times, aluminosilica networks can form dense, locally-ordered structures that evolve over time,² though lack long-range or crystalline order. Determining the local structures and interactions of aluminosilica networks that correspond to the development of macroscopic strength properties has been exceptionally challenging, especially for early times, due in part to the difficulty in characterizing the molecular-level changes occurring at the surface and understanding the relationship between

these molecular-level changes with macroscopic properties. These challenges have limited understanding of the development of specific microstructures and macroscopic mechanical properties of the materials.¹⁰ To advance the technological applications of aluminosilica networks in IPBs, a more detailed understanding of the early stages of network formation is required in relation to changes in the micro- and macroscopic strength properties of the materials.

In this work, we study the early network formation of aluminosilica networks formed from amorphous silica and alumina sources in strongly alkaline (6 M NaOH) reaction conditions to obtain a more detailed understanding of IPB network formation and evolution during the initial condensation and growth of the aluminosilica network. Using one- (1D) and two-dimensional (2D) solid-state dynamic nuclear polarization (DNP) nuclear magnetic resonance (NMR) spectroscopy in combination with the surface forces apparatus (SFA), we directly characterized the local molecular interactions and environments of ²⁹Si and ²⁷Al species within the aluminosilica networks formed after different reaction times. Notably, 2D solid-state DNP NMR spectra establish the ²⁹Si-O-²⁷Al connectivities within the aluminosilica networks at different stages of the network formation and evolution, providing detailed information on local structures that occur and significantly alter the aluminosilica network structure which has not been, to our knowledge, previously observed in these highly alkaline environments. The early dissolution behavior was characterized using the SFA to observe changes in the near-surface regime, providing a better understanding of the initial stages of dissolution and subsequent network formation processes. The thorough characterization of the local molecular network evolution, from dissolution to early aluminosilica formation, provides a unique opportunity to understand the development of micro- and macroscopic properties, bridging

the gap between initial molecular-level network formation and the development of desirable properties in IPBs and zeolites.

5.3 Experimental methods

5.3.1 Synthesis of IPB-like aluminosilica network

An aluminosilica network analogous to fly ash-based IPB formulations was synthesized using a mixture of amorphous, 50 nm alumina (US Research Nanomaterials, Inc.) and silica (PPG *Hi-Sil*) colloidal nanoparticles in an Si/Al atomic ratio of 2. The composition was chosen to be similar to many standard fly ash materials. The colloidal particles were suspended in a 6 M NaOH (Sigma-Aldrich) solution with a water/solids (w/s) ratio of 2 and allowed to react for 2 h to X days at 295 K while shaking, after which the mixture was neutralized with equimolar, equivolume HCl and freeze-dried to completely halt the network formation reaction at each desired timepoint.

5.3.2 Scanning electron microscopy and X-ray diffraction

Scanning electron microscopy (SEM) images and energy-dispersive X-ray spectroscopy (EDS) spectra were acquired with a FEI XL30 Sirion FEG SEM with EBSD and EDX on the unreacted and reacted aluminosilica powder samples. The images were recorded with an electron beam voltage of 3 – 5 kV and magnifications ranging from 30× to 10,000×. In some instances, the sample was coated with a 70:30 Au to Pd thin film to improve conductivity and image resolution, as indicated on the applicable images.

5.3.3 Surface forces apparatus (SFA)

SFA measurements were performed with an SFA 2000 (manufactured by SurForce LLC., Goleta, California) to measure the interaction forces between asymmetric SiO₂ and a 10 nm Al₂O₃ coated SiO₂ composite surfaces. The surfaces were fabricated as discussed in Chapter 2, on cylindrically curved silica disks ($R \approx 2$ cm) and mounted in the SFA in a crossed cylinder geometry. Prior to all SFA experiments, the thickness of the deposited SiO₂ and Al₂O₃-modified SiO₂ surfaces were measured to ensure the correct thickness for the interferometry distance calculations. A reservoir of DI water was added to the box to ensure that the droplet of 6M NaOH did not evaporate over the course of the experiment. Additional details regarding the SFA experimental setup are described in Chapter 2. A detailed description of the force and distance measuring methods can be found in Ref. 32.

5.3.4 1D and 2D solid-state DNP NMR

All solid-state 1D and 2D DNP-enhanced ²⁹Si{²⁷Al}, ²³Na{²⁹Si}, ²³Na{¹H}, ²⁷Al{¹H}, and ²⁹Si{¹H} NMR experiments were carried out on a Bruker ASCEND 400 DNP-NMR spectrometer with a 9.4 Tesla superconducting magnet operating at 399.95, 104.28, 105.84, and 79.46 MHz for ¹H, ²⁷Al, ²³Na, and ²⁹Si nuclei, respectively, and equipped with a gyrotron and microwave transmission line capable of providing 263 GHz microwave irradiation at the sample and a variable-temperature 3.2 mm triple-resonance H-X-Y MAS probe. The 1D and 2D DNP-enhanced ²⁹Si{¹H}, ²⁷Al{¹H}, ²³Na{²⁹Si}, and ²⁹Si{²⁷Al} spectra were acquired at 95 K, 8 kHz MAS, under continuous microwave irradiation at 263 GHz, with 100 kHz SPINAL-64 proton decoupling,¹⁷ and in the presence of 8 mM TEKPol biradical¹⁶ in frozen 1,1,2,2-tetrachloroethane (DNP solvent), which do not influence the structure of the material.¹⁸ Experimentally-optimized repetition times of 2-10 s were used for best signal

sensitivity. The solid-state 2D DNP-enhanced Solid-state 2D DNP-enhanced dipolar-mediated $^{29}\text{Si}\{^{27}\text{Al}\}$ spectra were acquired using a dipolar-mediated Heteronuclear Multiple Quantum Correlation (HMQC) experiment based on SR4_1^2 recoupling^{19,20} using $^{29}\text{Si}\{^1\text{H}\}$ cross-polarization with a contact time of 5 ms to circumvent the effects of the long longitudinal ^{29}Si spin relaxation times. A 1 ms ^{27}Al double-frequency sweep pulse²¹ was applied to invert the satellite transitions of quadrupolar ^{27}Al nuclei ($I = 5/2$) and improve sensitivity. Experimentally optimized recoupling times of 4.5 ms were used for best overall efficiency.

5.4 Results and discussion

5.4.1 Long-range order and morphology of aluminosilica materials crosslinked for short reaction times

Aluminosilica networks form between colloidal Al_2O_3 and SiO_2 particles reacted under alkaline conditions (6 M NaOH), which are tracked as a function of reaction time using wide-angle X-ray diffraction (XRD) and scanning electron microscopy (SEM), shown in Figure 1. The XRD patterns of a mixture of amorphous Al_2O_3 and SiO_2 particles (atomic Si/Al ratio ~ 2) after reaction at 295 K in 6 M NaOH solution (water/solids ratio ~ 2) do not change significantly after reaction times of 24, 72, or 384 h (**Fig. 5.1a,b,c**), indicating that there is no detectable change in the long-range periodic ordering of the reaction products. The XRD patterns exhibit relatively narrow reflections that are indexed to crystalline NaCl species (red dots) formed as a result of acid neutralization of the reaction mixture with HCl to arrest the reaction progress at the end of each time point. Additional reflections are indexed to an aluminum hydroxide phase (blue dots), indicating that a crystalline $\text{AlO}(\text{OH})$ impurity is

present in the Al_2O_3 precursor materials. The positions and widths of the XRD reflections from the crystalline NaCl and $\text{AlO}(\text{OH})$ phases are the same for the materials reacted for 24, 72, and 384 h, indicating that the $\text{AlO}(\text{OH})$ phase does not participate to a detectable extent in the development of the aluminosilica network and that the formation of NaCl on quenching the reaction occurs for all of the different time points. Each of the XRD patterns also exhibit a broad, featureless reflection at $22^\circ 2\theta$, which arises from regions of the material that lack long-range order,²² such as the aluminosilica networks formed by the reaction of SiO_2 and Al_2O_3 in highly alkaline aqueous media.²³ Due to the similar electron densities of Al and Si atoms, as well as the inability of scattering techniques to resolve regions of the material that lack long-range order, the XRD patterns are unable to provide further insights into the development of aluminosilica network formed under alkaline reaction conditions.

By comparison, the morphology of the Al_2O_3 and SiO_2 particle mixture changes significantly after reaction in 6 M NaOH for 24, 72, or 384 h, as shown by the representative SEM images in **Fig. 5.1c,d,e**. After 24 h reaction time, the mixture is predominately composed of a low-density network of aggregated 50 nm particles, indicating that the colloidal Al_2O_3 and SiO_2 particles (~50 nm mean diameter) do not change significantly in size after 24 h reaction. After 72 h reaction, the aggregated particles range in diameter from 100-500 nm, indicating that the colloidal Al_2O_3 and SiO_2 particles have partially dissolved and reacted to form larger amorphous particles. Additional large (~3 μm), irregular particles are also observed in the SEM images, which are morphologically similar to the irregular particles observed after 384 h reaction. Large, cubic crystals are also observed in some of the SEM images of the reacted Al_2O_3 and SiO_2 particles, which are attributed to crystalline NaCl, observed using XRD, particles formed during the neutralization of the reaction mixture,

corroborating the macroscopic phase segregation of the NaCl and aluminosilica regions of the material. After reaction for 384 h, the material is composed predominately of large, aggregated 2-10 μm particles, indicating that the small colloidal SiO_2 and Al_2O_3 particles have almost completely dissolved, reprecipitated, and crosslinked to form an aluminosilica IPB material after the long reaction time.

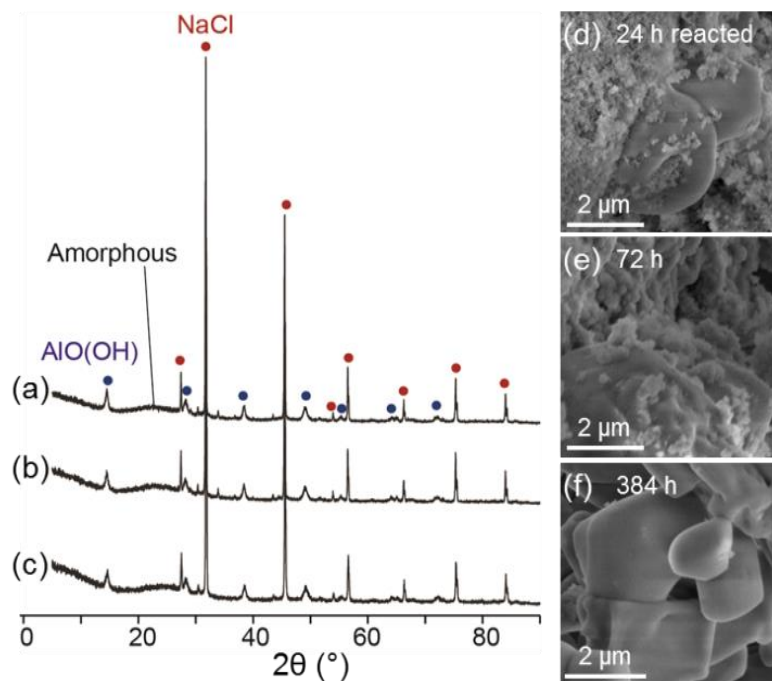


Figure 5.1 (a,b,c) XRD patterns and (d,e,f) representative SEM images of amorphous Al_2O_3 and SiO_2 particles reacted at 295 K in 6 M NaOH solution for (a,d) 24 h, (b,e) 72 h, and (c,f) 384 h. Reflections indexable to crystalline NaCl and AlO(OH) are indicated with red and blue dots, respectively.

5.4.2 Changes in the local ^1H , ^{23}Na , ^{27}Al , and ^{29}Si environments formed at early reaction times (24-72 h)

The atomic-scale ^1H , ^{29}Si , ^{27}Al , and ^{23}Na environments and interactions in the aluminosilica IPB materials are established by one-dimensional (1D) and two-dimensional (2D) solid-state nuclear magnetic resonance (NMR) spectroscopy, which provides element-specific insights into the chemical environments, covalent bonding configurations, and

nanoscale interactions of the atomic species of interest. For example, the 1D single-pulse ^{27}Al magic-angle-spinning (MAS) NMR spectra of amorphous Al_2O_3 and SiO_2 particles reacted in aqueous 6 M NaOH for 24 and 72 h, shown in **Fig. 5.2**, exhibit different ^{27}Al signals from ^{27}Al species in four- and six-coordinated environments, denoted $^{27}\text{Al}^{\text{IV}}$ and $^{27}\text{Al}^{\text{VI}}$, respectively. After 24 h reaction time, the 1D ^{27}Al MAS NMR spectrum is dominated by a ^{27}Al signal at 9 ppm, which accounts for 99.7% of the total integrated ^{27}Al signal intensity and is assigned to $^{27}\text{Al}^{\text{VI}}$ environments in the Al_2O_3 and $\text{AlO}(\text{OH})$ particles. A weak signal at 55 ppm accounts for 0.3% of the total integrated ^{27}Al signal intensity and is assigned to $^{27}\text{Al}^{\text{IV}}$ environments at the surfaces of the Al_2O_3 particles and within the nascent aluminosilica network. Previously, the formation of $^{27}\text{Al}^{\text{IV}}$ environments in IPB materials has been correlated to the development of macroscopic compressive strength.²⁴ The very small overall quantity of four-coordinated ^{27}Al species detected in the Al_2O_3 and SiO_2 materials reacted for 24 h indicates that only a very small fraction of the total Al in the material has participated in the formation of the aluminosilica network at this early stage. After 72 h reaction, the ^{27}Al signals at 55-60 and 9 ppm are detected from $^{27}\text{Al}^{\text{IV}}$ and $^{27}\text{Al}^{\text{VI}}$ species, respectively. The $^{27}\text{Al}^{\text{IV}}$ species with signals in the 55-60 ppm range account for 3% of the total integrated signal intensity in the 1D ^{27}Al MAS NMR spectrum, while the $^{27}\text{Al}^{\text{VI}}$ species account for 97% of the total integrated signal intensity. The increase in the total quantity of $^{27}\text{Al}^{\text{IV}}$ species from 0.3% after 24 h reaction to 3% after 72 h reaction suggests an order-of-magnitude increase in the quantity of ^{27}Al species incorporated into an aluminosilica network formed after the longer reaction time, though this still comprises a relatively small fraction of the overall ^{27}Al species present in the material.

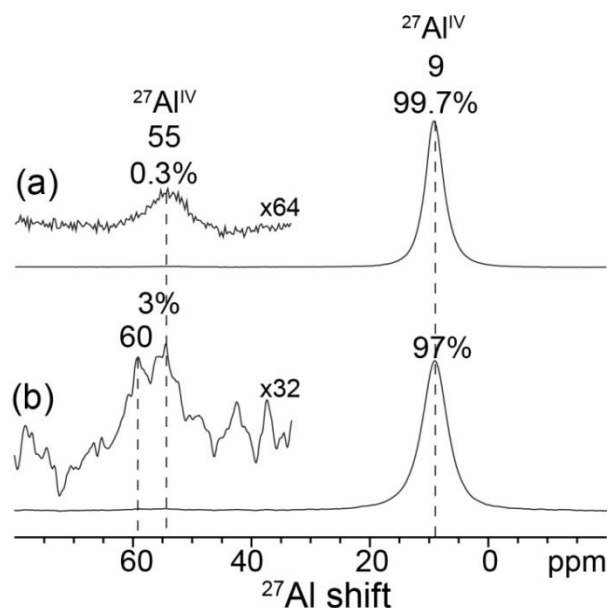


Figure 5.2 Solid-state 1D ^{27}Al MAS NMR spectra of amorphous Al_2O_3 and SiO_2 particles reacted at 295 K in 6 M NaOH solution for (a) 24 h and (b) 72 h. The spectra were acquired at 295 K, 18.8 T, and 20 kHz MAS.

The development of macroscopic strength in IPB materials is expected to arise from molecular-level changes in the compositions and structures of the aluminosilica network that occur gradually over the course of the reaction period.²⁴ However, distinguishing the bonding environments of different ^{27}Al and ^{29}Si species in the aluminosilica networks in IPB materials is exceptionally challenging due in part to their non-stoichiometric compositions, dilute overall quantities (especially for early reaction times), and broad and overlapping NMR signals from different alumina(te) and silica(te) phases of the complex and heterogeneous IPB materials. However, recent advances in solid-state NMR spectroscopy, most notably dynamic-nuclear-polarization surface-enhanced MAS NMR (DNP-SENS) techniques at low temperatures (<100 K), provide significantly enhanced NMR signal sensitivity that enables the detection and correlation of ^{27}Al and ^{29}Si environments in dilute aluminosilica materials, even at natural isotopic abundance (4.7%) ^{29}Si .¹²⁻¹⁵ The DNP-SENS experiments use continuous microwave irradiation at <100 K to transfer high electron spin polarization from

stable exogeneous biradicals such as TEKPol²⁵ via electron-nuclear hyperfine interactions to ¹H nuclei of the frozen 1,1,2,2-tetrachloroethane (TCE) DNP solvent molecules.¹⁶ The hydrophobic solvent TCE is chosen so as to not perturb the structure or hydration environments of ²⁹Si and ²⁷Al species in the aluminosilica network or at particle surfaces.²⁶ The DNP-enhanced ¹H spin polarization is distributed by ¹H-¹H spin diffusion through the frozen solvent to other molecularly proximate (<1 nm) solvent molecules and to the surfaces of the colloidal particles. Subsequently, DNP-enhanced ¹H polarization is transferred via ²⁹Si{¹H}, ²⁷Al{¹H}, or ²³Na{¹H} cross-polarization (CP) to ²⁹Si, ²⁷Al, or ²³Na nuclei. Alternatively, DNP-enhanced polarization of the ²³Na, ²⁷Al, or ²⁹Si nuclei can be detected via direct-excitation methods, which can yield improved sensitivity for quadrupolar nuclei such as ²³Na ($I = 3/2$) and ²⁷Al ($I = 5/2$), particularly under conditions where radical-surface interactions drive DNP polarization transfer. The polarization transfer pathways involved in DNP-NMR experiments are depicted schematically in **Figure 5.3a**.

To demonstrate the dramatic sensitivity enhancements enabled by DNP-SENS measurement conditions, **Figure 5.3b,c** shows the DNP-enhanced 1D ²⁹Si{¹H} and ²⁷Al{¹H} CPMAS spectra of 50 nm colloidal alumina and silica particles reacted for 24 h in 6 M NaOH (water/solids ~ 2). The spectra were acquired under DNP-SENS measurement conditions without (black) and with (red) microwave irradiation. The DNP-SENS signal enhancements ϵ_{Si} and ϵ_{Al} are defined as the ratio of ²⁹Si{¹H} or ²⁷Al{¹H} DNP-CPMAS signal intensities obtained with (red) and without (black) microwave irradiation, and were measured to be $\epsilon_{\text{Si}} = 22$ and $\epsilon_{\text{Al}} = 37$. After 24 h of dissolution and network formation, the ²⁹Si{¹H} DNP-CPMAS spectrum of reacted Al₂O₃ and SiO₂ particles (**Fig. 5.3b**) shows a broad distribution of ²⁹Si signal intensity, with three partially-resolved ²⁹Si signal maxima at -110, -101, and -92 ppm.

These three signals are assigned respectively on the basis of their shift positions²³ to $Q^4(0Al)$ species, overlapping signals from $Q^4(1Al)$ and $Q^3(0Al)$ species, and $Q^3(1Al)$ and $Q^2(0Al)$ species, respectively. The $Q^n(mAl)$ notation refers to a tetrahedral silicon atom which is covalently bonded (through bridging oxygen atoms) to n silicon or aluminum atoms, of which m are aluminum. Q^n species with $n < 4$ are therefore incompletely crosslinked and associated with SiOH and/or $-SiO^-$ species at the surfaces of the SiO_2 particles as well as within the partially-condensed aluminosilica networks. After longer dissolution/network formation times (72 h), the same three broad ^{29}Si signals are observed but shifted by ca. 1 ppm to higher frequency. This small chemical shift displacement is consistent with a greater concentration of silicate species that are partially-crosslinked and/or linked to Al species after the longer reaction time. However, the small magnitude of the displacement indicates that only a relatively small fraction of the total number of ^{29}Si species are influenced by the longer reaction times and correspondingly participating in dissolution, reprecipitation, and network formation. The $^{27}Al\{^1H\}$ DNP-CPMAS spectrum (**Fig. 5.3c**) is dominated by a signal at 8 ppm from six-coordinated ^{27}Al environments at the surfaces of the Al_2O_3 particles, similar to the conventional 1D ^{27}Al MAS NMR spectra in **Fig. 5.2** though the ^{27}Al signals are displaced and somewhat broadened due to field-dependent quadrupolar²⁷ and temperature-dependent²⁸ broadening effects. Additional weak ^{27}Al signals at 50 and 31 ppm are assigned to ^{27}Al species in four- and 5-coordinate environments and arise from relatively dilute ^{27}Al species at the surfaces of the Al_2O_3 particles as well as within the partially-condensed aluminosilica network. However, due to the inhomogeneously-broadened and overlapping ^{27}Al and ^{29}Si signals from the different ^{27}Al and ^{29}Si environments within the amorphous Al_2O_3 and SiO_2 particles, at the particle surfaces, and incorporated into the dilute aluminosilica network, it is

impossible to unambiguously resolve the signals associated with the aluminosilica network on the basis of 1D $^{29}\text{Si}\{^1\text{H}\}$ and $^{27}\text{Al}\{^1\text{H}\}$ DNP-SENS spectra alone.

Crucially, the more than order-of-magnitude enhancement in NMR signal intensity enables the measurement of 2D $^{29}\text{Si}\{^1\text{H}\}$, $^{27}\text{Al}\{^{29}\text{Si}\}$, and $^{23}\text{Na}\{^{29}\text{Si}\}$ heteronuclear correlation spectra of the dilute surface species in aluminosilica networks, which have until now been challenging or infeasible to characterize without expensive isotopic enrichment in ^{29}Si . With DNP-SENS techniques, powerful 2D NMR correlation analyses can be applied to establish the molecular-level structures and compositions of aluminosilica networks, which can be used to correlate directly to the development of macroscopic strength in the materials.

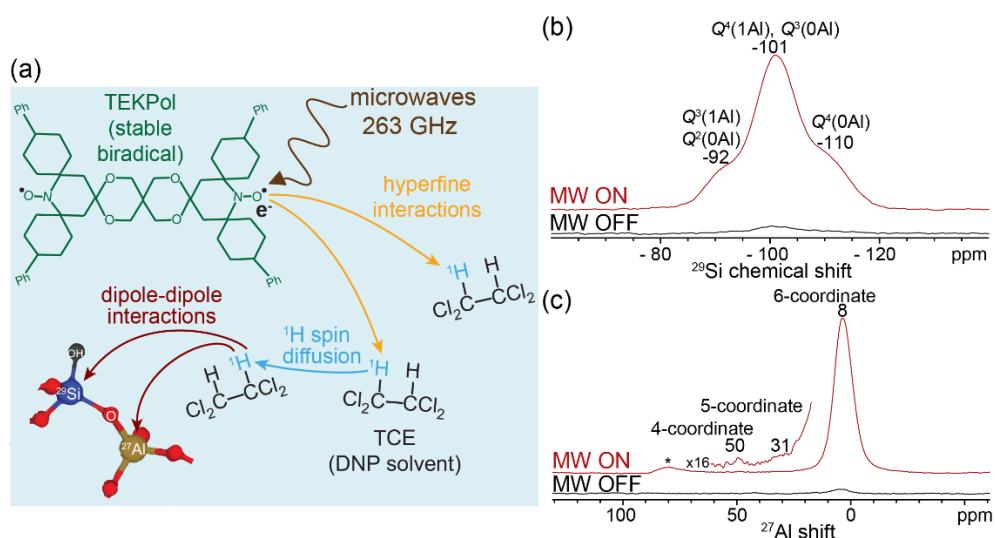


Figure 5.3 (a) Schematic diagram depicting the various polarization transfer pathways involved in the DNP-SENS experiments, including hyperfine interactions (yellow arrows) from electrons on the TEKPol biradical to proximate ^1H nuclei, ^1H spin diffusion within the frozen solvent to the external particle surfaces (blue arrows), followed by $^{29}\text{Si}\{^1\text{H}\}$ cross-polarization (maroon arrows) from ^1H to ^{29}Si nuclei (natural abundance 4.7%, $I = 1/2$) or ^{27}Al nuclei (natural abundance 100%, $I = 5/2$) through nuclear dipole-dipole interactions. Solid-state DNP-SENS 1D (b) $^{29}\text{Si}\{^1\text{H}\}$ and (c) $^{27}\text{Al}\{^1\text{H}\}$ CPMAS spectra of 50 nm colloidal alumina and silica particles reacted for 24 h in 6 M NaOH (water/solids ~ 2), acquired in the presence of 8 mM TEKPOL biradical in frozen 1,1,2,2-tetrachloroethane (TCE), at 9.4 T, 90 K, 8 kHz MAS, and without (black) or with (red) microwave irradiation at 263 GHz.

Specifically, DNP-SENS heteronuclear correlation spectra establish the hydration environments, $^{27}\text{Al-O-}^{29}\text{Si}$ bonding configurations, and the interactions and environments of Na^+ cations in aluminosilica networks formed by reaction of Al_2O_3 and SiO_2 particles in highly alkaline conditions after different reaction times. These insights are provided by two-dimensional (2D) $^{29}\text{Si}\{^1\text{H}\}$, $^{27}\text{Al}\{^{29}\text{Si}\}$, and $^{23}\text{Na}\{^{29}\text{Si}\}$ DNP-SENS heteronuclear correlation spectra, which are mediated by through-space internuclear dipole-dipole couplings that operate over distances of < 1 nm. The 2D spectra are plotted as 2D contour plots with ^1H , ^{29}Si , ^{27}Al , or ^{23}Na frequency axes plotted with units of Hz/MHz or ppm. Correlated signals in the 2D spectra manifest the site-specific interactions and nanoscale proximities of the dipole-dipole coupled ^1H , ^{29}Si , ^{27}Al , or ^{23}Na nuclei with the corresponding NMR signals. The 2D DNP-SENS spectra thus selectively detect and resolve signals from dilute species within the aluminosilica networks, including directly-bonded $^{27}\text{Al-O-}^{29}\text{Si}$ moieties and charge-balancing Na^+ cations situated near AlO_4^- tetrahedral within the IPB networks.

Strong hydrogen-bonding interactions of adsorbed water at the surfaces of the SiO_2 particles and within the aluminosilica networks are established by the 2D $^{29}\text{Si}\{^1\text{H}\}$ DNP-SENS HETeronuclear CORrelation (HETCOR) spectra in **Figure 5.4**. The 2D $^{29}\text{Si}\{^1\text{H}\}$ spectrum of the particle mixture after 24 h of reaction in 6 M NaOH shows broad, overlapping ^{29}Si signals at -92, -100, and -108 ppm, which reflect overlapping signal contributions from $Q^3(1\text{Al})/Q^2(0\text{Al})$, $Q^4(1\text{Al})/Q^3(0\text{Al})$, and $Q^4(0\text{Al})$ silicate species, respectively. All of these signals are correlated with a broad distribution ^1H signals from 5.2 to 20 ppm, which arise from -OH moieties participating to different extents in hydrogen bonding at the different ^{29}Si sites. The ^1H signals at 5.2 ppm are consistent with physisorbed water, while the signals at higher ^1H chemical shift values arise from strongly H-bonded -OH moieties which are

associated with incompletely condensed Si-OH, Al-OH, and H₂O species at particle surfaces and in the crosslinking aluminosilica network. Well-established semi-empirical correlations relate the ¹H chemical shift to the -OH...O- hydrogen bond distances.²⁹ Using these correlations, the broad ¹H signals from 6-20 ppm establish the presence of very strong hydrogen bonding interactions at partially and completely crosslinked silicate sites at the surfaces of the SiO₂ particles and the aluminosilica networks. The ²⁹Si signal at -100 ppm from Q³(0Al) and Q⁴(1Al) silicate species shows an additional weak intensity correlation with the ¹H signal at 2.5 ppm, which is assigned to dilute isolated Si-OH moieties associated with Q³(0Al) sites at the surfaces of the SiO₂ particles. The 2D DNP-SENS ²⁹Si{¹H} HETCOR spectrum of the same material after 72 h reaction shows similar ²⁹Si-¹H intensity correlations between ²⁹Si signals at -92, -100, and -106 ppm and ¹H signals at 5.7 ppm from adsorbed water, and 8.7-15 ppm from strongly H-bonded -OH groups. The decrease in the shifted H-bonded -OH groups indicates a decrease in the interaction between adsorbed water and the partially and completely crosslinked silicate sites at the surface. Previous analyses of cementitious IPB materials, and traditional cement materials, has suggested that strength development coincides with expulsion of water from the IPB as the material condenses. The reduced extent of hydrogen bonding detected after 72 h reaction compared to 24 h is consistent with exclusion of water from between the SiO₂ particles and from within the aluminosilica network during condensation of the material. Complementary analyses of 2D DNP-SENS ²⁷Al{¹H} HETCOR spectra of the same materials corroborate this conclusion. All ²⁹Si signals in the 2D ²⁹Si{¹H} HETCOR spectrum in **Fig. 5.4b** are also correlated with ¹H signals at 2.0 and -0.5 ppm, which are assigned to isolated -Si-OH and Na-OH moieties, respectively. The stronger correlated signal intensities from isolated -Si-OH species after 72 h reaction

compared to 24 h suggests that longer reaction times lead to greater densities of relatively isolated (as opposed to strongly H-bonded) hydroxyl groups, which is also consistent with the reduced extent of hydrogen bonding for the material reacted for 72 h. Furthermore, the correlated signals from Na-OH species establish that a subset of the alkaline NaOH species present in the reaction media are adsorbed (within 1 nm) at the surfaces of the partially-crosslinked SiO₂ particles. This conclusion is corroborated by the 2D DNP-SENS ²³Na{²⁹Si} correlation spectra discussed below.

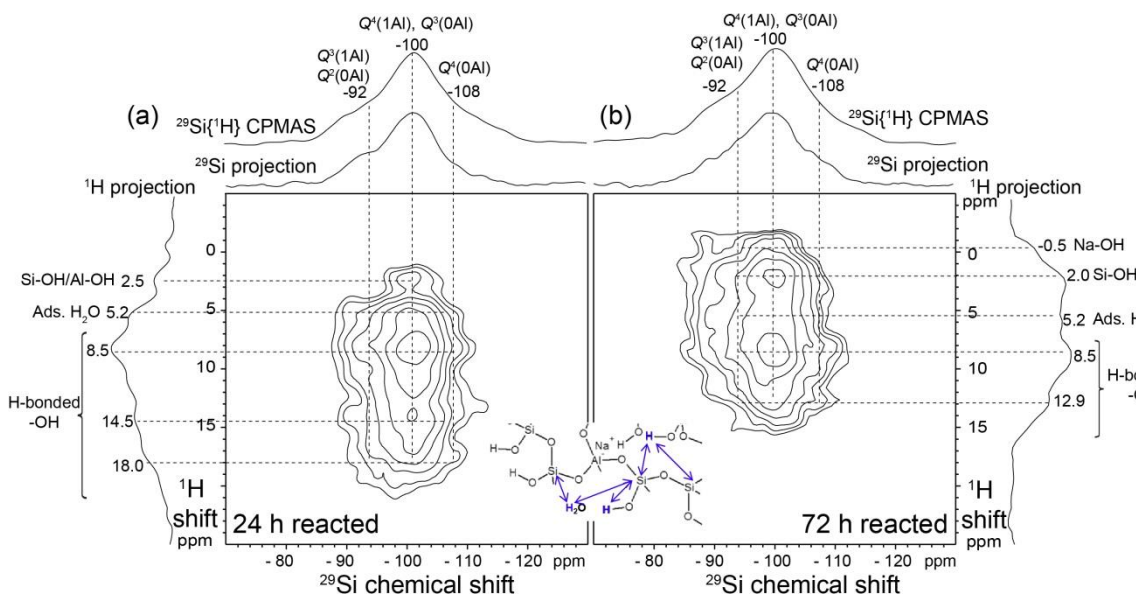


Figure 5.4 Solid-state 2D ²⁹Si{¹H} DNP-CP-HETCOR spectra of amorphous Al₂O₃ and SiO₂ particles reacted at 295 K in 6 M NaOH solution for (a) 24 h and (b) 72 h. The spectra were acquired at 95 K, 9.4 T, 8 kHz MAS, in the presence of 8 mM TEKPol biradical polarizing agent in 1,1,2,2-tetrachloroethane (DNP solvent), and using ²⁹Si{¹H} CP contact times of 0.5 ms. Solid-state 1D ²⁹Si{¹H} DNP-CPMAS spectra are shown along the horizontal axes for comparison with the 1D ²⁹Si projections of the 2D spectra, and the ¹H projections are shown along the vertical axes. The inset shows interactions of hydroxyl moieties and occluded water molecules with ²⁹Si atoms in the aluminosilica network.

The ²⁷Al-O-²⁹Si covalent connectivities within the precipitated aluminosilica IPB network are different after different reaction times, as established by the 2D ²⁷Al{²⁹Si} dipolar-

mediated heteronuclear multi-quantum coherence (*D*-HMQC) NMR spectra of colloidal Al₂O₃ and SiO₂ particles reacted in 6 M NaOH for 24 or 72 h shown in **Fig. 5.5**. The 2D ²⁷Al{²⁹Si} HMQC spectra selectively detect and correlate ²⁷Al species that are dipole-dipole-coupled to, and within nanoscale proximity of, ²⁹Si nuclei, being principally sensitive to interactions of directly-bonded ²⁷Al-O-²⁹Si spin pairs. The 2D spectra thus establish unambiguously the types, distributions, and covalent bonding of ²⁹Si and ²⁷Al species within the aluminosilica networks, which comprise only ca. 1-3% of the IPB materials based on the quantitative ²⁷Al single-pulse spectra discussed above. The 2D ²⁹Si{²⁷Al} HMQC spectrum of the Al₂O₃ and SiO₂ particles after 24 h reaction (**Fig. 5.5a**) shows broad partially-resolved ²⁷Al signals at 65 and 48 ppm that arise from ²⁷Al^{IV} and ²⁷Al^V species, respectively. The ²⁷Al signal at 48 ppm is correlated to a broad distribution of ²⁹Si signals in the -96 to -85 ppm range, indicating that ²⁷Al^V species in the aluminosilica network are bonded (through bridging oxygen atoms) to partially-crosslinked *Q*³(1Al) and *Q*²(1Al) silicate species. Interestingly, the ²⁷Al signal at 65 ppm is correlated to ²⁹Si signals centered at -85 ppm from *Q*²(1Al) species, indicating that the ²⁷Al^{IV} species are predominately bonded to *Q*²(1Al) silicate species and distributed in regions of the aluminosilica network that are less-completely crosslinked than the environments occupied by ²⁷Al^V species.

At longer reaction times, the aluminosilica network condenses further, evidenced by the correlated signal intensities in the 2D ²⁷Al{²⁹Si} *D*-HMQC spectrum of Al₂O₃ and SiO₂ particles reacted in 6 M NaOH for 72 h shown in **Figure 5.4b**. The spectrum shows ²⁷Al signals at 62 and 40 ppm from ²⁷Al^{IV} species that are correlated to a relatively narrow ²⁹Si signal at -94 ppm from *Q*³(1Al) silicate species. These correlated signals establish the ²⁷Al-O-²⁹Si connectivities of four- and five-coordinated ²⁷Al species and *Q*³(1Al) silicate species

within the partially-condensed aluminosilica network. Overall, the DNP-enhanced 2D $^{27}\text{Al}\{^{29}\text{Si}\}$ D -HMQC spectra and analyses establish that at early reaction times of 24 h, the aluminosilica network is composed of ^{27}Al species in four- and five-coordinate environments that are connected to partially-crosslinked Q^2 and Q^3 silicate species. After longer reaction times of 72 h, Q^2 silicate species further condense to form $Q^3(1\text{Al})$ species.

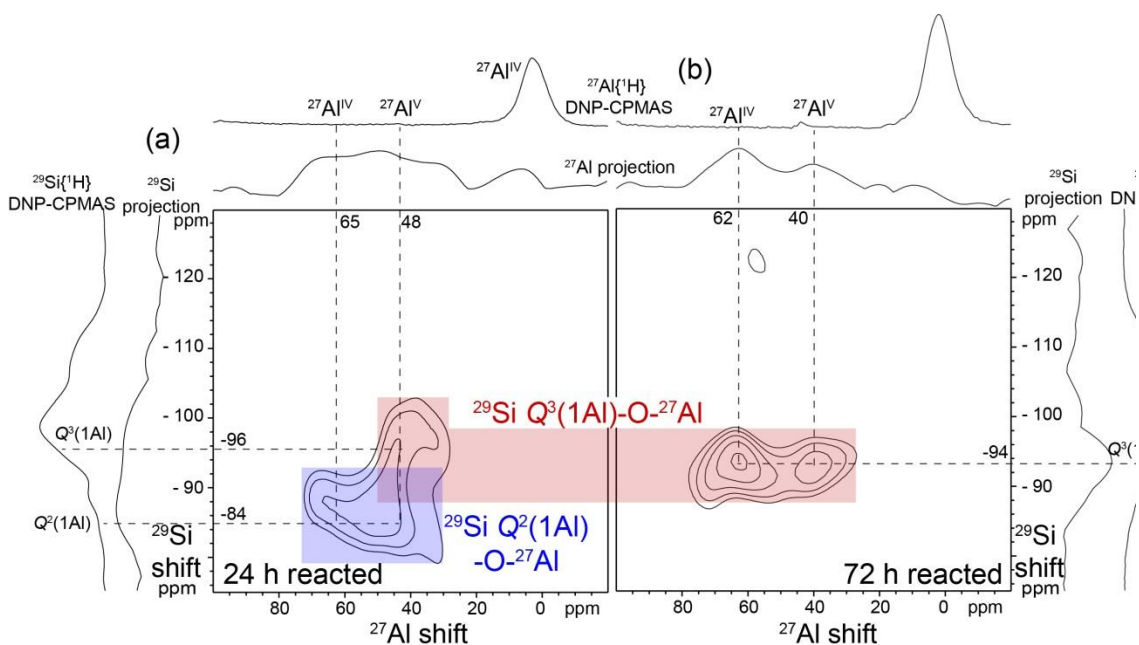


Figure 5.5 Solid-state 2D $^{27}\text{Al}\{^{29}\text{Si}\}$ DNP- D -HMQC spectra of amorphous Al_2O_3 and SiO_2 particles reacted at 295 K in 6 M NaOH solution for (a) 24 h and (b) 72 h. The spectra were acquired at 95 K, 9.4 T, 8 kHz MAS, and in the presence of 8 mM TEKPol biradical polarizing agent in 1,1,2,2-tetrachloroethane (DNP solvent). Solid-state 1D $^{27}\text{Al}\{^1\text{H}\}$ or $^{29}\text{Si}\{^1\text{H}\}$ DNP-CPMAS spectra are shown along the horizontal axes for comparison with the 1D projections of the 2D spectra.

Sodium cations have long been recognized to play roles as activator species in the dissolution and setting of silica-based cementitious materials due to the empirically-observed catalytic influence that sodium plays on the dissolution of silica.² Highly alkaline conditions are generally required for the formation of IPBs due to the reduced dissolution rates which greatly slow the setting time compared to traditional cements, though it has not been clear if

the sodium ions play a more active role in directing the formation of the resultant aluminosilica(te) structure compared to other metal cations. Solid-state DNP-enhanced 1D ^{23}Na echo and $^{23}\text{Na}\{^1\text{H}\}$ CPMAS establish the local environments of Na^+ cations in colloidal Al_2O_3 and SiO_2 particles reacted in 6 M NaOH for 24 and 72 h, as shown in **Figure 5.6**. Specifically, the 1D ^{23}Na echo spectra of the materials reacted for 24 (**Fig. 5.6a**) and 72 h (**Fig. 5.6b**) show a relatively narrow (2 ppm full-width-half-maximum, FWHM) ^{23}Na signal at 7 ppm that arises from the NaCl phase formed on neutralization of the materials with HCl. An additional ^{23}Na signal at -2 ppm is much broader and exhibits a Czjzek quadrupolar lineshape,³⁰ as established by the representative deconvolution of the spectrum in Fig. 6a. The Czjzek lineshape is characteristic of a distribution of quadrupolar parameters corresponding to isotropically distributed ^{23}Na species, typically seen in glasses. The -2 ppm shift position of the broad ^{23}Na signal is similar to ^{23}Na signals seen in Na^+ -exchanged zeolites,³¹ and the signal is assigned to hydrated Na^+ cations interacting at the surfaces of the Al_2O_3 and SiO_2 particles, as well as incorporated within the aluminosilica network. Only the broad ^{23}Na signal at -2 ppm is enhanced in the 1D $^{23}\text{Na}\{^1\text{H}\}$ DNP-CPMAS spectra in Fig. 6c,d, corroborating that this signal corresponds to hydrated Na^+ cations while the ^{23}Na signal at 7 ppm arises from anhydrous NaCl species. While the 1D ^{23}Na echo spectra in **Fig. 5.6a,b** are not strictly quantitative, the relative signal intensity of the ^{23}Na signal from NaCl decreases after 72 h reaction time relative to after only 24 h, indicating that more Na^+ cations are incorporated into the aluminosilica network at later reaction times, consuming NaOH species that otherwise form NaCl on acid neutralization of the materials.

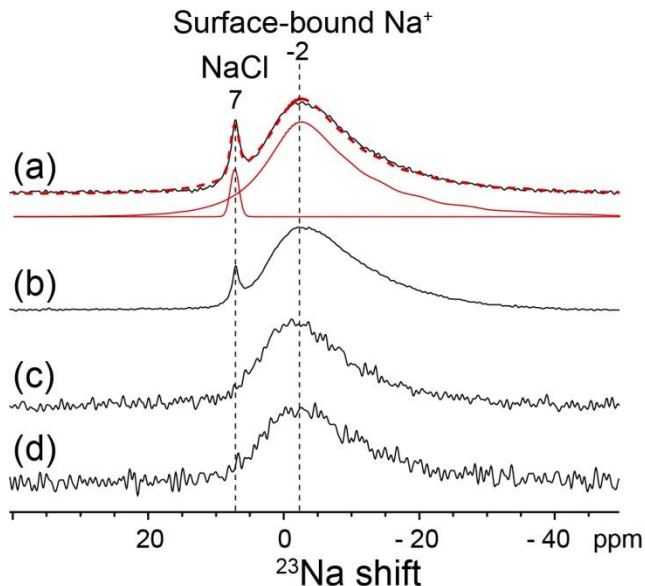


Figure 5.6 Solid-state 1D DNP-enhanced (a,b) ^{23}Na echo and (c,d) $^{23}\text{Na}\{^1\text{H}\}$ CPMAS NMR spectra of amorphous Al_2O_3 and SiO_2 particles reacted at 298 K in 6 M NaOH solution for (a,c) 24 h and (b,d) 72 h. The spectra were acquired at 95 K, 9.4 T, 8 kHz MAS, in the presence of 8 mM TEKPol biradical polarizing agent in 1,1,2,2-tetrachloroethane (DNP solvent), and using $^{23}\text{Na}\{^1\text{H}\}$ CP contact times of 5 ms for (c,d). A representative simulation of the ^{23}Na spectra is shown in (a) as the dotted red line, with the fit deconvolution shown offset below.

Interestingly, Na^+ cations interact to significant extents at the surfaces of the SiO_2 particles, as established by the DNP-enhanced 2D $^{23}\text{Na}\{^{29}\text{Si}\}$ *D*-HMQC spectra in **Figure 5.7**. The 2D $^{23}\text{Na}\{^{29}\text{Si}\}$ NMR correlation spectrum of amorphous Al_2O_3 and SiO_2 particles reacted for 24 h in 6 M NaOH (**Fig. 5.7a**) reveals correlated signal intensities at -6 and -2 ppm in the ^{23}Na dimension and -84 and -94 ppm in the ^{29}Si dimension (red shaded region), which arise from Na^+ cations near $Q^2(\text{1Al})$ and $Q^3(\text{1Al})$ moieties. These signals are assigned to Na^+ cations that charge-balance the AlO_4^- tetrahedra that compose part of the aluminosilica network as established by the 2D $^{27}\text{Al}\{^{29}\text{Si}\}$ *D*-HMQC analyses discussed above. Interestingly, the 2D $^{23}\text{Na}\{^{29}\text{Si}\}$ correlation spectrum shows an additional broad distribution of correlated signal intensity from 5 to -15 in the ^{23}Na dimension and -123 to -94 ppm in the ^{29}Si dimension, as well as a narrow, correlated signal intensity at -21 ppm in the ^{23}Na dimension and -109 ppm

in the ^{29}Si (yellow-shaded region). These signals establish the nanoscale interactions of hydrated Na^+ cations and ^{29}Si $Q^4(0\text{Al})$, $Q^4(1\text{Al})$, $Q^3(0\text{Al})$, and $Q^4(1\text{Al})$ silicate species at the surfaces of the partially-reacted SiO_2 particles. After 72 h reaction (**Fig. 5.7b**), similar but somewhat broader correlated $^{23}\text{Na}\{^{29}\text{Si}\}$ signal intensities are observed at 10 to -22 ppm in the ^{23}Na dimension and -128 to -94 ppm in the ^{29}Si dimension, indicating broader distributions of surface-bound $^{23}\text{Na}^+$ at the SiO_2 particle surfaces after the longer reaction time. An additional weaker signal at -2 ppm in the ^{23}Na dimension and -94 ppm in the ^{29}Si dimension (red shaded region) is assigned to Na^+ species that charge balance AlO_4^- tetrahedra near $Q^3(1\text{Al})$ sites within the partially-condensed aluminosilica network. Interestingly, this signal is narrower than the similar signal in the same spectral region of the spectrum acquired after 24 h reaction time (**Fig. 5.7a**), indicating that the extent of local order of the Na^+ cations incorporated within the aluminosilica network increases as a function of reaction time. Given the strong correlated signal intensities in the spectral region associated with surface-bound Na^+ cations, a substantial fraction of the Na^+ species in the material interact electrostatically with Si-O^- moieties at the surfaces of the partially-reacted SiO_2 particles after both 24 and 72 h reaction. The strong surface interactions of Na^+ cations and the SiO_2 particle surfaces is evidence of the important catalytic role sodium ions play at the silica surface, though the extent at which they interact on a molecular level has not been well characterized to date. These correlated 2D NMR measurements provide an opportunity to see how sodium ions interact at the silica surface during network formation. Complementary 1D and 2D $^{27}\text{Al}\{^{23}\text{Na}\}$ NMR correlation experiments are currently in progress to corroborate the incorporation of Na^+ cations into the aluminosilica network and also evaluate the extents and types of interactions of Na^+ cations with the Al_2O_3 particles.

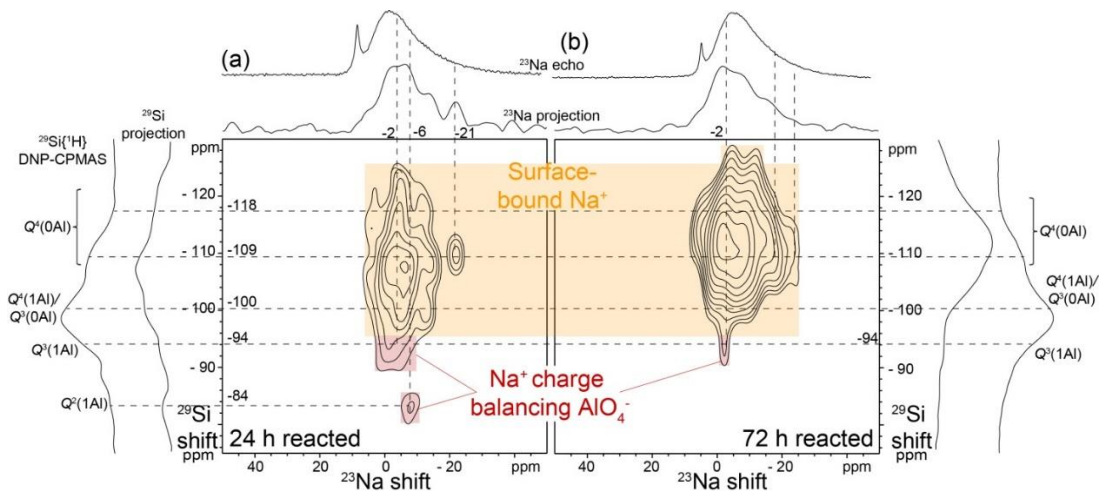


Figure 5.7 Solid-state 2D $^{23}\text{Na}\{^{29}\text{Si}\}$ DNP-*D*-HMQC spectrum of amorphous Al_2O_3 and SiO_2 particles reacted at 298 K in 6 M NaOH solution for (a) 24 h and (b) 72 h. The spectra were acquired at 95 K, 9.4 T, 8 kHz MAS, and in the presence of 8 mM TEKPol biradical polarizing agent in 1,1,2,2-tetrachloroethane (DNP solvent). Solid-state 1D ^{23}Na echo or $^{29}\text{Si}\{^1\text{H}\}$ DNP-CPMAS spectra are shown along the horizontal axes for comparison with the 1D projections of the 2D spectra.

The comprehensive 1D and 2D $^{27}\text{Al}\{^1\text{H}\}$, $^{29}\text{Si}\{^1\text{H}\}$, $^{27}\text{Al}\{^{29}\text{Si}\}$, $^{23}\text{Na}\{^1\text{H}\}$, and $^{23}\text{Na}\{^{29}\text{Si}\}$ DNP-SENS spectra and analyses together provide detailed information on the compositions and structures of the surface species in alkali-activated aluminosilica cements and their evolution over time. A schematic diagram of the types and distributions of surface ^{23}Na , ^{27}Al , and ^{29}Si species that compose the aluminosilica network is shown in **Figure 5.8** that is consistent with all of the solid-state NMR analyses. Specifically, the aqueous 6 M NaOH reaction mixture equilibrates rapidly as solution-phase species saturate. Less than 3% of all of the aluminum atoms present in the material are incorporated into the aluminosilica network formed after 24-72 h. Nevertheless, the structure and composition of the aluminosilica IPB network change dramatically over that same time period. Water is excluded from the interparticle networks as silicate species in the aluminosilica network condense. After 24 h reaction time, the aluminosilica network is composed of four- and five-coordinate ^{27}Al species

bonded (through bridging oxygen atoms) to partially-crosslinked $Q^3(1Al)$ and $Q^2(1Al)$ silicate species. After 72 h reaction time, the types of ^{27}Al coordination environments are unchanged though the majority of ^{27}Al species are bonded to $Q^3(1Al)$ species, consistent with further condensation of the IPB network over longer reaction times. Additionally, Na^+ species are incorporated into the aluminosilica network after reaction times of 24-72 h, likely acting as charge-balancing cations to AlO_4^- tetrahedral. Broad distributions of Na^+ species are shown to interact with the surfaces of the partially-reacted SiO_2 particles, related to the previously observed catalytic effect on silica dissolution.

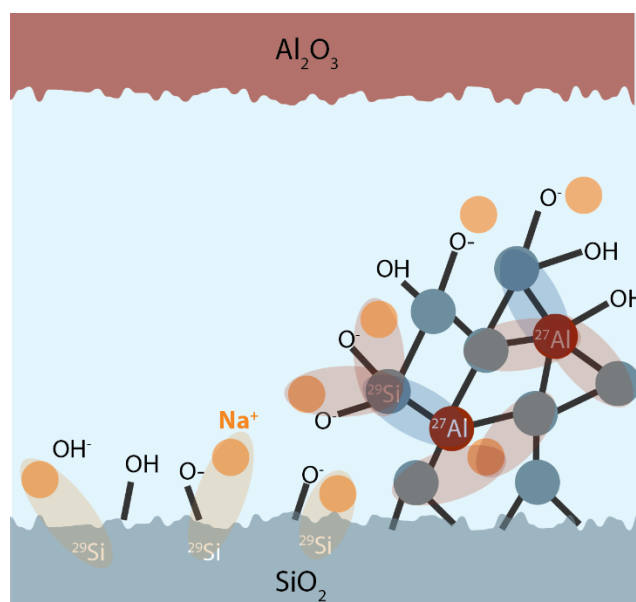


Figure 5.8 Schematic diagram of the partially-condensed aluminosilica network formed on reaction of colloidal alumina and silica particles in aqueous 6 M NaOH. Silicon, aluminum, and sodium atoms are represented by blue, red, and yellow circles, respectively, and the ^{27}Al - ^{29}Si and ^{23}Na - ^{29}Si interactions manifested by the 2D $^{27}Al\{^{29}Si\}$ and $^{23}Na\{^{29}Si\}$ DNP- D -HMQC spectra in Fig. 5.5 and 5.6 are represented by the blue, red, or yellow colored regions.

5.4.3 Characterizing early dissolution behavior of aluminosilica network formation

In addition to characterizing the local molecular structure during the initial stages of aluminosilica network formation, the SFA apparatus was used to establish the early

dissolution behavior for an asymmetric solid-liquid-solid interface of alumina and silica in 6 M NaOH. The previous NMR results clearly indicate that the dissolution and subsequent network formation reactions primarily occur at the surface, with large amounts of the bulk material remaining inactive in the network formation process. Force-distance $F(D)$ measurements were performed using a standard Surface Forces Apparatus 2000 (SFA),³² depicted in **Figure 1.2**.

The SFA experiments were set up with two composite surfaces, one with an 800 nm thick SiO₂ layer and one with 10 nm Al₂O₃ layer on 800 nm SiO₂. 6 M NaOH was injected between the surfaces with a water/solids ratio of 200 to cover the entire contact area. Forces were measured on approach rates below which hydrodynamic forces are negligible, as ascertained by forces that are independent of approach rates. Representative force-distance profiles, $F(D)$, measured while bringing together the two silica and alumina-coated silica surfaces are shown by the data points in **Figure 5.9**.

At the first force measurement after injection, where the surfaces have been exposed to the solution for approximately 10 minutes, we observe significant dissolution of the surfaces by approximately 15 nm. This is clearly observed by the difference in the hardwall of the t_0 curve and the initial contact marker and is expected for silica and alumina-coated silica surfaces in a strong alkaline solution. As the reaction time increases, the hardwall of the surfaces continues to shift indicating dissolution is still occurring at the $t > 1$ h curve. Due to the increase in water/solids ratio, the solution will remain undersaturated with regards to silica and alumina species and no significant growth of aluminosilica species is observed, verified by the lack of adhesion/cohesion even after 168 h.

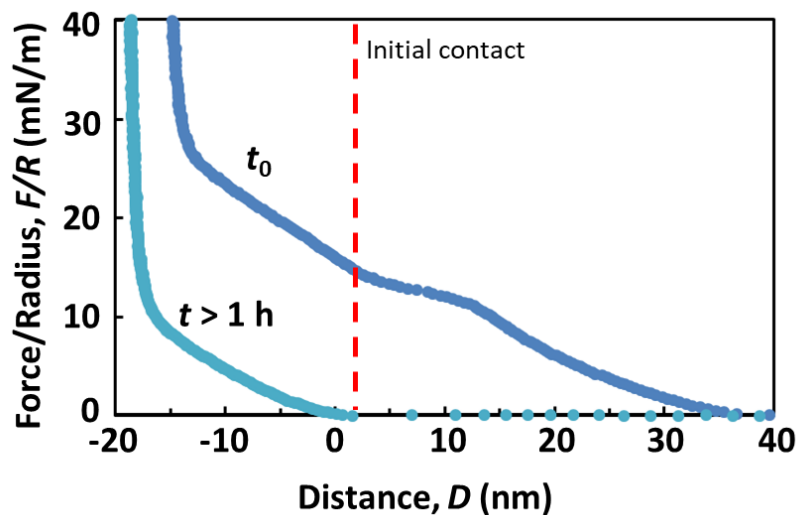


Figure 5.9 Representative force-distance profiles measured between silica and alumina surfaces in 6 M NaOH (pH > 14) at $T = 22^\circ\text{C}$. The water/solids ratio of this experiment was approximately 200 to achieve a large enough volume to coat the entire surface. The curve at t_0 indicates the first force run acquired immediately after injection of the 6 M NaOH solution, which means the surfaces were exposed to solution for up to 10 minutes before data was collected. The curve at $t > t_0$ is representative of the force curve after the surfaces were exposed to solution for more than 1 hour. The initial contact position of the surfaces is indicated by the vertical dashed line.

Notably, a strong repulsion occurs at over 45 nm away from the surface for t_0 and over 20 nm away from the surface for $t > 1$ h. The high salt concentration results in a Debye length that is essentially the size of the counterion which means the electrostatic forces are extremely short-range in this system.³³ The repulsion is instead a result of strongly adsorbed ions near the surface which are compressed as the surfaces are brought together. During the initial approach, we displace an ion layer at 12.3 mN/m with a size of almost 8 nm. These results suggest that, at early dissolution time periods, the silica and alumina species are removed from the surface but still interact strongly near the interface and react to form larger aluminosilica networks (i.e., undergoing the initial stages of nucleation). At longer reaction times, $t > 1$ h, the repulsive interaction regime decreased and no large species were displaced near the

surface, due to the large reservoir of undersaturated solution which allows for diffusion of species away from the confined interface.

5.5 Summary and conclusions

The local atomic environments and distributions of ^1H , ^{23}Na , ^{27}Al , and ^{29}Si species in aluminosilica IPB materials have been established for colloidal SiO_2 and Al_2O_3 particles reacted in highly alkaline (6 M NaOH) aqueous media by using state-of-the-art 1D and 2D DNP-enhanced solid-state NMR techniques, with complementary X-ray diffraction and electron microscopy analyses. The results establish the covalent bonding configurations and hydration environments within the aluminosilica IPB network that evolve over time, which can be related to the development of the macroscopic strength of the material in future experiments. The aluminosilica network forms from reaction of surface and near-surface species and incorporates <3% of all of the ^{27}Al species in the bulk material after reaction times of 24-72 h. After 24-72 hours of reaction time, the aluminosilica network is comprised of four- and five-coordinate ^{27}Al species bonded to partially-crosslinked silicate species that condense over time.

Additionally, the initial stages of dissolution at the interface of alumina and silica surfaces was characterized in highly alkaline (6 M NaOH) aqueous media using SFA force measurement techniques. Significant dissolution is observed followed by the formation of strongly adsorbed surface species which, at early times, have a length of around 8 nm. These results show that during the initial dissolution of the alumina and silica surfaces in a confined interface, the ionic species exist near the surfaces even in highly undersaturated environments, corroborating the observations made using NMR. Further investigation of the initial dissolution behavior followed by nucleation and growth of the aluminosilica network is

required to fully correlate the change in macroscopic properties with the observed molecular structure changes observed using NMR.

The gradual condensation of the aluminosilica network at and between the Al_2O_3 and SiO_2 particle surfaces corresponds with “setting” of the bulk cement material. Understanding the molecular level changes during IPB network formation identifies important factors that may strongly impact the formation of a 4-coordinate aluminosilica network, specifically the presence of impurities that substitute aluminum sites or that competitively react with aluminum to prevent the aluminosilica formation, which is expected to assist in screening of initial precursor (fly ash) selection in the development of new IPB materials with applications as low- CO_2 cements. Fully correlating these results with macroscopic changes in dissolution behavior and network adhesion/cohesion in the SFA provides the basis for spanning molecular-to-macroscopic property relation.

References

1. Shailaja, J. et al. Alkali Ion-controlled excited-state ordering of acetophenones included in zeolites: emission, solid-state NMR, and computational studies. *J. Phys Chem. A.*, **2003**, 107, 3187
2. Duxson, P. et al. Geopolymer technology: the current state of the art. *J. Mater. Sci.*, **2007**, 42, 2917
3. Sherman, J. Synthetic zeolites and other microporous oxide molecular sieves. *Proc. Natl. Acad. Sci.*, **1999**, 96, 3471
4. Khale, D.; Chaudhary, R. Mechanism of geopolymerization and factors influencing its development: a review. *J. Mater. Sci.*, **2007**, 42, 729

5. Na, K.; Jo, C.; Kim, J.; Cho, K.; Jung, J.; Seo, Y.; Messinger, R.; Chmelka, B.; Ryoo, R. Directing zeolite structures into hierarchically nanoporous architectures. *Science*, **2011**, 333, 328
6. Erdem, E.; Karapinar, N.; Donat, R. The removal of heavy metal cations by natural zeolites. *Journal of Colloid and Interface Science*, **2004**, 280, 309
7. Mandal, S.; Roy, D.; Chaudhari, R.; Sastry, M. Pt and Pd nanoparticles immobilized on amine-functionalized zeolite: excellent catalysts for hydrogenation and heck reactions. *Chem. Mater.*, **2004**, 16, 3714
8. Aughenbaugh, K.; Williamson, T.; Juenger, M. Critical evaluation of strength prediction methods for alkali-activated fly ash. *Materials and Structures*, **2015**, 48, 607
9. Duxson, P.; Provis, J.; Lukey, G.; Mallicoat, S.; Kriven, W.; van Deventer, J. Understanding the relationship between geopolymer composition, microstructure and mechanical properties. *Colloids Surfaces A Physicochem. Eng. Asp.*, **2005**, 269, 47
10. Grand, J.; Awala, H.; Mintova, S. Mechanism of zeolites crystal growth: new findings and open questions. *Cryst. Eng. Comm.*, **2016**, 18, 650
11. Thompson, R. *Synthesis Molecular Sieves*, Springer, 1998, vol. 1, p. 1
12. Becerra, L.; Gerfen, G.; Temkin, R.; Singel, D.; Griffin, R. Dynamic nuclear polarization with a cyclotron resonance maser at 5 T. *Phys. Rev. Lett.*, **1993**, 71, 3561
13. Lafon, O.; Thankamony, A.; Kobayashi, T.; Carnevale, D.; Vitzthum, V.; Slowing, I.; Kandel, K.; Vezin, H.; Amoureux, J.; Bodenhausen, G.; Pruski, M. Mesoporous silica nanoparticles loaded with surfactant: low temperature magic angle spinning ^{13}C and ^{29}Si NMR enhanced by dynamic nuclear polarization. *J. Phys. Chem. C*, **2013**, 117, 1375

14. Vitzthum, V.; Mieville, P.; Carnevale, D.; Caporini, M.; Gajan, D.; Coperet, C.; Lelli, M.; Zagdoun, A.; Rossini, A.; Lesage, A.; Emsley, L.; Bodenhausen, G. Dynamic nuclear polarization of quadrupolar nuclei using cross polarization from protons: surface-enhance aluminium-27 NMR. *Chem. Commun.*, **2012**, 48, 1988
15. Lange, S.; Linden, A.; Akbey, U.; Franks, W.; Loening, N.; van Rossum, B.; Oschkinat, H. The effect of biradical concentration on the performance of DNP-MAS-NMR. *J. Mag. Res.*, **2012**, 216, 209
16. Zagdoun, A.; Casano, G.; Ouari, O.; Schwarzwald, M.; Rossini, A.; Aussenac, F.; Yulikov, M.; Jeschke, G.; Coperet, C.; Lesage, A.; Tordo, P.; Emsley, L. Large molecular weight nitroxide biradicals providing efficient dynamic nuclear polarization at temperatures up to 200 K. *J. Am. Chem. Soc.*, **2013**, 135, 12790
17. B. M. Fung, A. K. Khitrin, K. Ermolaev, *Journal of Magnetic Resonance* **2000**, *142*, 97-101.
18. R. P. Sangodkar, B. J. Smith, D. Gajan, A. J. Rossini, L. R. Roberts, G. P. Funkhouser, A. Lesage, L. Emsley, B. F. Chmelka, *Journal of the American Chemical Society* **2015**, *137*, 8096-8112.
19. L. Martel, S. Cadars, E. Veron, D. Massiot, M. Deschamps, *Solid State Nuclear Magnetic Resonance* **2012**, *45-46*, 1-10.
20. B. Hu, J. Trebosc, J. P. Amoureux, *Journal of Magnetic Resonance* **2008**, *192*, 112-122.
21. D. Iuga, H. Schafer, R. Verhagen, A. P. M. Kentgens, *Journal of Magnetic Resonance* **2000**, *147*, 192-209.

22. S. Guha, J. Yang, D.L. Williamson, Y. Lubianiker, J.D. Cohen, A.H. Mahan (1999) Structural, defect, and device behavior of hydrogenated amorphous Si near and above the onset of microcrystallinity. *Appl. Phys. Lett.* 74:1860
23. Y. Nie, M. Xia, F. Niu, S. Liu (2011) ^{29}Si and ^{27}Al MAS-NMR studies of fly ash changes during the polymerization of mineral polymer. *Advanced Materials Research* 156-157:794-798
24. A. Fernandez-Jimenez, A. Palomo, I. Sobrados, J. Sanz (2006) The role played by the reactive alumina content in the alkaline activation of fly ashes. *Micro. and Meso. Mat.* 91:111-119
25. A. Zagdoun, G. Casano, O. Ouari, M. Schwarzwälder, A.J. Rossini, F. Aussenac, M. Yulikov, G. Jeschke, C. Copéret, A. Lesage, P. Tordo, L. Emsley. (2013) Large Molecular Weight Nitroxide Biradicals Providing Efficient Dynamic Nuclear Polarization at Temperatures up to 200 K. *J. Am. Chem. Soc.* 135(34):12790–12797
26. R.P. Sangodkar, B.J. Smith, D. Gajan, A. Rossini, L.R. Roberts, G.P. Funkhouser, A. Lesage, L. Emsley, B.F. Chmelka, (2015) “Influences of dilute organic adsorbates on the hydration of low-surface-area silicates,” *J. Amer. Chem. Soc.*, 137, 8096-8112
27. C.A. Fyfe, J.L. Bretherton, L.Y. Lam (2001) Solid-state NMR detection, characterization, and quantification of the multiple aluminum environments in US-Y catalysts by (^{27}Al) MAS and MQMAS at very high field. *J. Am. Chem. Soc.* 123(22):5285-91
28. S. Cadars, N. Mifsud, A. Lesage, J.D. Epping, N. Hedin, B.F. Chmelka, L. Emsley (2008) Dynamics and Disorder in Surfactant-Templated Silicate Layers Studied by Solid-State NMR Dephasing Times and Correlated Line Shapes. *J. Phys. Chem. C* 112:9145-9154
29. J.P. Yesinowski, H. Eckert, G.R. Rossman (1988) Characterization of hydrous species in minerals by high-speed proton MAS-NMR. *J. Am. Chem. Soc.* 110(5):1367-1375

30. Massiot, D., Fayon, F., Capron, M., King, I., Le Calvé, S., Alonso, B., Durand, J., Bujoli, B., Gan, Z., Hoatson, G. (2002) Modelling one- and two-dimensional solid-state NMR spectra. *Magn. Reson. Chem.* 40: 70-76
31. K.H. Lim, C.P. Grey (2000) Characterization of Extra-Framework Cation Positions in Zeolites NaX and NaY with Very Fast ^{23}Na MAS and Multiple Quantum MAS NMR Spectroscopy. *J. Am. Chem. Soc.* 122(40):9768-9780
32. Israelachvili JN et al. (2010) Recent advances in the surface forces apparatus (SFA) technique. *Rep Prog Phys* 73:036601.
33. J.N. Israelachvili, *Intermolecular and Surface Forces, 3rd ed.*, Elsevier, USA **2011**

Chapter 6: Conclusions

This dissertation demonstrated the significant impact that electrostatic surface forces have on non-equilibrium processes such as dissolution, corrosion, and network formation in confined solid-liquid-solid interfaces. The overall unifying theme of the research presented here was to understand the importance of electrostatic forces for non-equilibrium processes at confined interfaces and demonstrate how control of the surface forces can influence the evolution of the interface. Each of these non-equilibrium processes plays an important role in the development of macroscopic properties relevant to technological applications. As such, understanding the driving force behind changes at the interface is necessary to develop improved methods which can positively influence the non-equilibrium processes. Specifically, dissolution-based non-equilibrium processes at the confined interfaces are dramatically influenced by changes in the electrostatic forces. By using a combination of the SFA technique with NMR spectroscopy and standard materials characterization techniques, the changes in molecular interactions can be correlated with the change in macroscopic properties. New insights into the role of electrostatic forces on enhanced dissolution processes at confined interfaces have important implications for the development of technological processes related to improving current CMP or inhibiting corrosion. Additionally, dissolution processes are often the first step in other non-equilibrium processes which involve surface reactions that drastically influence the development of macroscopic properties in catalysis and structural materials.

To accurately characterize non-equilibrium processes at confined solid-liquid-solid interfaces, the proper tools and characterization methods are required. The previous limitations on interfaces for surface characterization techniques were resolved through the

development of composite silica surfaces. These composite surfaces are more versatile due to the ease of functionalization while maintain the ultra-smooth surface roughness required for surface characterization techniques. The development of these surfaces allows for previously unobtainable interfaces to be studied, allowing for characterization of a wider range of interfacial phenomena for dynamic processes.

The investigation of enhanced dissolution processes at confined, asymmetric solid-liquid-solid interfaces using a combination of surface and materials characterization techniques resulted in a broader understanding of enhanced dissolution phenomena. Specifically, the observed enhanced dissolution processes are all strongly influenced by the electrostatic forces at the interface, which had been previously overlooked in a wide range of enhanced dissolution phenomena observed at confined interfaces. An electrochemically enhanced dissolution model was developed and verified through the direct manipulation of observed dissolution of silica, diamond, and nickel using applied electrostatic forces. Notably, this model provides a new method for controlling dissolution processes at confined, asymmetric solid-liquid-solid interfaces through manipulation of the applied electrostatic forces. The insights gained are expected to be broadly applicable as long as the asymmetric solid-liquid-solid interface condition is achieved.

Network formation of aluminosilica materials in alkaline environments has been shown to be strongly dependent on the interaction of dissolved species at the surface of the alumina and silica precursors. The networks that evolve over time are built upon the initial reaction of the dissolved species at the surface which demonstrates the importance of the initial dissolution and condensation processes involved in network formation. At the silica and alumina interface, species released from the surface through dissolution are shown to strongly

interact near the surface and even participate in initial nucleation reactions within the confined interface. The detailed understanding of changes in the molecular structure of aluminosilica networks present future opportunities to correlate the initial formation and growth of aluminosilica networks with the development of macroscopic properties such as adhesion/cohesion. These insights can be used to better understand network formation processes and how to ensure the formation of networks with desirable macroscopic properties for structural materials or catalysis.

The new and detailed molecular-level insights presented in this dissertation are expected to be of interest to researchers working on the characterization of non-equilibrium processes at confined solid-liquid-solid interfaces, especially those involving dissolution processes such as corrosion, CMP, and network formation. The role of intermolecular interactions, such as electrostatic forces, and associated changes in macroscopic properties have been demonstrated for several non-equilibrium processes. In particular, the general model for electrochemically enhanced dissolution demonstrates the importance of understanding the relationship between molecular and macroscopic changes within a system. Consequently, the combination of surface and materials characterization techniques, analyses, and resulting insights demonstrated in this dissertation are expected to be of general relevance to a wide range of non-equilibrium processes at confined interfaces where macroscopic properties develop due to the influence of surface interactions and molecular forces.